ALKÜ FEN BİLİMLERİ DERGİSİ

ALANYA ALAADDİN KEYKUBAT ÜNİVERSİTESİ

Cilt:5 Sayı:3 (Eylül-Aralık 2023)

Volume:5 Issue:3 (September-December 2023)

ALKU JOURNAL of SCIENCE

e-ISSN 2667-7814

Alanya Alaaddin Keykubat University

DERGİNİN KÜNYESİ / *JOURNAL INFO*

Derginin Adı / *Journal Name*: ALKÜ Fen Bilimleri Dergisi / ALKU Journal of Science

Kısa Adı/ *Short Name*:

e-ISSN: 2667-7814

Doi prefix: 10.46740/alku.

Yayın Dili / *Publication Language* : Türkçe / *English*

Yayın Periyodu / *Publication Period*: Yılda üç kez (Nisan, Ağustos ve Aralık) / *Three times a year (April, August, and December)*

Sahibi / *Owner*: Prof. Dr. Kenan Ahmet TÜRKDOĞAN, Alanya Alaaddin Keykubat Üniversitesi Rektörü

Sorumlu Yazı İşleri Müdürü / *Publishing Manager*: Prof. Dr. Mehmet GÜMÜŞ

Kuruluş / *Establishment*: ALKÜ Fen Bilimleri Dergisi, Alanya Alaaddin Keykubat Üniversitesi Rafet Kayış Mühendislik Fakültesi tarafından tüm mühendislik bilimleri ve temel bilimler alanında yılda 3 kez yayınlanan hakemli bir dergidir. Dergimizde, Türkçe ve İngilizce dillerinde orijinal araştırma çalışmaları ve derlemeler yayımlanmaktadır. Bu dergi, hakemli ve açık erişimli bir uluslararası mühendislik bilimleri ve temel bilimler dergisidir. Değerlendirme ve yayınlanma süreçlerinde yazarlardan ücret talep edilmez.

ALKU Journal of Science is an international, peer-reviewed journal which is published by Rafet Kayış Engineering Faculty of Alanya Alaaddin Keykubat University in all areas of engineering and basic science. ALKU Journal of Science is a triannually published open access journal operating an online submission and peer review system which allows authors to submit articles online and track their progress. No charges are required from the authors in all of the publication steps.

Dizinler ve Platformlar / I*ndexing and Platforms*: Google Scholar, Cosmos Impact Factor, ResearchBip, Bielefeld Academic Search Engine (BASE), Asos Index, International Innovative Journal Impact Factor(IIJIF), Scientific Indexing Services(SIS)

Web Adresi/ *Web address* : https://dergipark.org.tr/tr/pub/alku

Yayınlayan Kuruluş / *Publisher* : Alanya Alaaddin Keykubat Üniversitesi / Alanya Alaaddin Keykubat University

Makale gönderim ve takip sistemi / *Article submission and tracking system*: ULAKBİM Dergi Sistemleri, https://dergipark.org.tr/tr/pub/alku

Web barındırma ve teknik destek / *Web hosting and technical support*: Dergipark Akademik http://dergipark.gov.tr/

İletişim / *Contact*: Alanya Alaaddin Keykubat Üniversitesi, Rafet Kayış Mühendislik Fakültesi, Alanya, Antalya. E-mail: alkufbd@alanya.edu.tr Tel/Phone: 0242 5106060 (2545)

YAYIN, DİL ve TEKNİK EDİTÖRLERİ / PUBLISHING, LANGUAGE AND TECHNICAL EDITORS

ALKÜ FEN BİLİMLERİ DERGİSİ 2023:5(2)

ALKU JOURNAL OF SCIENCE 2023:5(2)

İçindekiler / Contents

ALKU Journal of Science 2023, Sayı 5(3): 100-117
e-ISSN: 2667-7814

Original Article

Optimizing the Synthesis of Folic Acid Conjugated Silver Nanoparticles by Box-Behnken Design to Target Breast Cancer Cells

Safa Furkan Soylu[1#], Ahmed KA Zidan[1#], Nazan Gökşen Tosun[2], Özlem Kaplan[3], İsa Gökçe[4*]

[1]*Tokat Gaziosmanpaşa University, Faculty of Engineering and Architecture, Department of Genetics and Bioengineering, Tokat, Turkey.*
[2]*Tokat Gaziosmanpaşa University, Tokat Vocational School of Health Services, Department of Medical Services and Techniques, Tokat, Turkey*
[3]*Alanya Alaaddin Keykubat University, Rafet Kayış Faculty of Engineering, Department of Genetics and Bioengineering, Antalya, Turkey*
[4]*Tokat Gaziosmanpaşa University, Faculty of Pharmacy, Department of Basic Pharmaceutical Sciences, Tokat, Turkey*
#These authors contributed equally to this work
**isa.gokce@gop.edu.tr*

Abstract

In this study, the synthesis of folic acid-conjugated silver nanoparticles (FA&AgNPs) was optimized. FA&AgNPs were synthesized by reduction of silver nitrate with folic acid, which is widely used to target folate receptors in cancer cells. Five independent variables (stirring speed, $AgNO_3$ concentration, folic acid concentration, $AgNO_3$ volume/folic acid volume, and temperature) that were effective on silver nanoparticle synthesis were determined. Based on the independent variables, an experimental plan consisting of 46 experiments was created using the Box-Behnken design (BBD). Nanoparticle formation, physical color change, UV-Vis absorption spectroscopy, Dynamic Light Scattering (DLS) analysis, and Fourier Transform Infrared (FTIR) analysis were evaluated. The mean particle size and zeta potential of FA&AgNPs produced under optimized conditions were measured as 207±4.3 nm and -51.6 mV±2.5, respectively. Cytotoxicity tests were performed to evaluate the anticancer activity of FA&AgNPs in breast cancer cell lines. The IC_{50} values for MDA-MB-231 breast cancer cells at 24 hours and 48 hours were 20.0 µg/mL and 16.9 µg/mL, respectively, and 26.3 µg/mL and 31.5 µg/mL for MCF-7 cells. The findings indicated that FA&AgNPs have the potential to be an effective anticancer agent in breast cancer cells.

Keywords: Folic acid, Silver nanoparticles, Breast cancer, Cell targeting, Optimization

Meme Kanseri Hücrelerini Hedeflemek için Box-Behnken Tasarımıyla Folik Asit Konjuge Gümüş Nanopartiküllerin Sentezinin Optimizasyonu

Özet

Bu çalışmada, folik asit konjuge gümüş nanopartiküllerin (FA&AgNP'ler) sentezi optimize edilmiştir. FA&AgNP'ler, kanser hücrelerinde folat reseptörlerini hedeflemek için yaygın olarak kullanılan folik asit ile gümüş nitratın indirgenmesiyle sentezlenmiştir. Gümüş nanopartikül sentezi üzerinde etkili olan beş bağımsız değişken (karıştırma hızı, $AgNO_3$ konsantrasyonu, folik asit konsantrasyonu, $AgNO_3$ hacmi/folik asit hacmi ve sıcaklık) belirlenmiştir. Bağımsız değişkenlere dayanarak, Box-Behnken tasarımı (BBD)

Geliş/Received: 12 Temmuz/July 2023
Kabul Ediliş/Accepted: 13 Ekim/October 2023

kullanılarak 46 deneyden oluşan bir deney planı oluşturulmuştur. Nanopartikül oluşumu, fiziksel renk değişimi, UV-Vis absorpsiyon spektroskopisi, Dinamik Işık Saçılma (DLS) analizi ve Fourier Dönüşümü Kızılötesi (FTIR) analizi ile değerlendirilmiştir. Optimize edilmiş koşullarda üretilen FA&AgNP'lerin ortalama partikül boyutu ve zeta potansiyeli sırasıyla 207±4.3 nm ve -51.6±2.5 mV olarak ölçülmüştür. Meme kanseri hücre hatlarında FA&AgNP'lerin antikanser etkinliğini değerlendirmek için sitotoksisite testleri yapılmıştır. 24 saat ve 48 saatte MDA-MB-231 meme kanseri hücreleri için IC_{50} değerleri 20.0 µg/mL ve 16.9 µg/mL, MCF-7 hücreleri için ise sırasıyla 26.3 µg/mL ve 31.5 µg/mL olarak bulunmuştur. Bulgular, FA&AgNP'lerin meme kanseri hücrelerinde etkili bir antikanser ajan olma potansiyeline sahip olduğunu göstermiştir.

Anahtar Kelimeler: Folik asit, Gümüş nanopartiküller, Meme kanseri, Hücre hedefleme, Optimizasyon

1. INTRODUCTION

Cancer is an important public health issue that ranks second among worldwide causes of mortality [1]. Developing novel nanoscale chemotherapy agents is increasingly significant in addressing the adverse effects of conventional chemotherapy approaches [2]. Nanoparticles have become highly attractive due to their numerous advantages, such as drug delivery and targeting capabilities [3]. Metallic nanoparticles, nanostructured materials composed of pure metals or their compounds, offer a novel platform for targeted drug delivery, enabling the treatment of diverse diseases within a specific and controlled environment [4]. As one of the metallic nanoparticles with chemical stability, silver nanoparticles (AgNPs) have distinctive features such as strong electrical conductivity, catalytic activity, and antibacterial activities [5,6]. There has been a surge of research investigating the utilization of AgNPs in anticancer therapy in recent years [7-9]. AgNPs can interact with cells and cause cell membrane disruption, affect electron transport chains, generate radicals, interfere with protein synthesis by interacting with ribosomes, affect enzyme function by interacting with enzymes, and cause DNA damage by interacting with DNA [10].

Folic acid (FA), a recognized ligand for folate receptors, has been used to develop nanoformulations with surface functionalization for specific targeting of breast cancer cells [11]. FA plays an important role in the biosynthesis of pyrimidines and purines, which are necessary for DNA synthesis, methylation, and repair. FA is a cofactor in synthesizing purines and pyrimidines in amino acids and DNA/RNA structures [12]. Most cancer tissues overexpress folate receptors, including lung, ovarian, colorectal, brain, breast, epithelial, renal, and cervical malignancies. This expression can target chemicals and medicinal substances directly to malignant cells [13]. Targeting folate receptors is appealing due to their restricted overexpression in healthy tissues and organs. The harmful effects of chemotherapeutic medicines can be decreased by employing folate as a targeting ligand for chemotherapy because folate will preferentially bind to cancer cells overexpressing folate receptors while binding to normal cells at a lower amount [14]. The use of folic acid-conjugated nanocarriers is a preferred method to achieve selective delivery of chemotherapeutic drugs in malignancies that overexpress folate receptors. In this way, many folic acid-conjugated nanoparticles based on polymeric [15], lipid [16], dendrimer [17] and metallic [18] carriers have been designed.

This study focused on optimizing FA&AgNPs synthesis using the Box-Behnken design (BBD). Response surface analysis was used to evaluate the independent variable-response relationship based on particle size and size distribution analysis, and optimal synthesis conditions were determined. UV-Vis spectrophotometry, Dynamic Light Scattering (DLS), and Fourier Transform Infrared (FTIR) analyses were used to characterize the FA&AgNPs. In addition, the effect of FA&AgNPs synthesized under optimal conditions on cell viability in breast cancer cell lines (MDA-MB-231 and MCF-7) was analyzed using the MTT assay. MCF-7 and MDA-MB-231 cell lines are well-known and widely used models representing breast cancer [19]. The expression levels of folate receptors in these two cell lines are different. MDA-MB-231 cells express higher levels of folate receptors than MCF-7 cells [20]. In this respect, these two cell lines were chosen to examine the comparative cytotoxic effects of the FA&AgNPs.

2. MATERIAL AND METHOD

2.1 Material

Silver nitrate ($AgNO_3$) was obtained from Carlo Erba, 3-(4,5-dimethylthiazol-2-yl)-2,5-diphenyltetrazolium bromide (MTT) and Folic acid ($C_9H_{19}N_7O_6$) were purchased from Serva. Dulbecco's Modified Eagle Medium (DMEM) High Glucose, fetal bovine serum (FBS, heat-inactivated), penicillin-streptomycin solution, L-glutamine, phosphate-buffered saline (PBS), and trypsin-EDTA were obtained from Biological Industries. The American Type Culture Collection (ATCC) provided the MDA-MB-231 and MCF-7 cell lines.

2.2 Method

2.2.1 Optimization of synthesis of FA&AgNPs using Box-Behnken design

The synthesis of FA&AgNP was accomplished through a green synthesis approach, eliminating the need for harsh chemicals. It involved mixing a solution of $AgNO_3$ with a solution of FA in specific proportions and at a certain temperature, resulting in the reduction of Ag^+ ions by FA molecules. A graphical summary of the study, including the physical and chemical characterization of FA&AgNP, is depicted in Figure 1.

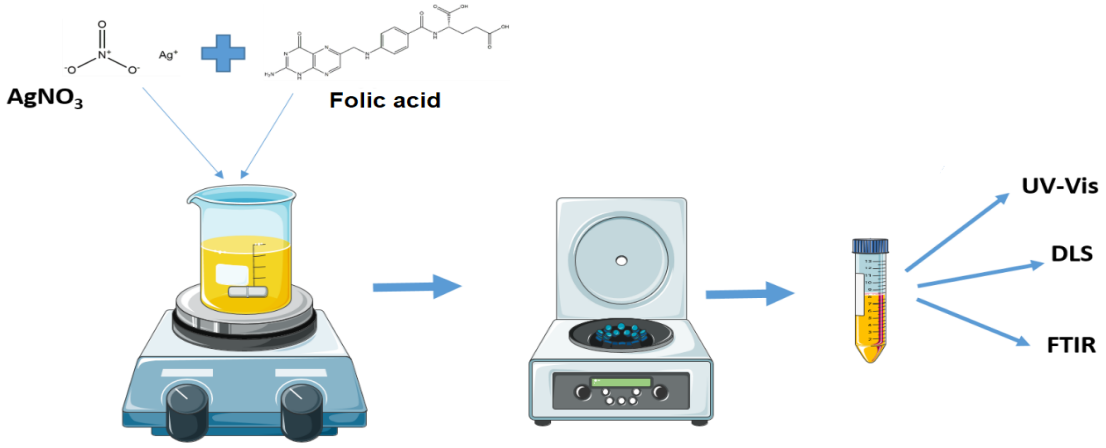

Figure 1. Synthesis and characterization of FA&AgNPs

Five independent variables that could affect the green synthesis of FA&AgNPs were determined. These independent variables are as follows: stirring speed, $AgNO_3$ concentration, FA concentration, V($AgNO_3$) /V(FA) volumetric ratio, and temperature. The ranges in which the independent variables were determined (Table 1). FA&AgNPs were optimized by Box-Behnken design using Design Expert® 11.0 software.

Table 1. Independent variables

Factor	Name	Unit	Min	Max	Mid.
A	Stirring Speed	rpm	250	1000	625
B	$AgNO_3$ concentration	mM	1	5	3
C	Folic acid concentration	mM	1	5	3
D	$AgNO_3$ volume/folic acid volume	-	0,1	0,5	0,3
E	Heat	°C	25	60	42,5

2.2.2 Synthesis of FA&AgNPs

To perform the synthesis of FA&AgNPs, 1 and 10 mM $AgNO_3$ stock solution and 20 mM FA stock solution were prepared. $AgNO_3$ and FA concentrations required for each experiment were diluted from stock solutions. $AgNO_3$ with the concentrations given in Table 2 was taken into beakers with a volume of 10 mL. $AgNO_3$ solution was taken on a magnetic stirrer, and the temperature and stirring speeds were adjusted according to the values given in Table 2. Then, FA solutions were added dropwise into $AgNO_3$ solutions and waited for one hour to complete the reaction. DLS analysis was performed for each of the synthesized FA&AgNPs, and the most suitable one was determined according to size, size distribution, and zeta potential FA&AgNPs were centrifuged for 15 minutes at 13000 rpm. Free silver and FA molecules in the supernatant were eliminated, and FA&AgNPs in the pellet were washed twice with distilled water before being used in the next steps.

2.2.3 Characterization of FA&AgNPs

2.2.3.1 UV-Vis analysis

For proving the synthesis of FA&AgNPs, a UV-Vis spectrophotometer (DeNoVIX) was used to measure the wavelength range of 200-800 nm. Ultra-purified de-ionized water was used as a blank.

2.2.3.2 FTIR analysis

FTIR shows the presence of various functional groups (such as proteins, amino acids, and aldehydes) around the synthesized FA&AgNPs. FA&AgNPs were scanned in the range of 400-4000 cm^{-1} using the Jasco FT/IR 4700 instrument to obtain a good signal-to-noise ratio.

2.2.3.3 DLS analysis

DLS (HORIBA-SZ-100) was used to assess the size, polydispersity, and zeta potential of FA&AgNPs. The measurements were carried out by loading FA&AgNP samples into the electrode cells and under computer control. The cell was washed with deionized water before each measurement.

2.2.4 Biological activity determination of FA&AgNPs

2.2.4.1 Cell culture

The cytotoxic effects of FA&AgNPs on MDA-MB-231 and MCF-7 breast cancer cell lines were investigated. First, MCF-7 and MDA-MB-231 cell lines were cultured in T75 flasks in DMEM High Glucose medium containing 10% FBS, 1% L-glutamine, and 0.1% gentamicin. Cells seeded in T75 flasks were incubated in a 37 °C incubator with 5% CO_2 until they reached 90% confluency.

2.2.4.2 Cell viability analysis

For cell viability analysis, cells were first seeded into 96-well plates at a concentration of 5 x 10^4 cells/mL in each well. Then, these plates were incubated for 24 hours in an incubator at 37 °C containing 5% CO_2. Following the incubation, these cells were treated with FA&AgNPs in the concentration range of 100 µg/mL-1.56 µg/mL and left to incubation (at 37 °C containing 5% CO_2) for 24 and 48 hours. Since viable cells form formazan salts using MTT, the number of viable cells in each well was determined by adding MTT dye to each well. The absorbance value of each well in the plates at a wavelength of 570 nm was measured using a Microplate Reader Spectrophotometer. Cell viability was calculated with the GraphPad 8.1 program. Statistical analysis and comparable data sets were analyzed using GraphPad Prism 8.0 software and a two-way ANOVA with the Sidak test. Statistical significance was determined as a probability value of 0.05.

3. RESULTS AND DISCUSSION

3.1 Optimization of FA&AgNP Synthesis with Box-Behnken Design

The experimental results yielded the size and distribution outputs presented in Table 2.

Table 2. Size and size distributions of FA&AgNPs

Std	Stirring speed(rpm)	$AgNO_3$ cons. (mM)	FA cons. (mM)	V($AgNO_3$) /V(FA)	Heat (°C)	Particle size (nm)	PDI
1	250	1	3	0.3	42.5	778	0.664
2	1000	1	3	0.3	42.5	1151.2	0.592
3	250	5	3	0.3	42.5	443.7	1.198
4	1000	5	3	0.3	42.5	234.4	0
5	625	3	1	0.1	42.5	417.5	1.834
6	625	3	5	0.1	42.5	294.8	0
7	625	3	1	0.5	42.5	371.2	2.359
8	625	3	5	0.5	42.5	295.2	1.688
9	625	1	3	0.3	25	784.5	0.662
10	625	5	3	0.3	25	175.3	0
11	625	1	3	0.3	60	940.3	0.655
12	625	5	3	0.3	60	0	0
13	250	3	1	0.3	42.5	406.1	1.987
14	1000	3	1	0.3	42.5	190.9	4.28
15	250	3	5	0.3	42.5	1894.7	1.421
16	1000	3	5	0.3	42.5	250.5	2.863
17	625	3	3	0.1	25	372.5	2.326
18	625	3	3	0.5	25	316.8	0
19	625	3	3	0.1	60	378.5	1.82
20	625	3	3	0.5	60	128.8	0
21	625	1	1	0.3	42.5	590.1	1.371
22	625	5	1	0.3	42.5	9366.4	5.844
23	625	1	5	0.3	42.5	615	0.655
24	625	5	5	0.3	42.5	9154.6	0.444
25	250	3	3	0.1	42.5	297.4	2.657
26	1000	3	3	0.1	42.5	238.5	3.181
27	250	3	3	0.5	42.5	1345.2	0
28	1000	3	3	0.5	42.5	333.2	1.659
29	625	3	1	0.3	25	345.5	2.626
30	625	3	5	0.3	25	349.9	2.102
31	625	3	1	0.3	60	1199.1	0
32	625	3	5	0.3	60	4320.6	1.595
33	250	3	3	0.3	25	961.1	0.722
34	1000	3	3	0.3	25	208.5	2.578
35	250	3	3	0.3	60	1213.2	0.681
36	1000	3	3	0.3	60	372.2	3.041
37	625	1	3	0.1	42.5	539.8	0.96
38	625	5	3	0.1	42.5	0	0
39	625	1	3	0.5	42.5	668.2	0.638
40	625	5	3	0.5	42.5	2559	1.139
41	625	3	3	0.3	42.5	181.8	2.8
42	625	3	3	0.3	42.5	230.5	3.222

43	625	3	3	0.3	42.5	400.7	1.861
44	625	3	3	0.3	42.5	428.2	0
45	625	3	3	0.3	42.5	363.5	1.326
46	625	3	3	0.3	42.5	89.1	0

3.1.1 Optimization results based on particle size output

Size and size distribution data were entered as output for BBD analysis. Outputs depending on particle size were obtained. The polynomial equation for the response factor was created. The correlation coefficient (R^2) was calculated as 0.9943 based on the obtained data.

Particle Size = 294.125 + 997.54293379686*A + 2893.2610338573*B + 1584.5853083434*C-1923.1442563482*D + 1776.186766928*E + 4865.6142911125*AB + 970.80808645707*AC + 1970.4942563482*AD - 2655.2392004232*AE - 1541.1424652358*BC - 1994.1145329504*BD + 3197.8610338573*BE - 1786.3225665054*CD + 121.08188482467*CE + 1773.1867669287*DE - 590.56795646916*A² + 3710.0391475212*B² + 2306.2389737001*C² - 407.62583887545*D² - 1647.9462439541*E²

Graphics showing how the size changes according to the independent variables are given in Figure 2.

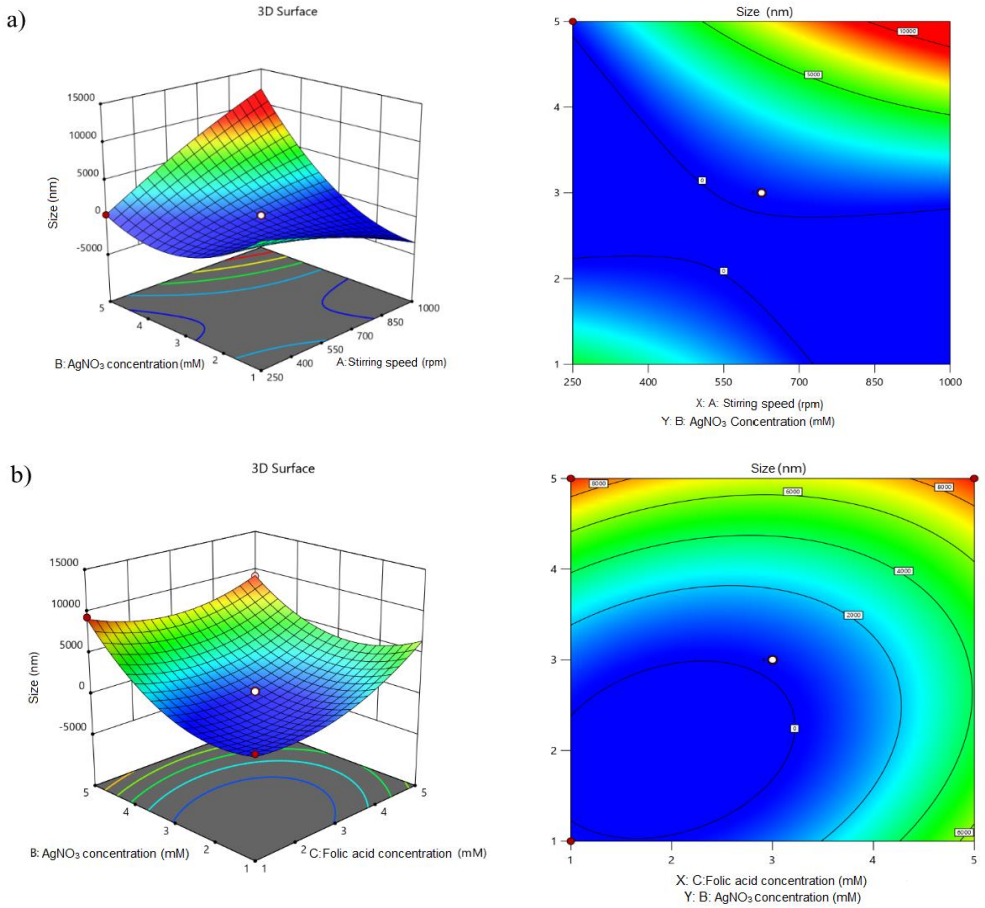

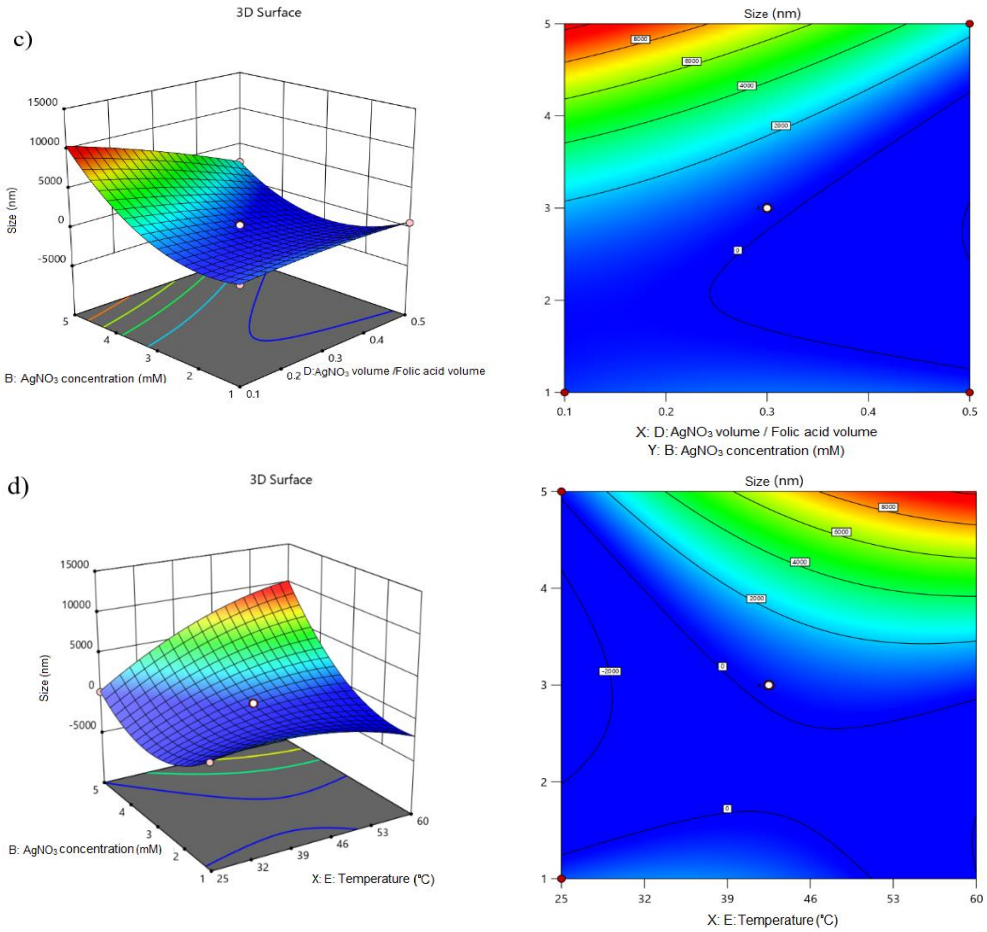

Figure 2. Projection and 3D response surface plots of the parameters affecting the particle size of synthesized FA&AgNPs. (a) $AgNO_3$ concentration and Stirring speed. (b) $AgNO_3$ and FA concentration. (c) $AgNO_3$ concentration and V($AgNO_3$) /V(FA). (d) $AgNO_3$ concentration and temperature.

According to the graphs given in Figure 2, a) It was observed that increasing both the stirring speed and $AgNO_3$ concentration simultaneously increased particle sizes. Similarly, when the stirring speed and $AgNO_3$ concentration were reduced simultaneously, a decrease in particle sizes was observed. b) The size of the particles was found to increase with higher concentrations of $AgNO_3$ and folic acid (FA). Conversely, when $AgNO_3$ and FA concentrations were kept low, nanoparticles with nano-scale sizes could be achieved. c) It was found that an increase in the V($AgNO_3$)/ V(FA) ratio led to larger particle sizes. Particularly, particle sizes close to the desired target were obtained when the $AgNO_3$ concentration was below 3 mM, and the V($AgNO_3$)/ V(FA) ratio approached its upper values. d) Box-Behnken design (BBD) results showed that the $AgNO_3$ concentration should be kept at the lowest levels while increasing the temperature to obtain nano-sized particles. Theoretical considerations suggested particle sizes would be at the desired levels when the temperature and $AgNO_3$ concentration were low. In summary, these findings demonstrate that the particle size of FA&AgNPs can be influenced by the Stirring speed, $AgNO_3$ concentration, V($AgNO_3$)/ V(FA) ratio, and temperature. By optimizing these variables, it is possible to control the particle sizes, especially by employing lower $AgNO_3$ concentrations and temperatures.

3.1.2 Optimization results based on output-to-size distribution (PDI)

A polynomial equation was formulated to represent the response factor. After analyzing the data, the correlation coefficient (R^2) was calculated as 0.9148.

PDI = 2.56055252263 + 0.29602641919865*A + 2.1877807522279*B -0.44682453862887*C - 0.50984250228054*D + 0.22764286716722*E

Figure 3 presented graphical representations illustrating the size variations corresponding to the independent variables. Additionally, in Figure 3, the PDI values showed an increasing trend from blue to red. During the evaluation of the PDI results, it can be concluded that the size distribution within the range of 0-0.7 is predominantly monodisperse. Hence, PDI values falling within this range were deemed the most favorable for nanoparticle synthesis. On the other hand, PDI values outside this range were characterized as polydisperse, indicating a broader size distribution.

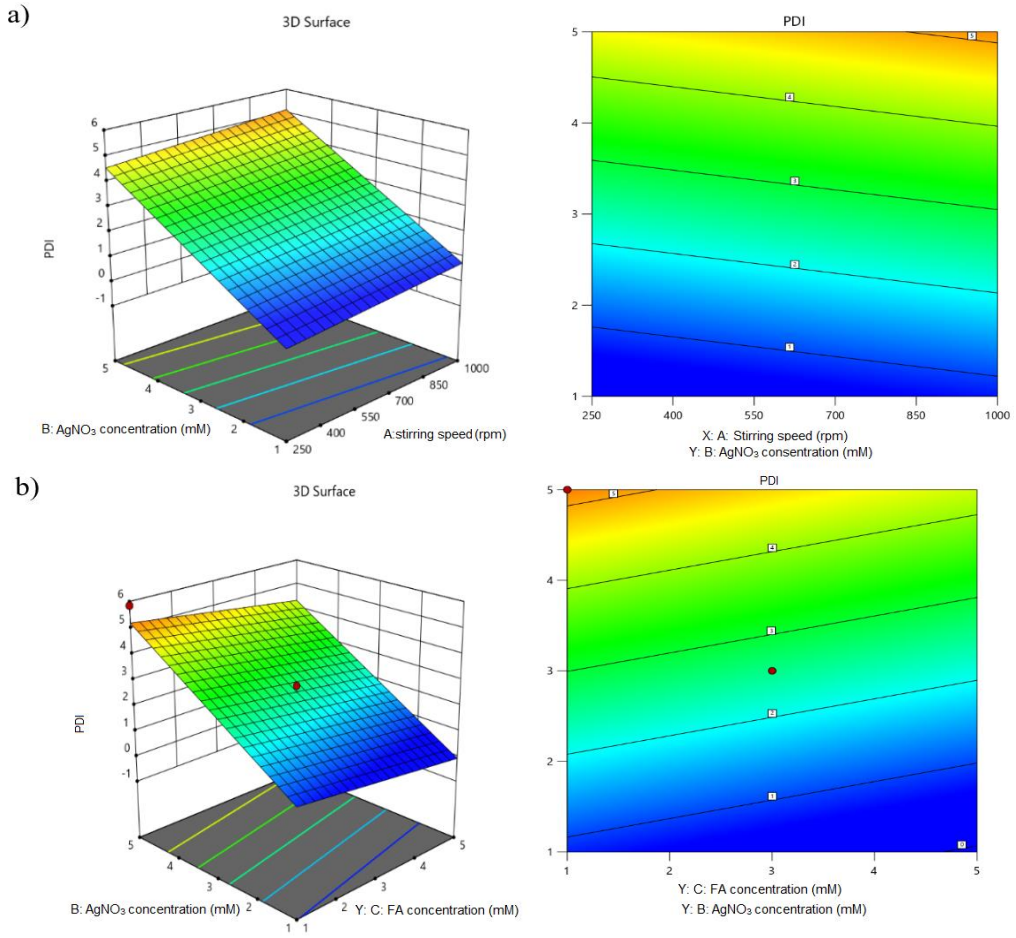

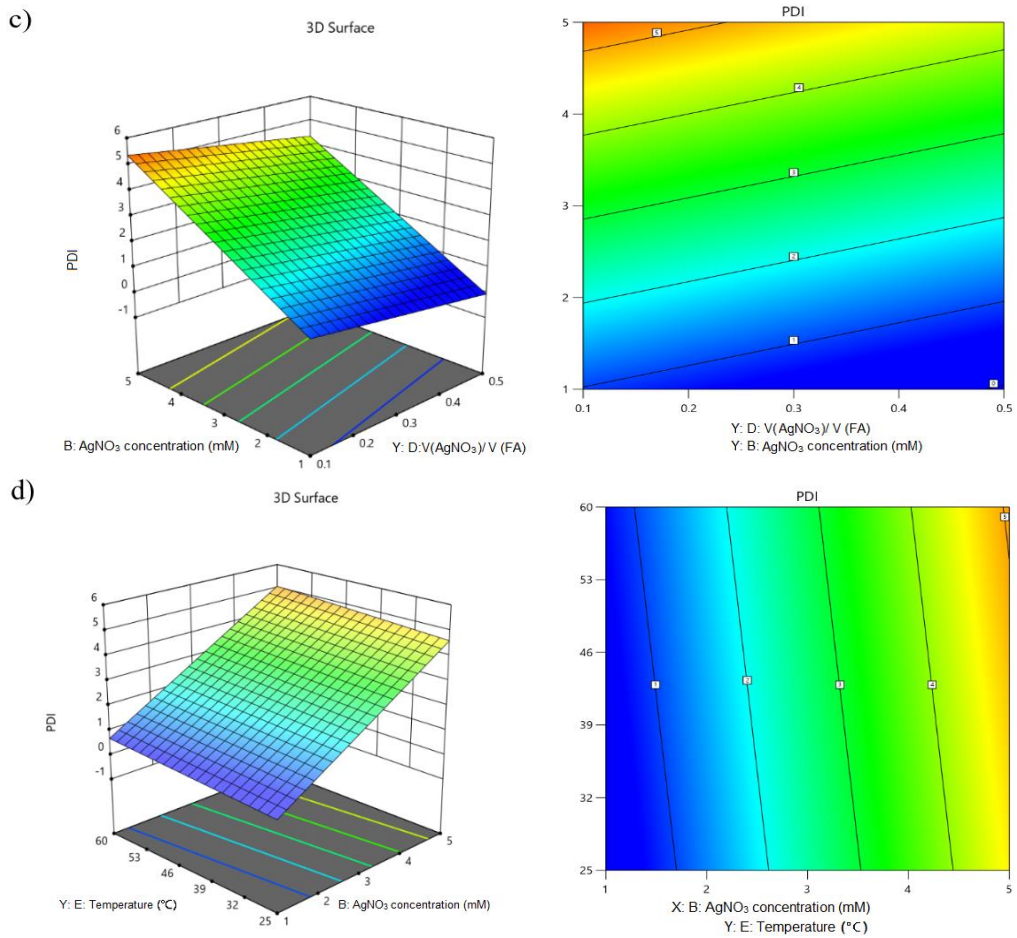

Figure 3**.** Projection and 3D response surface plots of the parameters affecting the PDI values of synthesized FA&AgNPs. (a) $AgNO_3$ concentration and Stirring speed. (b) $AgNO_3$ and FA concentration. (c) $AgNO_3$ concentration and $V(AgNO_3)$ / V(FA) (d) $AgNO_3$ concentration and temperature.

Based on the observations made in Figure 3, a) Simultaneously increasing the stirring speed and $AgNO_3$ concentration resulted in an undesired size distribution in the particles. However, by maintaining a flexible Stirring speed range of 250-1000 rpm and employing low $AgNO_3$ concentrations (1-2 mM), the PDI value can be maintained at desired levels. b) The PDI value tended to increase with higher FA concentrations and lower $AgNO_3$ concentrations. It was determined that the PDI value might be kept within the required range by reducing the FA concentration to 1 mM and keeping the $AgNO_3$ values between 1-2 mM. c) Increasing both the $V(AgNO_3)$/V(FA) ratio and the $AgNO_3$ concentration raised the PDI value. However, the appropriate PDI values were obtained by maintaining a low $V(AgNO_3)$/V(FA) ratio and keeping $AgNO_3$ concentrations within the range of 1-2 mM. d) The Box-Behnken design (BBD) findings showed that raising the temperature while retaining low $AgNO_3$ concentrations can achieve the appropriate PDI values. In summary, the data revealed that regulating the Stirring speed, $AgNO_3$ concentration, $V(AgNO_3)$/V(FA) ratio and temperature were the best conditions for reaching desirable PDI values. It is feasible to generate nanoparticles with the required size distribution by carefully modifying these factors.

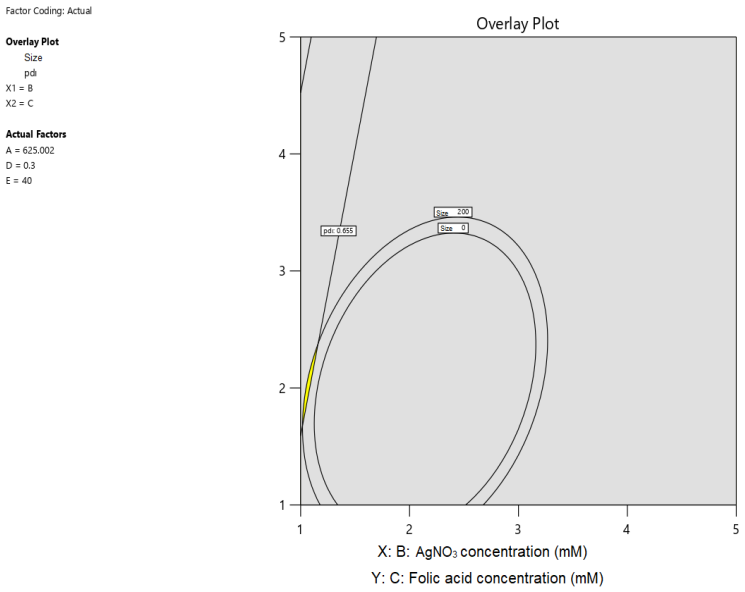

Figure 4. Graph showing the optimized region in yellow and the marked point as selected FA & AgNPs

The optimization of FA&AgNPs using the BBD was carried out as previously reported [21,22]. The desirability function neared a value of one, indicating that the goal response variable was successfully achieved. The optimal conditions for FA&AgNP synthesis were determined based on the yellow region depicted in Figure 4. This region was determined by setting target values for specific independent variables while considering relevant laboratory conditions. The target values for the optimization were as follows: $AgNO_3$ concentration of 1 mM, V($AgNO_3$)/V(FA) ratio of 0.3, temperature of 40°C, stirring speed of 625 rpm, and FA concentration of 2.4 mM.

3.2 Characterization of FA&AgNPs

UV-Vis spectrophotometry was used to characterize the FA&AgNPs synthesized under optimal conditions, and the results were presented in Figure 5. The spectrum of FA&AgNPs exhibited a peak at 419 nm. Additionally, the maximum absorbance wavelength for FA was determined to be 300 nm. Notably, the presence of a peak in the 300-500 nm range for FA&AgNPs, distinct from the peak of FA, serves as evidence for the successful synthesis of FA&AgNPs. As stated in previous studies, the absorption peak in the 300-500 nm region was observed when silver nitrate was reduced to silver nanoparticles. [23,24]. In this study, FA was employed as a reduction agent for silver ions. The prominent bright yellow coloration further confirms the formation of AgNPs. Chowdhuri et al. have demonstrated that FA is an effective reduction agent, providing stability to AgNPs and preventing their aggregation. Consequently, AgNPs synthesized using this approach have exhibited enhanced stability for a period exceeding one year [25].

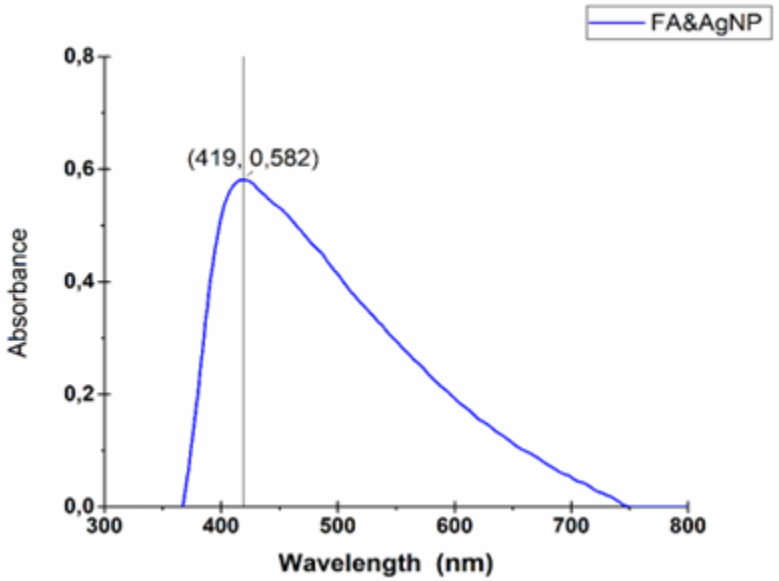

Figure 5. UV-Visible spectra of FA&AgNPs

FTIR analysis was performed to characterize the chemical reduction of silver ions by FA. FTIR analysis results of FA were compared with FTIR analysis results of FA&AgNPs (Figure 6).

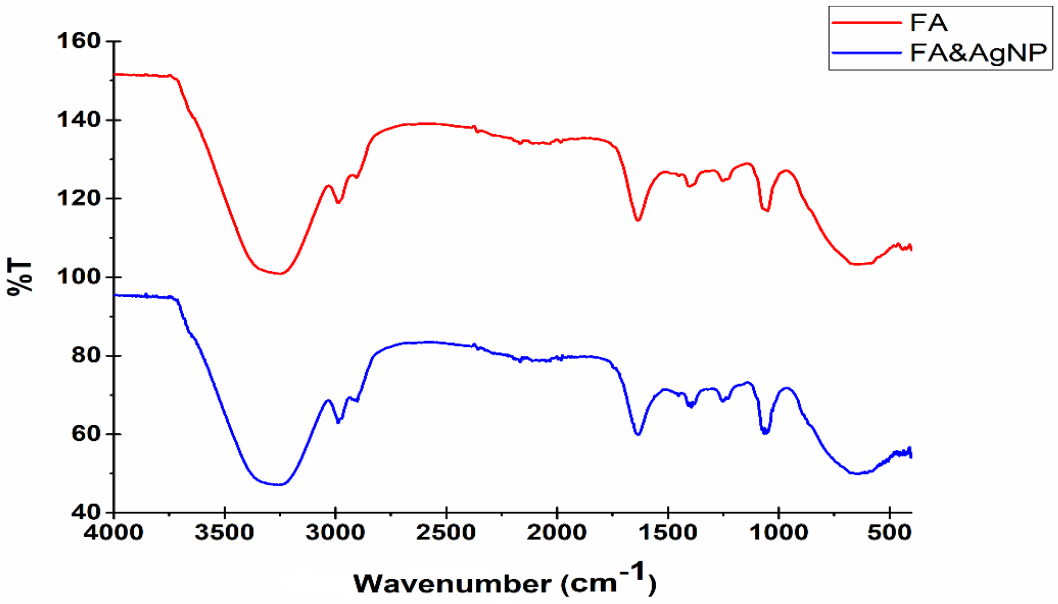

Figure 6. FTIR analysis of FA&AgNPs

Peaks expressing specific information regarding folic acid conjugation were analyzed. In the free folic acid spectra, the distinctive IR absorption peaks at 1633 cm^{-1} and 1487 cm^{-1} were found due to the N-H bending vibration of the CONH group and the absorption band of the phenyl ring, respectively [25]. A prominent peak around 3293 cm^{-1} was characterized as an O-H stretching vibration. The same peaks may be detected in FA&AgNPs, proving chemically that FA binds to Ag^{+} ions.

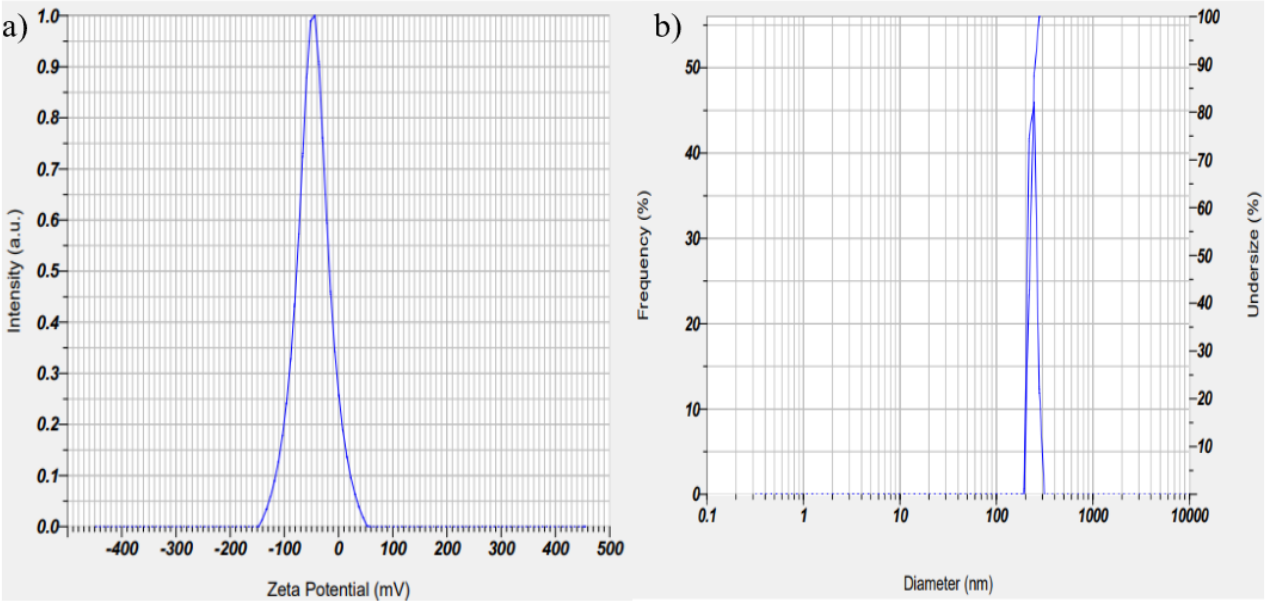

Figure 7. a) DLS of FA&AgNPs, b) Zeta potential of FA&AgNPs

The size of FA&AgNP was determined using DLS, as shown in Figure 7. The FA&AgNPs had an average size of 207±4.3 nm. The polydispersity index (PDI) values are indicative of the uniformity of nanoparticle distribution, and a PDI value exceeding 0.7 suggests a non-uniform distribution of nanoparticles [26]. The nanoparticles were distributed uniformly (polydispersity index: 0.655). In addition, the zeta potential value of the FA&AgNPs was found to be -51.6±2.5 mV. A zeta potential value ranging from -30 mV to +30 mV signifies the excellent dispersion and long-term stability of nanoparticles, reducing the likelihood of aggregation [26]. The presence of a negative charge on the surface of the nanoparticles implied that they are highly stable.

3.3 Cytotoxic Effect of FA AgNPs on Breast Cancer Cell Lines

MTT analysis was used to assess the cytotoxic effects of FA&AgNP on MDA-MB-231 and MCF-7 cell lines. Graphs of concentration-dependent cell viability determined by MTT analysis are shown in Figure 8.

Figure 8 was plotted by calculating the data obtained after 24 and 48 hours for both cell lines with the GraphPad 8.1 program.

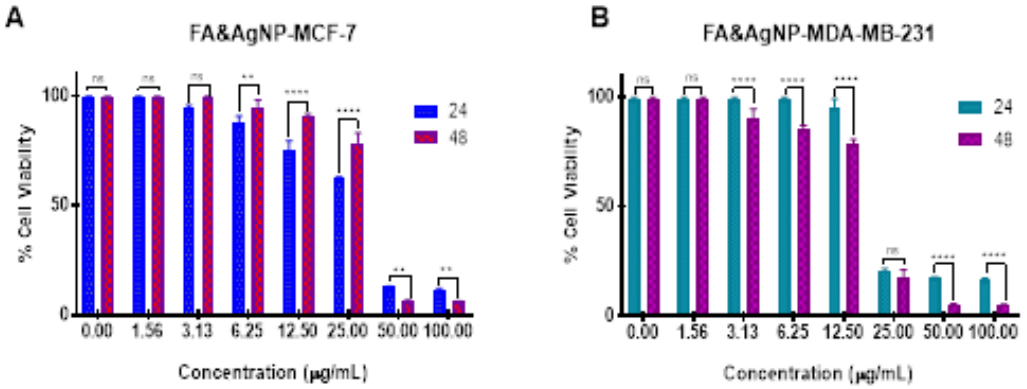

Figure 8. Cytotoxic effect of FA&AgNPs on MCF-7 (A) and MDA-MB-231 (B). The results are shown as the mean SEM (n = 3). *p < 0.05, **p < 0.01, ***p < 0.001 and ****p < 0.0001 represent statistical significance

The concentration value at which cell viability is reduced by 50% corresponds to the concentration value at which 50% of the cells are inhibited. This value is called IC_{50} in this study; it was calculated using GraphPad 8.1 software and presented in Table 3.

Table 3. IC_{50} values of FA&AgNPs after 24 h and 48 h on MDA-MB-231 and MCF-7 cell lines

Cell lines	MCF-7		MDA-MB-231	
Time	24 h	48 h	24 h	48 h
IC_{50} (µg/mL)	26.30 ± 0.003	31.50 ± 0.002	20.00 ± 0.004	16.99 ± 0.003

Two distinct cell lines derived from breast cancer were selected to assess the cytotoxic potential of folic acid-functionalized AgNPs. The MDA-MB-231 and MCF-7 cell lines exhibit contrasting responses to hormone therapies. MCF-7 cells possess both estrogen receptor (ER) and progesterone receptor (PR) while lacking human epidermal growth factor receptor 2 (HER2) [27]. Conversely, MDA-MB-231 represents a triple-negative breast cancer (TNBC) cell line devoid of all three receptors (ER, PR, and HER2), rendering hormone therapy ineffective. MDA-MB-231 and MCF-7 cells express folate receptors, although MDA-MB-231 cells express higher levels of FR-α than MCF-7 cells [20]. In this study, FA&AgNPs showed relatively more cytotoxic activity against MDA-MB-231 cells than MCF-7 cells. This result was attributed to MDA-MB-231 cells expressing higher levels of folate receptors.

Folate receptor-targeting nanoparticles have been studied to treat different cancer therapies, including breast cancer. El-Hammadi et al. developed PLGA nanoparticles with PEG coating and folic acid decoration. These 5-FU loaded-nanoparticles showed superior cytotoxic effects over non-targeting PLGA-based NPs in both HT-29 colon cell lines and MCF-7 breast cancer cell lines [28]. In another study, Erdogar et al. designed folate-conjugated β-cyclodextrins loaded with paclitaxel. Conjugation of paclitaxel with folate-conjugated cyclodextrin showed that it increased the sensitivity and cellular uptake efficiency of breast cancer cells towards the developed NPs, thus reducing the side effects of paclitaxel[29].

Karuppaiah et al. synthesized folic acid-conjugated silver nanoparticles and investigated their combined effect with gemcitabine (GEM) on breast cancer cells. It has been demonstrated that FA serves as a potent reducing and coating agent for cancer cells with folate receptors. FA-coated GEM-AgNPs exhibited synergistic effects and increased selectivity against MDA-MB-453 cells. FA-coated GEM-AgNPs demonstrated increased cytotoxicity (IC_{50}=35.34 µM) compared to the individual use of GEM and AgNPs, resulting in reduced dose-dependent toxicity. Furthermore, the induction of apoptotic cell death by FA-GEM-AgNPs in the MDA-MB-453 cell line was observed [30]. Banu et al. synthesized folic acid conjugated polymer-gold composite nanoparticles (GNPs) that combined doxorubicin (DOX) with laser photothermal treatment. The surface of GNPs was changed with folate, and polyethylene glycol (PEG) was designed to carry DOX to the targeted breast cancer cells. The folic acid-conjugated DOX-loaded polymeric GNPs and laser photothermal treatment outperformed DOX alone, notably against breast cancer cells with high folate expression (MDA-MB-231) [31,32]. DOX conjugated with N-acetyl glucosamine or folate-functionalized mesoporous silica nanoparticles (DOX-NAG-MSNP or DOX-FA-MSNPs) has been synthesized by Pramod et al. DOX-NAG-MSNPs had stronger cellular absorption and cytotoxicity than DOX-FA-MSNPs, particularly in MDA-MB-231 and MCF-7 cells. DOX-FA-MSNPs and DOX-NAG-MSNPs demonstrated better DOX transport to specific breast cells as compared to free DOX [33,34]. Considering the previous studies and the data obtained in our study, using folic acid-conjugated nanoparticles for targeting the folate receptor is considered a promising approach to treating breast cancer. It has been reported that folic acid-conjugated nanocarrier systems can bind selectively to the folate receptor

on the surface of cancer cells and be carried into the cell via clathrin-mediated endocytosis [35,36]. Circulating folic acid-conjugated transporters bind to folate receptors on the surface of cancer cells, resulting in invagination, internalization, and vesicle formation. When the pH within the vesicle decreases, the folic acid-conjugated chemotherapeutic drug is released into the cytosol, causing the desired pharmacological action in cancer cells. This impact either stops cell division or causes apoptosis [37]. As a result, the FA&AgNPs synthesized in this study may be delivered to the cells via clathrin-mediated endocytosis by binding to the folate receptor in breast cancer cells. It has been shown in numerous studies that silver nanoparticles exhibit cytotoxic effects on cancer cells through mechanisms such as disrupting cell membranes, interfering with electron transport chains, creating radicals, disrupting protein synthesis through ribosome interaction, affecting enzymes, and triggering DNA damage [7,10]. Therefore, FA&AgNPs that can specifically bind to the folate receptor may have a cytotoxic effect on cells through these mechanisms.

In recent years, investigations have been carried out to investigate the green synthesis of silver nanoparticles using plant extracts and their anticancer effects on breast cancer. Santhoshkumar et al. synthesized silver nanoparticles from the liquid extract obtained from *Gymnema sylvestre* leaves by green synthesis and determined the IC_{50} value as 44±0.8 µg/mL on MDA-MB-231 cells after 24h. Darvish et al. silver nanoparticles were synthesized using *Ducrosia Anethifolia* aqueous extract and investigated the cytotoxic effect of these nanoparticles on MDA-MB-231 and MCF-7 cells. After 24 h, IC_{50} values were calculated as 45.24±2.96 µg/mL and 33.78±3.54 µg/mL, respectively [38]. The metabolite content of the extract used in the synthesis of FA&AgNPs and the size, zeta potential, and particle size distribution of FA&AgNPs are the factors affecting the toxicity of the FA&AgNPs produced in this study on breast cancer cells. The IC_{50} values of the FA&AgNPs obtained in this study on MDA-MB-231 and MCF-7 cells after 24 h were calculated as 20.0 µg/mL and 26.3 µg/mL, respectively. After 48 hours, IC_{50} values on MDA-MB-231 and MCF-7 cells were found to be 16.99 µg/mL and 31.50 µg/mL, respectively. While FA&AgNPs showed a dose- and time-dependent cytotoxic effect on the MDA-MB-231 cell line, the time-dependent cytotoxic effect did not increase on MCF-7 cell lines. FA&AgNPs exhibited higher cytotoxicity than MCF-7 in MDA-MB-231 cell lines, indicating that they may be more effective in this cell line. The possible reason for this effect is that MDA-MB-231 cells express higher levels of folate receptors than MCF-7 cells.

4. CONCLUSION

In this study, FA&AgNPs were synthesized using $AgNO_3$ salt and FA as a reducing agent. The synthesis of FA&AgNPs was systematically optimized using the Box-Behnken design. The experimental design consisted of 46 different trials generated theoretically based on five independent variables (Stirring speed, $AgNO_3$ concentration, FA concentration, $V(AgNO_3)/V(FA)$ ratio, and temperature). Nanoparticle formation was physically detected by monitoring the color transformation and absorption band based on the surface plasmon resonance of the nanoparticles. FTIR analysis revealed the binding of FA to Ag^+ ions. The $AgNO_3$ concentration was found to be highly influential in nanoparticle formation efficiency. The optimal conditions were determined as a stirring speed of 625 rpm, $AgNO_3$ concentration of 1 mM, $V(AgNO_3)/V(FA)$ ratio of 0.3, and FA concentration of 2.4 mM. The average size and zeta potential of the synthesized FA&AgNPs were measured as 207±4.3 nm and -51.6±2.5 mV, respectively. Cytotoxicity results on breast cancer cell lines MDA-MB-231 and MCF-7 showed that FA&AgNPs could potentially serve as agents with anticancer activity. In conclusion, the synthesized and optimized FA&AgNPs in this study hold promise as a novel agent for potential use in breast cancer treatment in future studies.

ACKNOWLEDGEMENTS

This study received support from the Turkish Scientific and Technical Research Council (TUBITAK) under grant number TUBITAK-2209A (Project number: 1919B012106589).

REFERENCES

[1] Sung H., Ferlay J., Siegel R.L., Laversanne M., Soerjomataram I., Jemal A., Bray F. (2021). "Global Cancer Statistics 2020: GLOBOCAN Estimates of Incidence and Mortality Worldwide for 36 Cancers in 185 Countries." CA: A Cancer Journal for Clinicians 71, 209-249. https://doi.org/10.3322/caac.21660

[2] Yao Y., Zhou Y., Liu L., Xu Y., Chen Q., Wang Y., Wu S., Deng Y., Zhang J., Shao A. (2020). "Nanoparticle-Based Drug Delivery in Cancer Therapy and Its Role in Overcoming Drug Resistance." Front Mol Biosci 7, 193. 10.3389/fmolb.2020.00193

[3] Khan I., Saeed K., Khan I. (2019). "Nanoparticles: Properties, applications and toxicities." Arabian Journal of Chemistry 12, 908-931. https://doi.org/10.1016/j.arabjc.2017.05.011

[4] Chandrakala V., Aruna V., Angajala G. (2022). "Review on metal nanoparticles as nanocarriers: current challenges and perspectives in drug delivery systems." Emergent Materials 5, 1593-1615. 10.1007/s42247-021-00335-x

[5] Gökşen Tosun N., Kaplan Ö., Türkekul İ., Gökçe İ., Özgür A. (2022). "Green synthesis of silver nanoparticles using Schizophyllum commune and Geopora sumneriana extracts and evaluation of their anticancer and antimicrobial activities." Particulate Science and Technology 40, 801-811. 10.1080/02726351.2021.2010846

[6] Kaplan Ö., Gökşen Tosun N., İmamoğlu R., Türkekul İ., Gökçe İ., Özgür A. (2022). "Biosynthesis and characterization of silver nanoparticles from Tricholoma ustale and Agaricus arvensis extracts and investigation of their antimicrobial, cytotoxic, and apoptotic potentials." Journal of Drug Delivery Science and Technology 69, 103178. https://doi.org/10.1016/j.jddst.2022.103178

[7] Gökşen Tosun N., Kaplan Ö., Imamoğlu R., Türkekul İ., Gökçe İ., Özgür A. (2022). "Green synthesized silver nanoparticles with mushroom extracts of Paxina leucomelas and Rhizopogon luteolus induce ROS-Induced intrinsic apoptotic pathway in cancer cells." Inorganic and Nano-Metal Chemistry 1-10. 10.1080/24701556.2022.2081200

[8] Kaplan Ö., Gökşen Tosun N., Özgür A., Erden Tayhan S., Bilgin S., Türkekul İ., Gökce İ. (2021). "Microwave-assisted green synthesis of silver nanoparticles using crude extracts of Boletus edulis and Coriolus versicolor: Characterization, anticancer, antimicrobial and wound healing activities." Journal of Drug Delivery Science and Technology 64, 102641. https://doi.org/10.1016/j.jddst.2021.102641

[9] Rudrappa M., Kumar R.S., Nagaraja S.K., Hiremath H., Gunagambhire P.V., Almansour A.I., Perumal K., Nayaka S. (2023). "Myco-Nanofabrication of Silver Nanoparticles by Penicillium brasilianum NP5 and Their Antimicrobial, Photoprotective and Anticancer Effect on MDA-MB-231 Breast Cancer Cell Line." Antibiotics 12, 567

[10] Mikhailova E.O. (2020). "Silver Nanoparticles: Mechanism of Action and Probable Bio-Application." J Funct Biomater 11. 10.3390/jfb11040084

[11] Tagde P., Kulkarni G.T., Mishra D.K., Kesharwani P. (2020). "Recent advances in folic acid engineered nanocarriers for treatment of breast cancer." Journal of Drug Delivery Science and Technology 56, 101613. https://doi.org/10.1016/j.jddst.2020.101613

[12] Moffatt B.A., Ashihara H. (2002). "Purine and pyrimidine nucleotide synthesis and metabolism." Arabidopsis Book 1, e0018. 10.1199/tab.0018

[13] Zwicke G.L., Mansoori G.A., Jeffery C.J. (2012). "Utilizing the folate receptor for active targeting of cancer nanotherapeutics." Nano Rev 3. 10.3402/nano.v3i0.18496

[14] Martín-Sabroso C., Torres-Suárez A.I., Alonso-González M., Fernández-Carballido A., Fraguas-Sánchez A.I. (2021). "Active Targeted Nanoformulations via Folate Receptors: State of the Art and Future Perspectives." Pharmaceutics 14. 10.3390/pharmaceutics14010014

[15] Luong D., Kesharwani P., Alsaab H.O., Sau S., Padhye S., Sarkar F.H., Iyer A.K. (2017). "Folic acid conjugated polymeric micelles loaded with a curcumin difluorinated analog for targeting cervical and ovarian cancers." Colloids and Surfaces B: Biointerfaces 157, 490-502. https://doi.org/10.1016/j.colsurfb.2017.06.025

[16] Sabzichi M., Mohammadian J., Khosroushahi A.Y., Bazzaz R., Hamishehkar H. (2016). "Folate-Targeted Nanostructured Lipid Carriers (NLCs) Enhance (Letrozol) Efficacy in MCF-7 Breast Cancer Cells." Asian Pacific Journal of Cancer Prevention 17, 5185-5188. 10.22034/APJCP.2016.17.12.5185

[17] Xu L., Yang H., Folate-Decorated Polyamidoamine Dendrimer Nanoparticles for Head and Neck Cancer Gene Therapy, in: L. Dinesh Kumar (Ed.) RNA Interference and Cancer Therapy: Methods and Protocols, Springer New York, New York, NY, 2019, pp. 393-408.

[18] Ghaznavi H., Hosseini-Nami S., Kamrava S.K., Irajirad R., Maleki S., Shakeri-Zadeh A., Montazerabadi A. (2018). "Folic acid conjugated PEG coated gold–iron oxide core–shell nanocomplex as a potential agent for targeted photothermal therapy of cancer." Artificial Cells, Nanomedicine and Biotechnology 46, 1594-1604. 10.1080/21691401.2017.1384384

[19] Comșa Ș., Cimpean A.M., Raica M. (2015). "The story of MCF-7 breast cancer cell line: 40 years of experience in research." Anticancer research 35, 3147-3154

[20] Marshalek J.P., Sheeran P.S., Ingram P., Dayton P.A., Witte R.S., Matsunaga T.O. (2016). "Intracellular delivery and ultrasonic activation of folate receptor-targeted phase-change contrast agents in breast cancer cells in vitro." J Control Release 243, 69-77. 10.1016/j.jconrel.2016.09.010

[21] Gökşen Tosun N., Kaplan Ö. (2021). "Optimization of the green synthesis of silver nanoparticle with Box-Behnken design: Using Aloe vera plant extract as a reduction agent." Sakarya University Journal of Science 25, 774-787

[22] Lalegani Z., Seyyed Ebrahimi S.A. (2020). "Optimization of synthesis for shape and size controlled silver nanoparticles using response surface methodology." Colloids and Surfaces A: Physicochemical and Engineering Aspects 595, 124647. https://doi.org/10.1016/j.colsurfa.2020.124647

[23] Gökşen Tosun N., Kaplan Ö., Imamoğlu R., Türkekul İ., Gökçe İ., Özgür A. "Green synthesized silver nanoparticles with mushroom extracts of Paxina leucomelas and Rhizopogon luteolus induce ROS-Induced intrinsic apoptotic pathway in cancer cells." Inorganic and Nano-Metal Chemistry 1-10. 10.1080/24701556.2022.2081200

[24] Subba Rao Y., Kotakadi V.S., Prasad T.N.V.K.V., Reddy A.V., Sai Gopal D.V.R. (2013). "Green synthesis and spectral characterization of silver nanoparticles from Lakshmi tulasi (Ocimum sanctum) leaf extract."

Spectrochimica Acta Part A: Molecular and Biomolecular Spectroscopy 103, 156-159. https://doi.org/10.1016/j.saa.2012.11.028

[25] Chowdhuri A.R., Tripathy S., Haldar C., Chandra S., Das B., Roy S., Sahu S.K. (2015). "Theoretical and experimental study of folic acid conjugated silver nanoparticles through electrostatic interaction for enhance antibacterial activity." RSC Advances 5, 21515-21524. 10.1039/C4RA16785F

[26] Xu L., Wang Y.Y., Huang J., Chen C.Y., Wang Z.X., Xie H. (2020). "Silver nanoparticles: Synthesis, medical applications and biosafety." Theranostics 10, 8996-9031. 10.7150/thno.45413

[27] Bandyopadhyay A., Roy B., Shaw P., Mondal P., Mondal M.K., Chowdhury P., Bhattacharya S., Chattopadhyay A. (2020). "Cytotoxic effect of green synthesized silver nanoparticles in MCF7 and MDA-MB-231 human breast cancer cells in vitro." The Nucleus 63, 191-202. 10.1007/s13237-019-00305-z

[28] El-Hammadi M.M., Delgado Á.V., Melguizo C., Prados J.C., Arias J.L. (2017). "Folic acid-decorated and PEGylated PLGA nanoparticles for improving the antitumour activity of 5-fluorouracil." International Journal of Pharmaceutics 516, 61-70. https://doi.org/10.1016/j.ijpharm.2016.11.012

[29] Erdoğar N., Esendağlı G., Nielsen T.T., Şen M., Öner L., Bilensoy E. (2016). "Design and optimization of novel paclitaxel-loaded folate-conjugated amphiphilic cyclodextrin nanoparticles." International Journal of Pharmaceutics 509, 375-390. https://doi.org/10.1016/j.ijpharm.2016.05.040

[30] Karuppaiah A., Rajan R., Hariharan S., Balasubramaniam D.K., Gregory M., Sankar V. (2020). "Synthesis and Characterization of Folic Acid Conjugated Gemcitabine Tethered Silver Nanoparticles (FA-GEM-AgNPs) for Targeted Delivery." Curr Pharm Des 26, 3141-3146. 10.2174/1381612826666200316143239

[31] Kesharwani P., Banerjee S., Gupta U., Mohd Amin M.C.I., Padhye S., Sarkar F.H., Iyer A.K. (2015). "PAMAM dendrimers as promising nanocarriers for RNAi therapeutics." Materials Today 18, 565-572. https://doi.org/10.1016/j.mattod.2015.06.003

[32] Banu H., Sethi D.K., Edgar A., Sheriff A., Rayees N., Renuka N., Faheem S.M., Premkumar K., Vasanthakumar G. (2015). "Doxorubicin loaded polymeric gold nanoparticles targeted to human folate receptor upon laser photothermal therapy potentiates chemotherapy in breast cancer cell lines." Journal of Photochemistry and Photobiology B: Biology 149, 116-128. https://doi.org/10.1016/j.jphotobiol.2015.05.008

[33] Kumar P., Tambe P., Paknikar K.M., Gajbhiye V. (2017). "Folate/N-acetyl glucosamine conjugated mesoporous silica nanoparticles for targeting breast cancer cells: A comparative study." Colloids and Surfaces B: Biointerfaces 156, 203-212. https://doi.org/10.1016/j.colsurfb.2017.05.032

[34] Kesharwani P., Choudhury H., Meher J.G., Pandey M., Gorain B. (2019). "Dendrimer-entrapped gold nanoparticles as promising nanocarriers for anticancer therapeutics and imaging." Progress in Materials Science 103, 484-508. https://doi.org/10.1016/j.pmatsci.2019.03.003

[35] Assaraf Y.G., Leamon C.P., Reddy J.A. (2014). "The folate receptor as a rational therapeutic target for personalized cancer treatment." Drug Resistance Updates 17, 89-95. https://doi.org/10.1016/j.drup.2014.10.002

[36] Ramzy L., Nasr M., Metwally A.A., Awad G.A.S. (2017). "Cancer nanotheranostics: A review of the role of conjugated ligands for overexpressed receptors." European Journal of Pharmaceutical Sciences 104, 273-292. https://doi.org/10.1016/j.ejps.2017.04.005

[37] Xu L., Bai Q., Zhang X., Yang H. (2017). "Folate-mediated chemotherapy and diagnostics: An updated review and outlook." Journal of Controlled Release 252, 73-82. https://doi.org/10.1016/j.jconrel.2017.02.023

[38] Darvish S., Saeed Kahrizi M., Özbolat G., Khaleghi F., Mortezania Z., Sakhaei D. (2022). "Silver nanoparticles: Biosynthesis and cytotoxic performance against breast cancer MCF-7 and MDA-MB-231 cell lines." Nanomedicine Research Journal 7, 83-92

ALKU Journal of Science 2023, Sayı 5(3): 118-130
e-ISSN: 2667-7814

Original Article

A Numerical Study on Cross Flow Heat Exchanger with Different Reynolds (Re) Numbers

Gökhan CANBOLAT[1*]
[1]*Alanya Alaaddin Keykubat University, Rafet Kayış Faculty of Engineering, Department of Mechanical Engineering, Antalya, Turkey*
**gokhan.canbolat@alanya.edu.tr*

Abstract

Heat exchangers are highly popular in engineering and industrial applications. Numerical studies on heat exchangers to investigate the performance of heat transfer have been carried out widely by Computational Fluid Dynamics (CFD) in recent years. In this study, a circular pipe with hot water in cross flow is investigated in different Reynolds (Re) numbers. Flow is turbulent flow and the Re number varies from 3165 to 4643 in the circular pipe. The air is at a temperature of 303 K and the water is at 333 K. Variation of flow characteristics and thermal performance is observed according to an increase in Re numbers such as Wall Shear Stress (WSS), Skin Friction Coefficient (C_f), Nusselt Number (Nu), heat transfer coefficient (h) and surface temperature of the circular pipe. Results show that there are no significant changes for the WSS and C_f values in the specified range of the Re number. However, when the thermal performance is evaluated, the temperature of the surface of the circular pipe, heat transfer coefficient, and Nu number values are increased by an increase in the Re number. Here, the increase is approximately 2% for the specified range of Re number, and it is shown that it can be increased by the flow conditions. The maximum Nu number is 4482.37 at the Re number of 4643. As a result, the Re number is highly effective in controlling the heat transfer performance of a heat exchanger.

Keywords: Heat Exchanger, Cross-Flow, Computational Fluid Dynamics (CFD), Heat Transfer

Farklı Reynolds (Re) Sayılarında Çapraz Akışlı Bir Isı Değiştirici Üzerine Nümerik Bir Çalışma

Özet

Isı değiştiriciler mühendislik ve endüstriyel uygulamalarda oldukça popülerdir. Isı değiştiriciler üzerindeki ısı transferi performansının araştırılmasına yönelik sayısal çalışmalar son yıllarda Hesaplamalı Akışkanlar Dinamiği (HAD) yöntemiyle yaygın şekilde gerçekleştirilmektedir. Bu çalışmada farklı Reynolds (Re) sayıları ile çapraz akışlı sıcak su içeren dairesel bir boru incelenmiştir. Türbülanslı bir akışta, dairesel boru için Re sayısı 3165 ile 4643 arasında değişmektedir. Hava 303 K, su ise 333 K sıcaklıktadır. Akış karakteristikleri ve termal performans açısından Duvardaki kayma gerilmesi, Yüzey sürtünme katsayısı (Cf), Nusselt sayısı (Nu), Isı transferi kaysayısı (h) ve yüzey sıcaklığı Re sayısındaki artışa göre incelenmiştir. Sonuçlar, belirtilen Re sayısı aralığında kayma gerilmesi ve Cf değerleri için önemli bir değişiklik olmadığını göstermektedir. Ancak ısıl performans değerlendirildiğinde, Re sayısının artmasıyla dairesel borunun yüzey sıcaklığı, ısı transfer katsayısı ve Nu sayısı değerleri de artmaktadır. Burada, belirtilen Re sayısı aralığı için artış yaklaşık % 2 olup, akış koşullarıyla artırılabileceği gösterilmektedir. Re sayısı 4643'te maksimum Nu sayısı 4482.37 olarak hesaplamıştır. Sonuç olarak Re numarası, bir ısı değiştiricinin ısı transfer performansının kontrolünde oldukça etkilidir.

Anahtar Kelimeler: Isı Değiştirici, Çapraz Akış, Hesaplamalı Akışkanlar Dinamiği (HAD), Isı Transferi

Geliş/Received: 28 Eylül/September 2023
Kabul Ediliş/Accepted: 04 Ekim/October 2023

1. INTRODUCTION

Heat exchangers are popularly utilized in industrial and engineering applications. In the design of heat exchangers, cross-flow in tubes is widely used in engineering and industrial applications such as flow across over the tubes, cooling systems, electronic types of equipment, production process, boiler economizers, air preheater, air conditioning, and automotive radiator, etc. Therefore, various studies have been performed to observe the heat transfer in such flow [1]. Due to the increasing demands for energy saving in recent years, the need for efficient design of heat exchangers with low pressure drop and high heat transfer increase has increased [2].

The procedure of design for the heat exchanger is highly complicated. The analysis of heat transfer is needed to perform efficiently in terms of long-term performance and economy. While new technologies are integrated to increase the heat transfer by the improvement in the heat transfer rate, the pressure drop also increases, resulting the a higher pumping cost. Cross-flow exchangers are generally used by fins or without. Here, the high difference between the heat transfer coefficient for fluids such as gas and liquid, the heat transfer rate will be limited with lower heat transfer coefficient for gas. Here, fins are not mandatory for installation but fins increase the heat transfer area [3,4]. The heat transfer enhancement can be performed by various techniques for the heat exchangers. Here, these techniques are divided into two methods they are passive and active. In the active methods, an external method is needed such as electric, mechanical equipment, and vibration. On the other hand, in the passive methods, external power is not needed but surface geometry or additive fluid causes the heat transfer phenomenon. However, passive ones are commercially interested in heat transfer enhancement. Heat exchangers can be classified primarily according to flow types they are counter, parallel, and cross-flow. Cross-flow as in this study, the fluid flow is perpendicular to each other [5].

In a study, a tube exchanger is studied both numerically and experimentally. Large eddy simulation (LES) is also integrated to study to investigate the fluid flow and heat transfer. Small tubes with a diameter of 5.2 mm are used as flow channels. It is concluded that small tubes increase the heat transfer coefficient compared the large tubes and the LES method is highly effective in predicting fluid mechanics and heat transfer for the heat exchangers [6]. In a study, a steady, laminar, and two-dimensional incompressible flow is investigated for the tube bundles for a heat exchanger. The effects of Reynolds number, Prandtl number, and aspect ratio are studied to observe pressure drop and heat transfer performance. They reported that the Nu number increases with an increase in the Reynolds number. A higher length for the aspect ratio is more efficient in increasing the heat transfer ratio. Equivalent circular tubes perform better heat transfer according to flat tube banks. When the pressure drop is investigated, flat tube banks are better according to circular tubes [7]. In a study, the effect of the longitudinal pitch on heat transfer performance in a cross-flow is investigated over an inline tube heat exchanger. A geometry with symmetric and periodic boundary conditions is implemented for analysis. A single phase and turbulent flow are studied to examine the turbulent flow. In the study by Zukauskas, it was reported that the heat transfer coefficient can be reduced by correlation with a decrease in the longitudinal pitch [8]. The heat transfer performance can be estimated with the empirical correlations in the literature [9].

In this study, a cross-flow heat exchanger is studied with different Re numbers under turbulent flow conditions. The geometry is constructed as a one-way hot water to air that is perpendicular to water flow. Analysis is performed by the CFD and uniform mesh generation is aimed before the studies. Flow is three-dimensional, incompressible, and transitional flow is also taken into account during the flow. The Re numbers are 3165, 3587, 3904,4221, and 4643 for the turbulent flows. Air is at a temperature of 303 K and water is at 333 K. So the temperature difference is 30 K between water and air. The variation of WSS, C_f, Nu, h, and temperature on the pipe surface is investigated for comparison. In the given range of the Re numbers, the increase in heat transfer is approximately 2%. For the case of Re number is 4643, the

maximum Nu number is 4482.37 obtained by CFD studies. CFD calculations are highly effective in guiding heat transfer enhancement for heat exchangers.

2. MATERIAL AND METHOD

In this section, the definition of the geometry for the heat exchanger, generation of mesh and mesh independency test, boundary conditions for the flows for air and water, governing equations for the fluid flow and heat transfer, and the numerical approach are shown.

2.1 Geometry, Generation of Mesh and Mesh Sensitivity Test

The geometry with mesh is shown in Figure 1. It is seen in the figure that L is the length of the pipe with 50 mm, H is the height with 50 mm, and W is the width with 50 mm. So, the heat exchanger is constructed as 50 mm x 50 mm x 50 mm. Here, developing flow effects are also considered for the flow, and pipe length is not provided ten times the pipe diameter. In a turbulent flow, the length needs to be a minimum ten times of the pipe diameter [10]. Here, while the air inlet as in the seen figure is through the Y direction, the water inlet is through the Z direction. The pipe is constructed in the center of the XY plane at the coordinate system. The blue regions are the inlets of air and water in the figure.

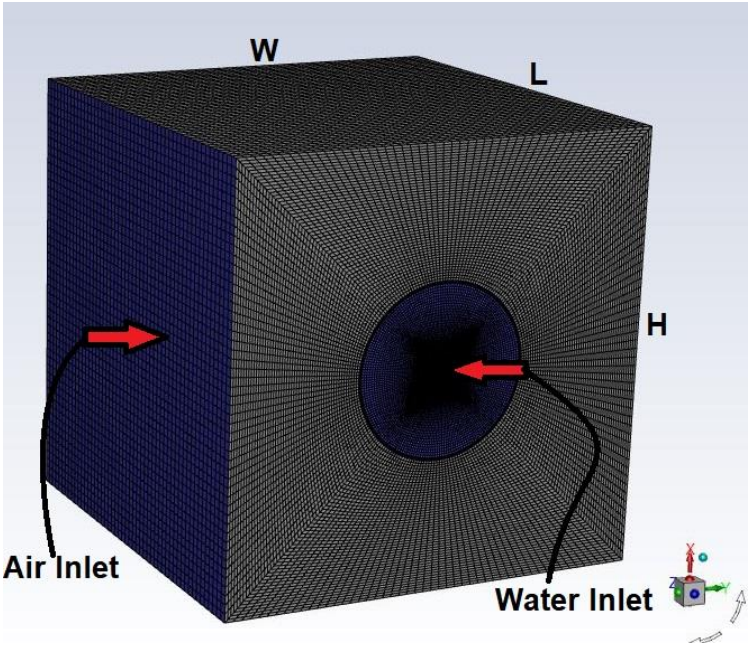

Figure 1. Meshed geometry for the heat exchanger

The hexahedral structured mesh is generated during meshing for the airflow and water flow separately by using the Ansys Fluent meshing tool. The meshing is an important stage during the numerical analysis and uniformity and adequate mesh number are needed to be supplied [11-17].

Detailed mesh views are shown in Figure 2. The general mesh is shown in Figure 2 (a) and a detailed view of the fluid domain is shown in Figure 2 (b). The hexahedral mesh is also used for the circular pipe. The mesh closed the pipe has small elements and it increases from the pipe wall to outward. Also, the mesh in the fluid domain is quite dense to solve the boundary layer. Here, y^+ value and WSS are used to obtain sufficient element numbers.

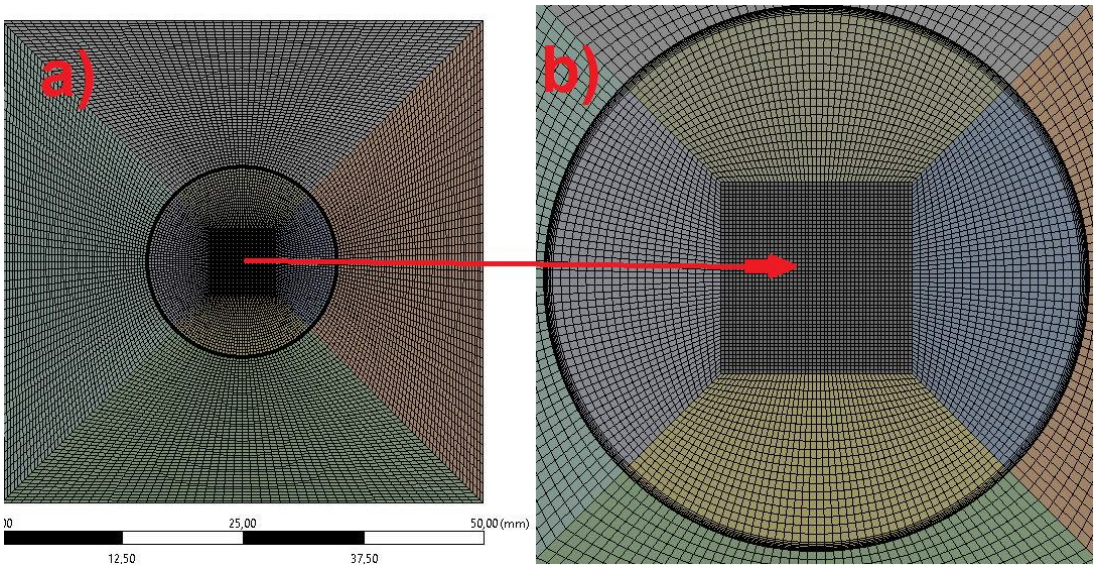

Figure 2. Detailed mesh view of the water inlet side of the heat exchanger

The mesh independency test is shown in Figure 3. This test is performed according to WSS and y^+ values. Blue bars indicate the y^+ values along the pipe surface in turbulent flow, and orange bars indicate the WSS values along the pipe surface. The mesh independency test studies are started by 103268 the element number to 8495087. It is increased within the element size and WSS and y^+ values are reported. In the first mesh, the y^+ value is 3.56 and the WSS value is 7.5 Pa. However, these values decrease to 1.183 and 10.37 Pa with the decrease in the element size. The 7-layer inflation method is constructed in the fluid domain to investigate the boundary layer in detail with the 1.2 growth rate. The dense mesh is generated by the inflation method. Here, the mesh with y^+ value for 1.2 and 10.35 Pa for the WSS is determined for the numerical analysis. The element number is 0.75 mm. Thus it is avoided to perform the numerical calculation with the insufficient mesh element number and it is also avoided the computational cost with large mesh element numbers. y^+ is a nondimensionalized variable with the same formulation of the Re number except for velocity, the velocity is friction velocity for the velocity y^+.

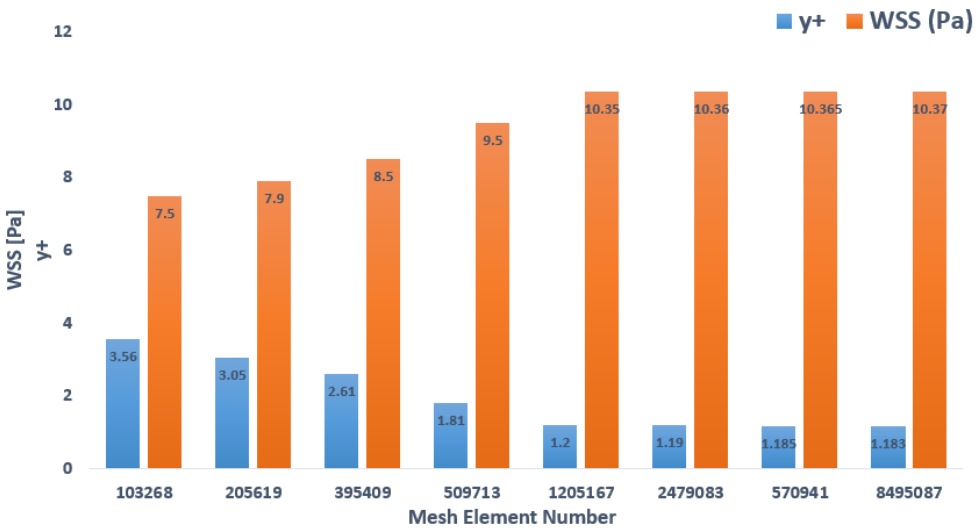

Figure 3. Mesh independency test

2.2 Boundary Conditions, Numerical Methods and Governing Equations

In this study, an incompressible, fully developed, and steady-state flow is studied. The no-slip boundary condition is applied at the pipe and heat exchanger walls. The pipe's inner wall is the heat transfer interface surface for the flows. So heat transfer occurs from hot water inlet to air by this surface.

Table 1. Thermophysical properties of the water

Density (ρ)	983.3	kg/m^3
Viscosity (μ)	0.467 x 10^{-3}	kg/m.s
Thermal Conductivity (*k*)	0.654	W/m.K
Specific Heat (c_p)	4185	J/kg.K

Table 1 presents the thermophysical properties of the water at the temperature of 333 K. The inlet temperature is 333 K for the hot water. Table 2 presents the thermophysical properties of the air at the temperature of 303 K. The inlet temperature is 303 K for the air in this study.

Table 2. Thermophysical properties of the air

Density (ρ)	1.164	kg/m^3
Viscosity (μ)	1.872 x 10^{-5}	kg/m.s
Thermal Conductivity (*k*)	0.02588	W/m.K
Specific Heat (c_p)	1007	J/kg.K

$$\mathrm{Re} = \frac{\rho U D_h}{\mu} \tag{1}$$

Reynolds Number (Re) was used to predict the fluid motion whether it is laminar or turbulent flow in fluid mechanics. Re is the ratio of inertial forces to viscous forces. It is an important dimensionless number. ρ, D_h, U and μ are density [kg/m3], characteristic length [m], velocity [m/s], and dynamic viscosity [Pas] in Equation 1.

The fluid motion was expressed by the governing equations for Newtonian, steady-state, and incompressible, flow. The continuity (conservation of mass) and momentum Equations (2) and (4), respectively [18].

$$\nabla . \vec{V} = 0 \tag{2}$$

$$\nabla = \vec{i}\frac{\partial}{\partial x} + \vec{j}\frac{\partial}{\partial y} + \vec{k}\frac{\partial}{\partial z} \tag{3}$$

The above Equation (2) is known as the Continuity Equation. $\vec{V}$ denotes the velocity vector. In this study, fluid is incompressible, hence, density was constant. Newtonian, incompressible, steady-state momentum equation is governed by Equation (4) for the flow.

$$\rho\left(\vec{V}.\nabla\right)\vec{V} = -\nabla P + \rho\vec{g} + \mu\nabla^2\vec{V} \tag{4}$$

p, μ and $\vec{g}$ are pressure [Pa], dynamic viscosity [Pas], and gravity vector above, respectively.

$$\rho\, c_p\left(\vec{V}.\nabla\right) T = k\,(\nabla^2 T) \tag{5}$$

$$\rho\, c_p \left(u\frac{\partial T}{\partial x} + v\frac{\partial T}{\partial y} + w\frac{\partial T}{\partial z}\right) = k\left(\frac{\partial^2 T}{\partial x^2} + \frac{\partial^2 T}{\partial y^2} + \frac{\partial^2 T}{\partial z^2}\right) \quad (6)$$

The energy equation is given in Equation (5).

$$\tau_w = \mu \frac{du}{dr} \quad (7)$$

In Equation (7); τ_w, μ and $\frac{du}{dr}$ are the shear stress, dynamic viscosity, and shear rate along the r direction perpendicular to the pipe surface respectively.

$$Nu = \frac{h\, D}{k} \quad (8)$$

where k is the thermal conductivity of fluid [W/m.K], D is the diameter of the tube [m], and h is the local heat transfer coefficient [W/m^{2}K] respectively, and the Nusselt number is defined by Equation (8).

The SST k-ω model was used to predict the turbulent flow in this study. Transport equations of the SST k-ω model are given by Equation (9) and Equation (10);

$$\frac{\partial(\rho k)}{\partial t} + \frac{\partial(\rho k u_i)}{\partial x_i} = \frac{\partial}{\partial x_j}\left[\Gamma_k \frac{\partial k}{\partial x_j}\right] + G_k - Y_k + S_k \quad (9)$$

$$\frac{\partial(\rho \omega)}{\partial t} + \frac{\partial(\rho \omega u_j)}{\partial x_i} = \frac{\partial}{\partial x_j}\left[\Gamma_\omega \frac{\partial \omega}{\partial x_j}\right] + G_\omega - Y_\omega + D_\omega + S_\omega \quad (10)$$

k and ω are the kinetic energy and specific dissipation rate in the SST k- ω turbulent model. G_k is defined as the generation of turbulence kinetic energy. G_ω is the generation of ω. Γ_ω and Γ_k are the effective diffusivity of ω and k, respectively. Y_ω and Y_k and are the dissipation of ω and k. S_k and S_ω are user-defined source terms in Equation [19].

Numerical calculations are performed by all second-order upwind discretization to discretize the pressure, momentum, turbulent dissipation rate, and turbulent kinetic energy. The convergence criteria for residuals is chosen 10^{-5}. Flow is steady-state and the energy equation is enabled during calculations.

3. RESULTS AND DISCUSSION

In this study, the aim is to observe the effects of the Re number on the thermal performance of the heat exchanger. The hot inlet is supplied by water at the temperature of 333 K, and the cold inlet is supplied by the air at the temperature of 303 K. Wall Shear Stress (WSS), Skin Friction Coefficient (Cf), Nusselt Number (Nu), heat transfer coefficient (h), and surface temperature are compared according to increase in Re number range from 3165 to 4643. Results are presented for Wall Shear Stress (WSS), Skin Friction Coefficient (Cf), Nusselt Number (Nu), heat transfer coefficient (h), and surface temperature by Re numbers in this section.

Figure 4 presents the variation of velocity for the air passing through the pipe. Air enters the heat exchanger with a velocity of 10 m/s and a temperature of 303 K. As it is seen, the velocity of air is nearly zero at the point that contacts the pipe surface because of the stagnation point that occurs there. It increases on the upper side and the lower side by the narrowing in the airway.

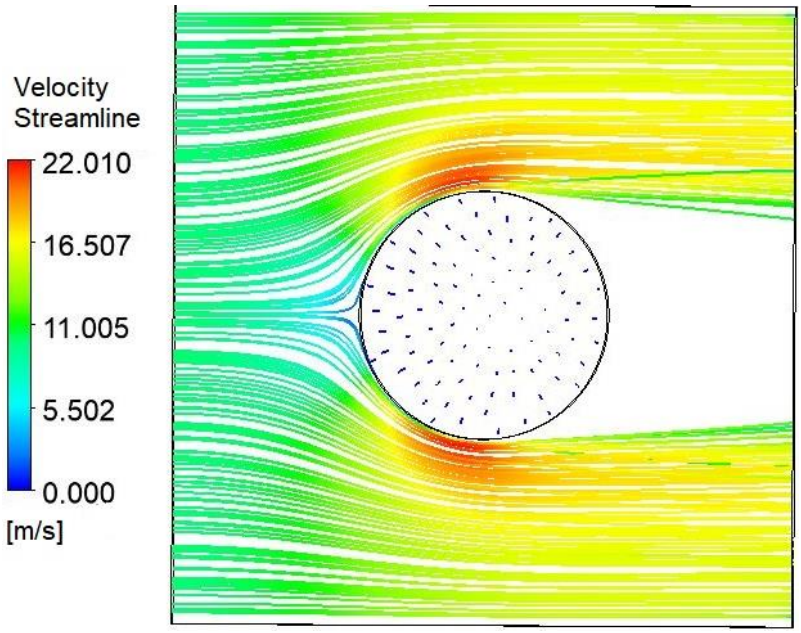

Figure 4. Velocity streamlines for the air passing through the pipe

Figure 5 shows the temperature distribution near the pipe surface for the air and water. The water enters the pipe with 333 K. As seen in the figure the temperature of the air is 303 K closed by the heat exchanger wall. But, the air temperature increases close to the pipe surface because of the heat transfer from the hot water to the air. The temperature of the water is seen as 333 K in the pipe but it decreases to the wall that contact with the air.

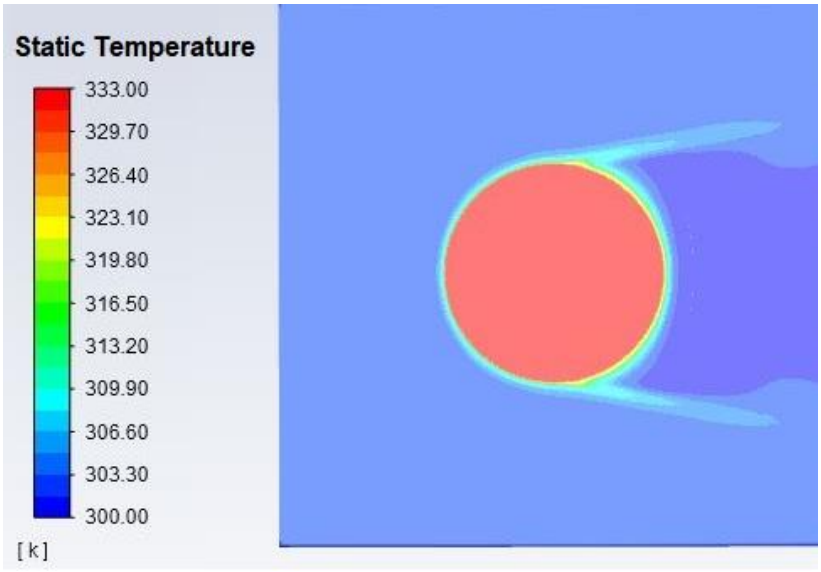

Figure 5. Temperature contour for the air passing through the pipe

Figure 6 shows the variation of the C_f values on the surface of the pipe along the flow direction. The C_f values are similar for the specified Re number for the flows. Due to the range of Re number is in a limited range. C_f values are presented to observe the transition from laminar flow to turbulent flow. C_f value is an indicator to investigate the transition from laminar to turbulent flow [20, 21].

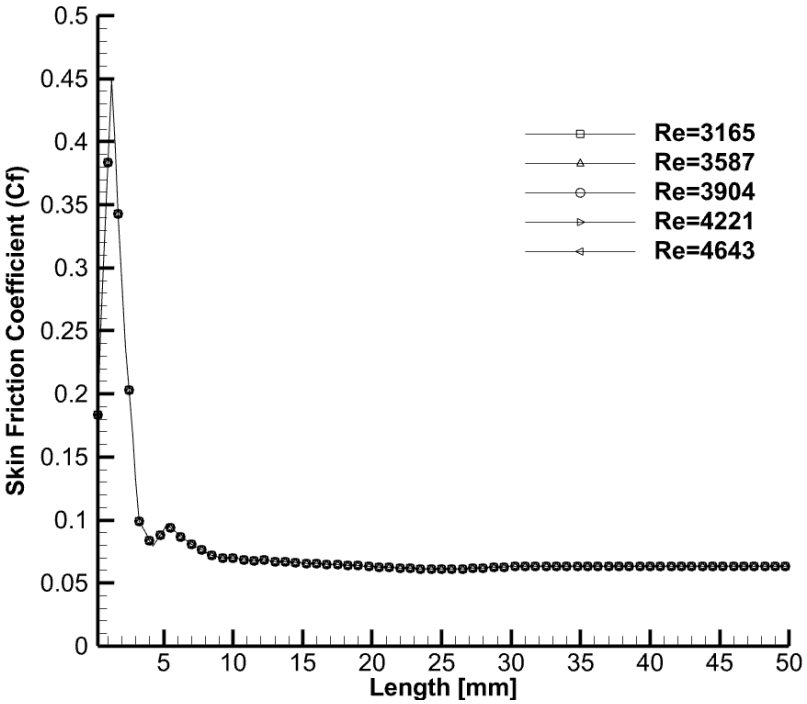

Figure 6. Variation of C_f along the pipe

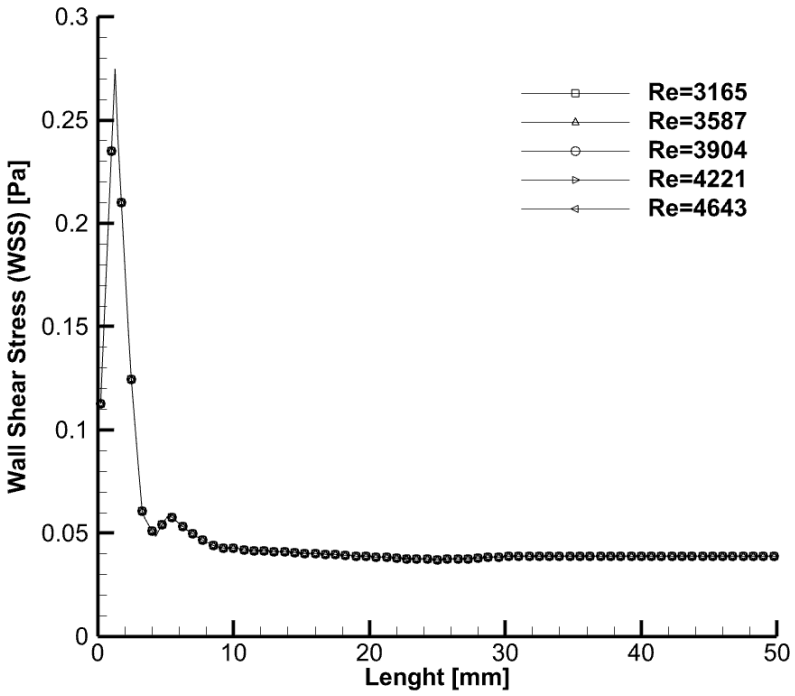

Figure 7. Variation of WSS along the pipe

Figure 7 shows the variation of the WSS values on the surface of the pipe along the flow direction. As seen in the C_f values, WSS values are also similar for the given Re numbers because of a limited range. The transition from laminar to turbulent flow is also seen in the WSS values along the pipe. The WSS is nearly 0.04 Pa during the turbulent flow. In the transition region, it is between 0.05- 0.06 Pa. It reaches its higher value when the flow is fully turbulent, and then it decreases [18].

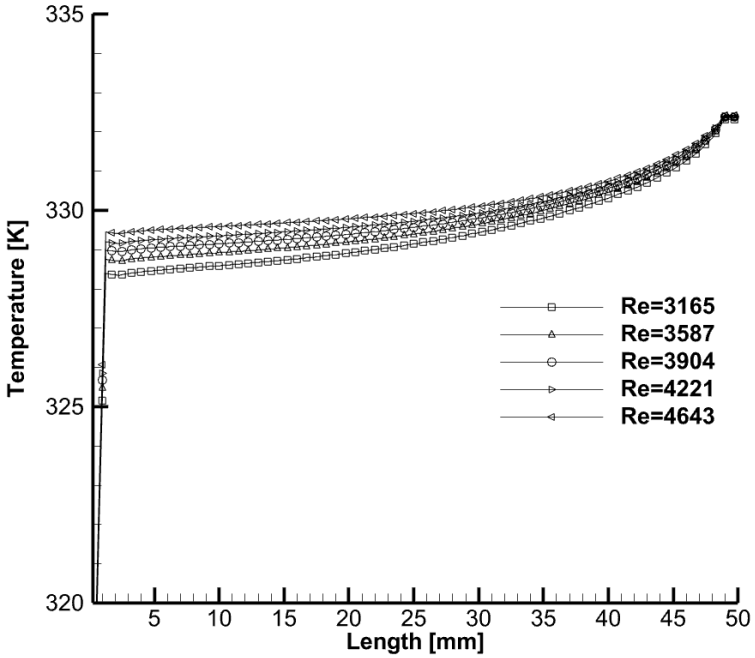

Figure 8. Variation of the surface temperature along the pipe

Figure 8 shows the variation of the surface temperature along the flow direction. Here the highest surface temperature occurs for Re number 4643. The lowest surface temperature occurs for the Re 3165. As expected the increase in Re number also increases the surface temperature along the pipe because of heat transfer from water to the air [22-25]. Here, the increase is approximately 2% for the specified range of Re number for the surface temperature for the specified pipe length. The difference decreases along the flow direction. As seen in the figure temperature difference is higher in the transition region. Even though surface temperature increases, the difference between the flow for specified Re numbers decreases.

Figure 9 shows the variation of the heat transfer coefficient along the flow direction. Here the highest heat transfer coefficient occurs for Re number 4643. The lowest heat transfer coefficient occurs for the Re number 3165. As expected the increase in Re number also increases the heat transfer coefficient because of heat transfer from water to the air. Here, the increase is approximately 2% for the specified range of Re number for the heat transfer coefficient for the specified pipe length. The difference decreases along the flow direction. As seen in the figure heat transfer coefficient difference is higher in the transition region. Even though surface temperature increases, the difference between the flow for specified Re numbers decreases.

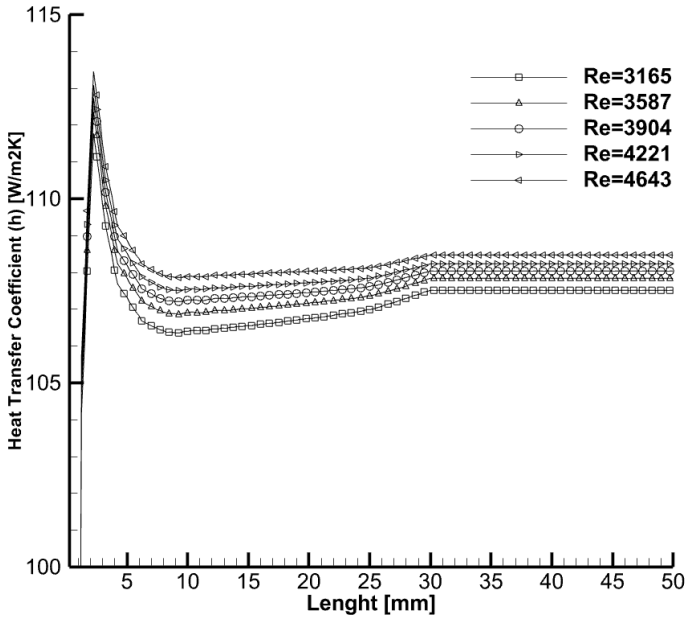

Figure 9. Variation of the heat transfer coefficient along the pipe

Figure 10 shows the variation of the Nu number along the flow direction. Here the highest Nu number occurs for Re number 4643. The lowest Nu number occurs for the Re number 3165. As expected the increase in Re number also increases the Nu number because of heat transfer from water to the air. Here, the increase is approximately 2% for the specified range of Re number for the Nu number for the specified pipe length. The difference decreases along the flow direction. As seen in the figure Nu number difference is higher in the transition region [26–29]. Even though the Nu number increases, the difference between the flow for specified Re numbers decreases.

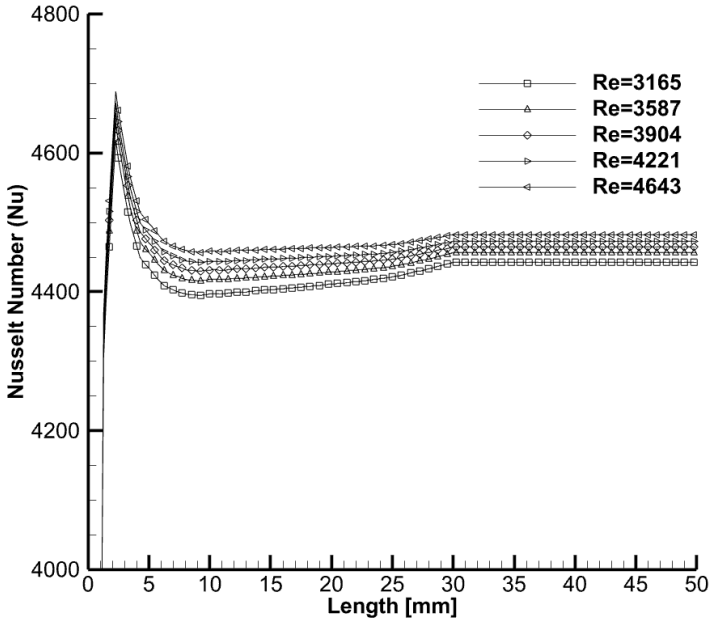

Figure 10. Variation of the Nu number along the pipe

4. CONCLUSION

In this study, a heat exchanger is studied numerically in terms of thermal performance according to the variation of the Re number. The Re number has changed the range from 3165 to 4643 for the five different values. The numerical calculations were repeated for all Re number values with the same boundary conditions except for Re number. The inlet velocity of the air is 10 m/s at the temperature of 303 K and the water temperature is 333 K so the temperature difference is 30 K.

According to the results, the following evaluations were reached:

- When the thermal performance of the heat exchanger is assessed for different Re numbers, the difference is highly low for the given limited ranger.
- The low differences for the investigated results that Wall Shear Stress (WSS), Skin Friction Coefficient (Cf), Nusselt Number (Nu), heat transfer coefficient (h), and surface temperature can be increased by an increase in the Re number. Because of a low limited range for Re numbers studied in the study, therefore differences are observed smaller than 2 %.
- The thermal indicators observed in this study are higher in the transition region according to the laminar and fully turbulent region.
- The increase in Re number increases the heat transfer coefficient and Nu number.

REFERENCES

[1] S. S. Paul, S. J. Ormiston, and M. F. Tachie, “Experimental and numerical investigation of turbulent cross-flow in a staggered tube bundle,” Int. J. Heat Fluid Flow, vol. 29, no. 2, pp. 387–414, 2008, doi: 10.1016/j.ijheatfluidflow.2007.10.001.

[2] J. M. Park, O. J. Kim, S. J. Kim, and Y. C. Shin, “Heat transfer characteristics of circular and elliptic cylinders in cross flow,” Adv. Mech. Eng., vol. 7, no. 11, pp. 1–8, 2015, doi: 10.1177/1687814015619553.

[3] S. Toolthaisong and N. Kasayapanand, “Effect of attack angles on air side thermal and pressure drop of the cross flow heat exchangers with staggered tube arrangement,” Energy Procedia, vol. 34, pp. 417–429, 2013, doi: 10.1016/j.egypro.2013.06.770.

[4] S. Liu and M. Sakr, “A comprehensive review on passive heat transfer enhancements in pipe exchangers,” Renew. Sustain. Energy Rev., vol. 19, pp. 64–81, 2013, doi: 10.1016/j.rser.2012.11.021.

[5] S. A. E. Sayed Ahmed, O. M. Mesalhy, and M. A. Abdelatief, “Flow and heat transfer enhancement in tube heat exchangers,” Heat Mass Transf. und Stoffuebertragung, vol. 51, no. 11, pp. 1607–1630, 2015, doi: 10.1007/s00231-015-1669-1.

[6] Y. Lai, M. Lu, and Q. Wang, “A large eddy simulation of plate-fin and tube heat exchangers with small diameter tubes,” Heat Transf. Eng., vol. 35, no. 11–12, pp. 1137–1143, 2014, doi: 10.1080/01457632.2013.863555.

[7] H. M. S. Bahaidarah, N. K. Anand, and H. C. Chen, “A numerical study of fluid flow and heat transfer over a bank of flat tubes,” Numer. Heat Transf. Part A Appl., vol. 48, no. 4, pp. 359–385, 2005, doi: 10.1080/10407780590957134.

[8] A. Žukauskas, “Heat Transfer from Tubes in Crossflow,” 1972, pp. 93–160.

[9] T. Kim, "Effect of longitudinal pitch on convective heat transfer in crossflow over in-line tube banks," Ann. Nucl. Energy, vol. 57, pp. 209–215, 2013, doi: 10.1016/j.anucene.2013.01.060.

[10] A. P. R. Bruce Roy Munson, T H Okiishi, Wade W Huebsch, Fundamentals of fluid mechanics. Hoboken, NJ: J. Wiley & Sons, 2013.

[11] M. Etli, G. Canbolat, O. Karahan, and M. Koru, "Numerical investigation of patient-specific thoracic aortic aneurysms and comparison with normal subject via computational fluid dynamics (CFD)," Med. Biol. Eng. Comput., vol. 59, no. 1, pp. 71–84, 2021, doi: 10.1007/s11517-020-02287-6.

[12] R. Rzehak and S. Kriebitzsch, "Multiphase CFD-simulation of bubbly pipe flow: A code comparison," Int. J. Multiph. Flow, vol. 68, pp. 135–152, 2015, doi: 10.1016/j.ijmultiphaseflow.2014.09.005.

[13] G. Canbolat, M. Etli, O. Karahan, M. Koru, and E. Korkmaz, "Investigation of vascular flow in a thoracic aorta in terms of flow models and blood rheology via Computational Fluid Dynamics (CFD)," J. Mech. Med. Biol., Aug. 2023, doi: 10.1142/S021951942350094X.

[14] F. Darıcık, G. Canbolat, and M. Koru, "Investigation of a fiber reinforced polymer composite tube by two way coupling fluid-structure interaction," Coupled Syst. Mech., vol. 11, no. 4, pp. 315–333, 2022, doi: 10.12989/csm.2022.11.4.315.

[15] G. Canbolat, A. Yıldızeli, H. A. Köse, and S. Çadırcı, "Düz Bir Plaka Üzerindeki Hidrodinamik ve Isıl Sınır Tabaka Akışının Sayısal Olarak İncelenmesi ve Geçiş Kontrolü," Int. J. Adv. Eng. Pure Sci., vol. 32, no. 4, pp. 390–397, 2020. doi: 10.7240/jeps.636786.

[16] M. Elkarii, R. Boukharfane, S. Benjelloun, and C. Bouallou, "A CFD-based surrogate model for predicting slurry pipe flow pressure drops," Part. Sci. Technol., vol. 41, no. 3, pp. 432–442, 2023. doi: 10.1080/02726351.2022.2110341.

[17] G. Canbolat, A. Yıldızeli, H. A. Köse, and S. Çadırcı, "Numerical Investigation of Transitional Flow over a Flat Plate under Constant Heat Fluxes," Acad. Perspect. Procedia, vol. 1, no. 1, pp. 187–195, Nov. 2018. doi: 10.33793/acperpro.01.01.39.

[18] J. Yunus A and M. Cimbala., Fluid Mechanics Fundamentals and Applications. Boston: HillHigher Education, 2006.

[19] ANSYS, "Ansys Fluent Theory Guide," PA 15317, 2013.

[20] W. H. GIEDT, "Effect of Turbulence Level of Incident Air Stream on Local Heat Transfer and Skin Friction on a Cylinder," J. Aeronaut. Sci., vol. 18, no. 11, pp. 725–730, Nov. 1951, doi: 10.2514/8.2092.

[21] S. T. McClain, B. K. Hodge, and J. P. Bons, "Predicting Skin Friction and Heat Transfer for Turbulent Flow Over Real Gas Turbine Surface Roughness Using the Discrete Element Method," J. Turbomach., vol. 126, no. 2, pp. 259–267, Apr. 2004, doi: 10.1115/1.1740779.

[22] A. Mirabdolah Lavasani, H. Bayat, and T. Maarefdoost, "Experimental study of convective heat transfer from in-line cam shaped tube bank in crossflow," Appl. Therm. Eng., vol. 65, no. 1–2, pp. 85–93, 2014, doi: 10.1016/j.applthermaleng.2013.12.078.

[23] C. K. Mangrulkar, A. S. Dhoble, S. G. Chakrabarty, and U. S. Wankhede, "Experimental and CFD prediction of heat transfer and friction factor characteristics in cross flow tube bank with integral splitter plate," Int. J.

Heat Mass Transf., vol. 104, pp. 964–978, 2017. doi: 10.1016/j.ijheatmasstransfer.2016.09.013.

[24] A. Sohankar, M. Khodadadi, and E. Rangraz, "Control of fluid flow and heat transfer around a square cylinder by uniform suction and blowing at low Reynolds numbers," Comput. Fluids, vol. 109, pp. 155–167, 2015. doi: 10.1016/j.compfluid.2014.12.020.

[25] A. Lemouedda, A. Schmid, E. Franz, M. Breuer, and A. Delgado, "Numerical investigations for the optimization of serrated finned-tube heat exchangers," Appl. Therm. Eng., vol. 31, no. 8–9, pp. 1393–1401, 2011. doi: 10.1016/j.applthermaleng.2010.12.035.

[26] Y. Wang, L. C. Wang, Z. M. Lin, Y. H. Yao, and L. B. Wang, "The condition requiring conjugate numerical method in study of heat transfer characteristics of tube bank fin heat exchanger," Int. J. Heat Mass Transf., vol. 55, no. 9–10, pp. 2353–2364, 2012. doi: 10.1016/j.ijheatmasstransfer.2012.01.029.

[27] C. K. Mangrulkar, A. S. Dhoble, S. Chamoli, A. Gupta, and V. B. Gawande, "Recent advancement in heat transfer and fluid flow characteristics in cross flow heat exchangers," Renew. Sustain. Energy Rev., vol. 113, no. November 2018, p. 109220, 2019. doi: 10.1016/j.rser.2019.06.027.

[28] L. Zhao, X. Gu, L. Gao, and Z. Yang, "Numerical study on airside thermal-hydraulic performance of rectangular finned elliptical tube heat exchanger with large row number in turbulent flow regime," Int. J. Heat Mass Transf., vol. 114, pp. 1314–1330, 2017. doi: 10.1016/j.ijheatmasstransfer.2017.06.049.

[29] F. Duan, K. W. Song, H. R. Li, L. M. Chang, Y. H. Zhang, and L. B. Wang, "Numerical study of laminar flow and heat transfer characteristics in the fin side of the intermittent wavy finned flat tube heat exchanger," Appl. Therm. Eng., vol. 103, pp. 112–127, 2016. doi: 10.1016/j.applthermaleng.2016.04.081.

ALKU Journal of Science 2023, Sayı 5(3): 131-148
e-ISSN: 2667-7814

Original Article

Amorf Polimerler

Özge Kılınç[1*], Nil Toplan[1]
[1] *Sakarya Üniversitesi, Mühendislik Fakültesi, Metalurji ve Malzeme Mühendisliği, Sakarya, Türkiye*
**ozgekilinc1998@gmail.com*

Özet

Amorf polimerler, moleküllerin düzenli ve yapılandırılmış bir düzenlemesine sahip olan kristalin polimerlerin aksine, rastgele ve düzensiz bir molekül düzenlemesine sahiptir. Amorf polimerler, kristal kristalli bir yapıya sahip olmadıklarından daha esnektirler. Bu malzeme grubu; şeffaflık, esneklik ve darbe direncinin önemli olduğu uygulamalarda yaygın olarak kullanılır. Kristalli yapıya sahip olmadıkları için ışığı dağıtmazlar ki bu da onları lensler veya ekranlar gibi optik netliğin önemli olduğu uygulamalarda kullanım için ideal kılar. Amorf polimerlerin yapısal eksiklikleri (düzensiz moleküler yapı, düşük sertlik, erime noktası ve mekanik dayanıklılık, yavaş kristallenme eğilimi gibi) işlemede tekdüzelik elde etmeyi zorlaştırabileceğinden, işlenmeleri kristal polimerlere göre daha zor olabilir. Ayrıca kristal polimerlerden daha düşük erime noktalarına sahip olduklarından, yüksek sıcaklıklarda deformasyona veya erimeye karşı daha duyarlıdırlar. Teknoloji ilerledikçe ve yeni malzemeler geliştirildikçe, amorf polimerler, ambalajdan elektroniğe ve tıbbi cihazlara kadar uzanan endüstrilerde büyük olasılıkla önemli rol oynamaya devam edecektir. Bu makale kapsamında amorf ve kristalin polimerlerin yapısı ve çeşitleri araştırılmış, kıyaslamalı bir şekilde polimerlerdeki amorf ve kristalin düzen incelenmiş, polimerlerin genel olarak sınıflandırılması yapılmış ve fiziksel özelliklerine de yer verilmiştir.

Anahtar Kelimeler: Amorf, Polimer, Amorf Polimerler, Kristalin Polimerler

Amorphous Polymers

Abstract

Amorphous polymers have a random and disordered arrangement of molecules, unlike crystalline polymers, which have an ordered and structured arrangement of molecules. Amorphous polymers are more flexible as they do not have a crystalline structure. This material group is commonly used in applications where transparency, flexibility, and impact resistance are important. Since they do not have a crystalline structure, they do not scatter light, making them ideal for use in applications where optical clarity is important, such as in lenses or displays. Amorphous polymers can be more difficult to process than crystalline polymers, as their structural deficiencies can make it difficult to achieve uniformity in processing. Also, since they have lower melting points than crystalline polymers, they are more susceptible to deformation or melting at high temperatures. As technology advances and new materials are developed, amorphous polymers will likely continue to play an important role in industries ranging from packaging to electronics to medical devices. Within the scope of this article, the structure and types of amorphous and crystalline polymers were investigated, and they have been included in the article in a comparative way. The amorphous and crystalline orders of the polymers were investigated. Polymers have been broadly classified, and their physical properties have been studied.

Keywords: Amorphous, Polymer, Amorphous Polymers, Crystalline Polymers.

Geliş/Received: 20 Mayıs/May 2023
Kabul Ediliş/Accepted: 10 Ekim/October 2023

1. GİRİŞ

Amorf polimerler, düzenli bir yapıya sahip olmayan türde polimerik malzemelerdir. Oldukça düzenli, tekrar eden bir yapıya sahip olan kristalli polimerlerin aksine, amorf polimerler düzensiz, rastgele bir molekül yerleşimine sahiptir. Genellikle daha esnek ve şeffaf olmak gibi kristal polimerlerden farklı mekanik ve fiziksel özelliklere sahiptirler. Amorf polimerler, paketleme, elektronik, otomotiv ve tıbbi cihazların dahil olduğu çeşitli endüstrilerde yaygın olarak kullanılırlar. Çok çeşitli şekil ve boyutlarda kalıplanabilirler ve benzersiz özellikleri (şeffaflık, esneklik, gelişmiş darbe mukavemeti ve elektriksel yalıtım, kolay işlenebilirlik, düşük yoğunluk ve kimyasal direnç gibi) onları belirli uygulamalar için ideal kılar. Örneğin, polikarbonat, darbelere karşı yüksek direnciyle bilinen ve yaygın olarak kullanılan amorf bir polimerdir ve bu özelliği sayesinde güvenlik camları, elektronik bileşenler ve dayanıklılığın önemli olduğu diğer uygulamalarda kullanılabilmektedir [1, 2].

Moleküler yapısı kristallere özgü periyodik ve düzenli bir yapıdan oluşmayan bütün maddeler amorf olarak bilinir. Dolayısı ile amorf bir katıda onu oluşturan atom veya moleküllerde belirli bir düzen mevcut değildir. Amorf katılar, bir sıvıyı katılaşma noktasının altına soğutarak ve molekülün hareketliliğini engelleyerek/azaltarak elde edilebilirler. Örneğin silika, kristal bir katının kafesini oluşturan polar yapılı kovalent bir moleküldür. Silikanın kristal yapısının füzyon işlemi sırasında yok edilmesi ve iyonlarının serbestçe hareket etmesine izin verilmesi durumunda amorf hale dönüştürülebilir. Erimiş formun soğumasıyla, viskozite yükselerek kristalin yeniden oluşmasını engeller. Malzeme soğuduktan sonra katı hale geri döner ancak iç yapısı farklıdır ve düzensiz hale gelmiştir [1]. Amorfizasyon, kristal halin amorf hale dönüşmesi olarak tanımlanabilir. Amorfizasyon çeşitli yollarla gerçekleştirilebilir (örneğin, yüksek enerjili elektronlar veya iyonlarla bombardıman, kısa lazer darbeleriyle ışınlama ve katı faz reaksiyonları vb. gibi). Kristal bir katı, malzemenin erime noktasının altındaki bir sıcaklıkta sıkıştırıldığında, olası kristal faz değişiklikleri başlayamaz veya bitemez ki bu durum, basınca bağlı amorfizasyon (PIA) olarak bilinir [1]. Mevcut derleme makalesinde amorf polimerlerin yapısı ve özellikleri kapsamlı olarak incelenmiş ve polimerlerdeki amorf ve kristalin bölgelerin polimere sağladığı avantaj ve dezavantajlar yorumlanarak potansiyel kullanım alanları konusunda bilgiler verilmiştir.

2. POLİMERLER

Polimerler birden fazla molekülün bir araya gelerek oluşturduğu monomerlerin tekrarlanır şekilde bir zincir halinde dizilmesiyle oluşan makromoleküler yapılardır. Latince'de "poly" çok ve "mer" parçacık anlamına gelir. Bu şekilde birçok molekülün bir araya gelerek polimerik yapıyı oluşturması mekanizmasına polimerizasyon denmektedir [3]. Polimerler, yüksek moleküler ağırlıklarından dolayı diğer malzeme türlerinden farklıdır. Atomların farklı faz hallerinde nasıl davrandıkları polimer boyutunun önemli bir sonucudur. Daha küçük moleküllü bileşikler, maddenin üç durumuna (katı, sıvı ve gaz) sahiptir. Bir katının tanecikleri birbirine yakın şekilde istiflenmiş ve çok az hareketliliğe sahipken, bir sıvının parçacıkları daha gevşek şekilde paketlenmiştir ve birbirleri arasında kolaylıkla kayabilirler. Bir gazın parçacıkları ise çok daha gevşek bir şekilde paketlenmiş olup, çok büyük bir enerjiyle hareket ederler. Polimerler sadece katı olarak düşünülmezler ve amorf ve kristalin olmak üzere iki türe ayrılırlar. Bazı polimerik katılar aynı anda hem amorf hem de kristalin (kısmi kristalin yapı) olabilir [4]. Tamamen kristalin yapıda bir polimer olmamasına rağmen, bazı polimerler belli koşullar altında %100 amorf olabilir ve yine aynı sebeple, amorf bölgelerin yanı sıra kristalin bölgelere de sahip olan polimerlere yarı kristalin polimerler denir [5].

2.1 Polimerlerin Sınıflandırılması

Polimerik malzemeler; elde edilişlerine, kimyasal bileşimlerine, yapılarına, üretim yöntemlerine, bağ yapılarına, işleme şekilleri ve/veya çözücülere karşı gösterdikleri tepkilere ve fiziksel durumlarına göre farklı şekillerde sınıflandırılabilir. Molekül zincirlerinin dizilişlerine göre düzenlenme şekilleri polimerlerin fiziksel yapısını meydana getirir ki bu sebeple polimerler; amorf, kristalin ve kısmi kristalin

olmak üzere üç kısma ayrılırlar. Genel olarak termoplastikler, termosetler ve elastomerler olmak üzere üç farklı polimer çeşidi bulunmaktadır.

Termoplastikler: Bu türdeki polimerler genellikle kristalin veya amorf halde bulunurlar. Genellikle esnek olmalarına rağmen, dayanıklılıkları düşüktür ve genellikle plastik üretiminde kullanılırlar. Propilen (C_3H_6), fosil yakıtlardan elde edilebilen bir termoplastik polimerin monomeridir [1]. Termoplastik polimerler ısıtıldıklarında şekillendirilebilen veya kalıplanabilen ve soğutulduğunda önemli bir kimyasal değişime uğramadan katı duruma dönebilen bir polimer kategorisi olup belli bir erime noktasına sahiptirler. Bu özellik, termoplastiklerin ekstrüzyon, enjeksiyonlu kalıplama ve şişirmeli kalıplama gibi yöntemlerle işlenmesine ve farklı şekillerde üretilmesine olanak tanımaktadır [6].

Termosetler: Termosetler, yüksek sıcaklıkta bir kimyasal reaksiyonla sertleşerek (polimerizasyon) ısının etkisiyle kalıcı olarak şekil değiştiren malzemelerdir. Bu reaksiyon sonucunda moleküler zincirler arasında çapraz bağlar oluşur ve polimer daha yüksek sıcaklıklara dayanıklı ve mekanik olarak dayanıklı hale gelir. Bu nedenle, termosetler bir kez sertleştiklerinde, yeniden ısıtıldıklarında erimez veya şekil değiştirmezler. Termosetler, örneğin epoksi reçineleri, fenolik reçineler, poliüretanlar ve bazı polyesterler gibi birçok farklı malzeme türünü içerir. Termoplastiklere göre daha dayanıklı olup, araç, yedek parça, araba tamponları ve çamurluk parça üretiminde kullanılırlar. Dayanıklı olsalar da aşırı ısıyla karşılaşmaları halinde ufak darbelerde bile parçalanabilirler. Termoset ürünler dikkatli kullanıldıklarında uzun yıllar sağlamlığını koruyabilir [7, 8, 9].

Elastomerler: Elastomerler, elastik özelliklere sahip olan polimer malzemelerdir [10]. Moleküller arası kuvvetleri küçük (elastomerlerin esnekliğini sağlayan zayıf kovalent bağlar veya van der waals kuvvetleri), bağ enerjileri düşük ve moleküllerinde esnek zincirler bulunması halinde bir polimer, elastomer özellik gösterir [11]. Elastomerler, oda sıcaklığında kuvvet uygulanması halinde uzama gösteren ve kuvvet kalktığında da eski haline dönebilen malzemelerdir (paket lastiği, kauçuk vb. gibi). Arabaların lastik, şasi süspansiyonu, motor ve şanzıman parçaları, contalar ve sızdırmazlık elemanları, direksiyon gibi kısımlarında büyük oranda elastomer bulunmaktadır [7, 12].

Polimerleri Şekil 1'deki gibi çeşitli şekilde sınıflandırmak (elde edilişlerine, kimyasal bileşimine, yapılarına, sentez yöntemlerine, bağ yapılarına, işleme şekillerine, fiziksel durumlarına göre) mümkündür. Elde edilişlerine göre polimerler doğal, yarı sentetik ve sentetik olmak üzere 3'e ayrılabilmektedir. Doğal polimerlere selüloz, nişasta, keratin ve lateks (kauçuk) örnek verilebilir. Sentetik polimerlere polietilen, polipropilen, polivinil klorür ve naylon; yarı sentetik polimerlere ise selüloit, rayon ve yarı sentetik kauçuklar örnek verilebilmektedir [13]. Polimerler kimyasal bileşimine göre organik (örn. polietilen, polipropilen, polivinil klorür, polistiren ve poliakrilonitril) ve inorganik (örn. silikon kauçuk, polisiloksanlar, fosfor, bor ve titanyum polimerleri) olarak da sınıflandırılabilmektedir [14]. Yapılarına göre sınıflandırılabilen polimerler kapsamındaki alt gruplar homopolimerler, alternatif kopolimerler, rastgele kopolimerler, blok polimerler ve aşı polimerlerdir. Homopolimerler, aynı türden tek bir monomer biriminin zincir halinde birleşmesiyle oluşurlar ve örnek olarak polietilen ve polipropilen verilebilir. Alternatif kopolimerler, iki veya daha fazla farklı monomer türünün sırayla zincirde birleştiği polimerler olup örnek olarak stiren-bütadien-stiren verilebilir. Rastgele kopolimerler, farklı monomer türlerinin rasgele sıralandığı polimerlerdir ve örnek olarak akrilonitril-stiren verilebilir. Blok kopolimerler, iki veya daha fazla farklı monomer türünün ardışık olarak ayrı bloklar halinde zincirde birleştiği polimerlerdir ve polistiren-bütadien bir blok kopolimer örneğidir. Aşı polimerleri, bir ana zincir üzerine farklı bir monomerin uygulandığı ve bu monomerin yan zincirlerle ana zincire bağlandığı polimerlerdir ve polistiren-graft-polietilen örnek olarak verilebilir [15]. Sentez yöntemlerine göre sınıflandırılan kondenzasyon polimerleri, sentez sırasında monomerlerin birleşmesi sonucu çeşitli yan ürünler (su gibi) oluşturan türde polimerler olup bu tür polimerler, monomerler arasında çift bağların veya reaktif grupların bulunması nedeniyle oluşmaktadır. Bunlara örnek olarak naylon, polyester, poliüretan ve polikarbonat verilebilir. Diğer bir alt başlık ise zincir (katılma) polimerleri olup sentez sırasında monomerlerin birleşerek polimer zincirlerini oluşturduğu bir tür polimerdir. Bu tür polimerlerde reaksiyonlar sonucu yan ürünler genellikle oluşmamaktadır ve örnek olarak polietilen, polipropilen ve polivinil klorür verilebilir

[16, 17]. Bağ yapılarına göre doğrusal (lineer) polimerlere yüksek yoğunluklu polietilen (HDPE), dallanmış polimere örnek olarak düşük yoğunluklu polietilen (LDPE), çapraz bağlı polimere ise vulkanize kauçuk örnekleri verilebilir. İşleme şekilleri ve/veya çözücülere karşı gösterdikleri davranışlara göre polimerler elastomerler, fiberler, termoset polimerler, termoplastik polimerler ve elastomerler olarak 5'e ayrılır. Fiziksel durumlarına göre ise amorf, kristalin ve kısmi kristalin olmak üzere 3'e ayrılmaktadırlar [18].

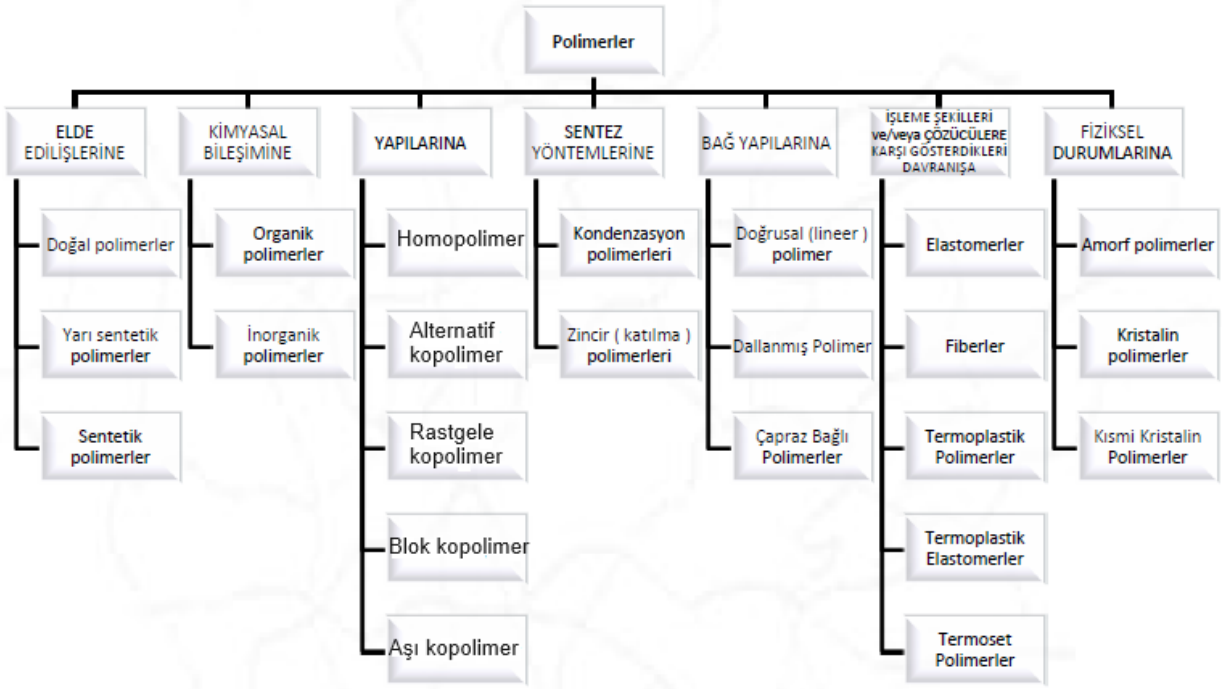

Şekil 1. Polimerlerin sınıflandırılması [18]

2.2 Polimerlerin Fiziksel Özellikleri

Polimerlerin kristalin, ısıl, çözünürlük, akışkanlık direnci (viskozite), uçuculuk, yüzey gerilimi, sürtünme ve mekanik özellikler olmak üzere çeşitli fiziksel özellikleri mevcuttur [19]. Çoğu fiziksel özellik, polimeri oluşturan moleküller arası kuvvetlere bağlıdır. Kuvvetli polar gruplara sahip bir molekülün komşuları üzerindeki çekim kuvveti yüksektir ve bu durum, erime ve kaynama noktalarının yükselmesine sebep olur. Bir polimerde moleküller arası kuvvetler büyükse, bağ enerjileri yüksek ve kalabalık yan gruplar mevcut ise tipik plastik özelliği gözlenir ki bu durum; polimerin bağ enerjisinin yüksek olmasına, gerilmeye karşı direnç göstermesine ve iyi mekanik özelliklere sahip olmasına yol açar [20]. Fiziksel özellikler; polimerin kristal, yarı kristal ve amorf denilen yapıları, ısıl iletkenliği, genleşmesi ve ısıya karşı dayanıklılığı ile erime/sertleşme noktası ve yanma oranı gibi ısıl davranışlarının yanı sıra çözünürlükleri ile de ilgilidir [19].

2.2.1 Polimerlerin kristalleşmesi

Gerçekte polimerlerin çoğu kristal katı ile viskozitesi yüksek sıvı amorf yapı (şekilsiz, düzensiz dizilim) karışımlarından oluşur. Genellikle tekrarlanan birimleri özdeş ve küçük olan zincirler bir kristal örgüsü oluşturabilirken, çeşitli büyüklükteki birimlerin rasgele bağlanmasıyla elde edilen zincirler ise kristalleşemezler [19].

Kristalin yapı, polimere sertliğin yanı sıra ısıl ve mekanik dayanıklılık sağlarken, polimerin çözünürlük, yayılma, geçirgenlik, boyanabilirlik, plastikleştiriciyi kabul etme gibi özelliklerinde önemli oranda azalmaya neden olur. Örneğin %5-10 kristalin bir polimerde hala yüksek oranda esneklik vardır ve

malzeme yumuşak ve kauçuğumsu iken; %20-60 kristalin yapıdaki polimerik bir malzeme ise toktur ve %70-90 kristalin yapılı bir malzeme ise sert ve dayanıklı bir yapıdadır. Kısacası bir polimerin kristalleşme derecesi moleküllerindeki yapısal birimlerinin kristal düzenine kolayca girebilmesine, zincirleri arasındaki çekim kuvvetlerine ve zincirlerinin sertliğine bağlı olup; ısıl, mekanik ve diğer fiziksel özelliklerini de büyük ölçüde etkiler [19].

Molekül ağırlığı, sıcaklık, soğutma hızı, basınç ve çekirdekleştirici ajanlar gibi faktörler polimerlerde kristalleşmeyi etkilemektedir [20]. Yüksek molekül ağırlığına sahip polimerler daha uzun zincirlere sahip oldukları için daha kolay kristalleşme eğilimindedir ve daha sıkı bir şekilde bir araya gelebilirler [21]. Bir polimer eriyiğinin veya bir çözeltinin soğutulması kristal bölgelerin oluşumunu teşvik ederek kristalleşmeyi tetikleyebilmektedir. Yavaş soğutma hızı ile polimer zincirlerinin kristal yapılar halinde düzenlemeleri zaman almaktadır. Yüksek basınç, özellikle yüksek performanslı malzemelerde kristalleşmeyi desteklemektedir. Çekirdekleştirici ajanlar olarak bilinen katkı maddeleri, kristal yapıların ilk oluşumu için alanlar sağlayarak kristalizasyon sürecini geliştirmek için kullanılmaktadır [22].

Polimer ana zincirine bağlı fonksiyonel gruplar, C-C bağı etrafındaki dönmeyi engelleyerek zinciri sertleştirir ki bu da kristalleşmeyi engeller. Polistiren (PS), poli (metil metakrilat) (PMMA) ve poli (vinil klorür) (PVC) gibi polimerlerde kristalleşme eğilimi çok düşüktür. Sert ve halkalı gruplar ile esnek olmayan zincirler kristalleşmeyi güçleştirir. Örneğin poli (etilen tereftalat) ve selüloz zincirlerinde bulunan aromatik ve halkalı gruplarla, yan zincirdeki polarite sertlik (politetrafloroetilen (teflon)'deki F atomları, PVC'deki Cl atomları, poliakrilonitril (PAN)'deki C≡N yan grupları esnekliği düşürür) oluşturur. Dolayısıyla hareketliliği engelleyen gruplar ile sert ve halkalı gruplar ve çapraz bağlar, kristalleşmeyi önler. HDPE zincirinde yinelenen birimler küçük ve özdeş olduğundan kolayca kristalleşebilir. Zincirler arasındaki çekim kuvveti zayıf olduğu halde, zincirlerin esnek olması kristalleşmeye yardım eder. LDPE'de olduğu gibi kısa dallanma, düzeni azaltarak, kristal oranını düşürür. Dallanma düzenli ise (polipropilendeki gibi) kristalin yüzdesi artar. Bir polimerde kristal yüzdesi ve kristalleşme türü, deneysel olarak; yoğunluk, X-ışınları, nötron kırılması, elektron difraksiyonu, kızılötesi (IR) ve nükleer manyetik rezonans (NMR) yöntemleri ile bulunabilirken, elektron mikroskobu ile de kristalin ve amorf bölgeleri gözlenebilir [19, 23].

2.2.2 Polimerlerin moleküler düzeni

Polimerler katı, sıvı veya çözelti halinde bulunabilirler. Bu durumlardaki yapı farklılıkları mekanik, ısıl ve fiziksel özellikleri ile ilgilidir. Polimerlerin bu yapılardaki kimyasal formülü ve morfolojisi önemlidir. Morfoloji; polimerin katı halinde bulunan kristalin veya amorf bölgelerin varlığı, yerleşme düzeni, büyüklüğü gibi özelliklerini kapsar. Katı haldeki bir polimerde iki temel düzen vardır ki bunlar, amorf yapı ve kristalin yapıdır [24]. Şekil 2'de bir polimer zinciri üzerindeki kristalin ve amorf bölgeler temsili olarak gösterilmiştir.

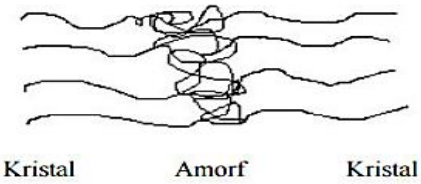

Şekil 2. Polimer zinciri üzerindeki kristal ve amorf bölgeler [18]

2.2.3 Polimerlerin ısıl davranışı

Amorf yapılı polimerler ısıtıldıklarında aniden erimezler. Bunun yerine, malzemenin daha az camsı ve daha çok kauçuğa benzediği veya tam tersi olduğu bir sıcaklık aralığına ulaşırlar. Amorf polimerlerin bir erime noktası yoktur ve bir camsı geçiş sıcaklığına (Tg) sahiptirler. Tg, uzun menzilli koordineli moleküler hareket nedeniyle polimerin yumuşadığı sıcaklıktır. Tg'nin altındaki sıcaklıklarda amorf

polimer zincirlerinin uzayda hareket edemediği söylenebilir. Bu durum sert ve kırılgan olan camsı durumu ortaya çıkarır. Sıcaklık Tg'nin üzerine çıktığında birbirine dolanmış haldeki zincirler hareket edebilir. Bu durumda amorf bir polimer yumuşak ve esnek, kauçuğumsu bir durum oluşturur. Yüksek kristalliğe eğilimli olan polimerler; sert, yüksek erime noktasına sahip ve solvent (çözücü) penetrasyonundan (nüfuziyetinden) daha az etkilenirken, yüksek amorfluğa eğilimli olanlar ise daha yumuşak bir yapıya ve camsı geçiş sıcaklığına sahiptir [4,25]. Kristal yapıya sahip bir polimer sağlam bir yapıda iken, amorf yapıdaki ise kolay şekil alabilen bir yapıdadır. Bir polimer soğutulursa kristalleşme ve camsılaşma olmak üzere birbirinden farklı iki mekanizma ile kristallenir [18].

Bazı polimerler tamamıyla amorf olduğu için erime sıcaklığından (Te) söz etmek mümkün değildir. Teorik olarak, tamamen kristalin yapıdaki polimerlerde de Tg yoktur. Ancak, genellikle, polimerler yarı kristal yapıda olduğundan, çoğu polimerde bu iki sıcaklık da gözlenir [18,26]. Polimerlerin hacim-sıcaklık davranışı Şekil 3'teki gibi olup, burada, erimiş halde bulunan sıcak haldeki polimer soğutulursa, Te'nin altındaki sıcaklıklarda kristalleşme başlar ve bir miktar şekilsiz madde içeren çok kristalli bir kütle elde edilir. Soğutma hızlı yapıldığında ise polimerin çoğu kristalleşmeden Te'nin altına inebilir ve termodinamik bakımdan yarı kararlı aşırı-soğumuş ve şekilsiz bir madde elde edilir. Moleküllerin dönme ve bükülme hareketleri sürdüğü için polimer yumuşak ve kauçuğumsu bir haldedir. Sıcaklık daha da düşürülürse, moleküllerin dönme ve bükülme hareketleri yavaşlar ve Tg'nin altında da tamamen durur.

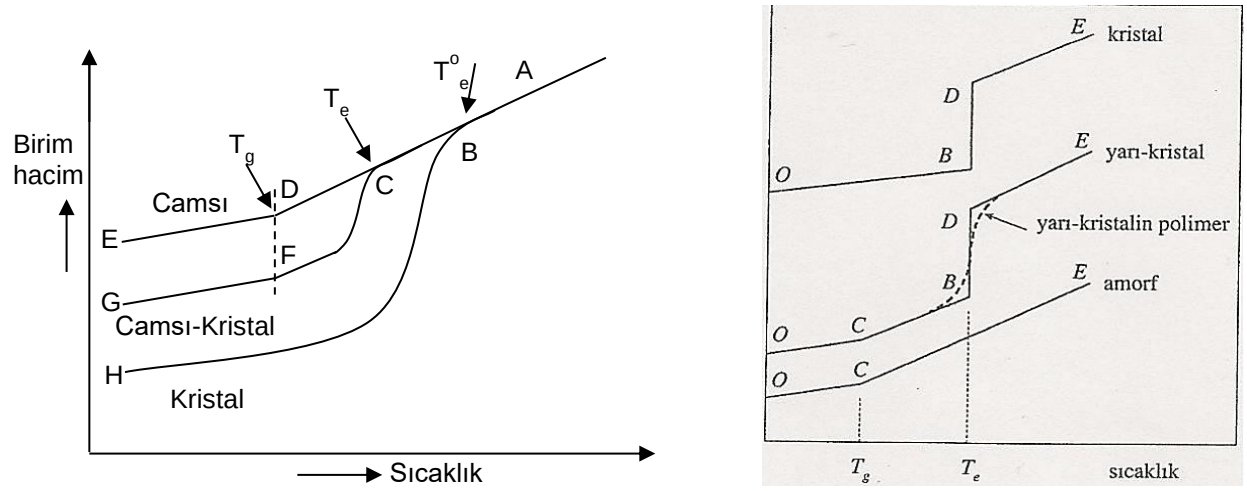

Şekil 3. (a) Bir polimerin hacim ve sıcaklık eğrisi ve (b) Amorf, yarı kristal ve kristal maddelerin sıcaklık-özgül hacim değişimi [19]

Polimer zinciri farklı yapı birimlerinden oluşuyor ise, yani amorf yapıda bir polimer söz konusu ise, hacim değişimi ACD eğrisini izler ve sadece Tg geçişi gözlenir. Yapıda kristalin bölgeler bulunmadığı için erime noktası gözlenemez. Tümüyle kristal bir polimer ise ABH eğrisini izleyip, sadece T°'e geçişi gösterir. Düzensiz zincirleri olmadığı için Tg gözlenemez. Polimerlerin çoğu Te sıcaklığında bir miktar kristalleştiği için genellikle her iki geçiş sıcaklığını da gösterir (ACFG eğrisi) çünkü hem kristalin hem de amorf halleri bulunur (Şekil 3.a). Şekil 3.b'de amorf, yarı kristal ve kristal maddeler için özgül hacim-sıcaklık ilişkileri verilmiştir. Kristal yapıdaki maddelerin özgül hacimleri erime noktasına kadar OB doğrusundaki gibi belirli bir hızla artar. Erime noktasına ulaşıldığında (B noktası) kristal yapı bozunarak madde erir. Erime sırasındaki katı-sıvı faz değişimi nedeniyle hacimde belirgin bir artış (BD doğrusu) gözlenir [18].

2.2.4 Polimerlerin çözünürlüğü

Lewis asit gruplarını içeren polimer molekülleri, Lewis bazı niteliğinde olan çözücülerde kolayca çözünür. Kristal yapılı polimerlerin çözünürlüğü, amorf olanlarınkinden çok daha düşüktür. Polar

olmayan kristal yapılı bir polimer ise Te'nin altında hiçbir çözücüde çözünmez. Polimer ile çözücünün kohezif enerji yoğunluğu (KEY) değerleri aynı olsa bile, çözünme olayı yeterince ısı alan (endotermik) olduğu için, polimerin çözünmediği görülür. Bu durumda çözücü, amorf bölgelere nüfuz ederek polimeri şişirse de kristal yapıyı çözemeyeceğinden polimerin çözünebilmesi için polimer/çözücü karışımının kristallerin erime noktasına kadar ısıtmak da gerekir [19].

Yapılan bir çalışmada HDPE, polipropilen, polibütadien ve polietilentereftalat kullanılarak çözünürlük üzerinde kristalin bölgelerin önemli bir parametre olduğu doğrulanmıştır. Çalışmada yavaş soğutulan yarı kristal polimerlerin kristalliği daha yüksek olduğu için daha düşük bir yayılma göstermiştir. Örneğin en düşük çözünürlüğe sahip olan HDPE hızlı soğutulduğunda 17,5 mg/g çözünürlüğe sahipken yavaş soğutulduğunda 11,9 mg/g çözünürlüğe, en yüksek çözünürlüğe sahip olan PET hızlı soğutulduğunda 74,3 mg/g, yavaş soğutulduğunda ise 37,7 mg/g çözünürlüğe sahip olmuştur [27].

2.3 Mikromekanik Davranış

Yük altındaki amorf polimerler; çatlaklar, deformasyon bantları veya kayma bantları gibi şekil değiştirme (deformasyon) çeşitleri sergiler. Amorf polimerlerde görülen tipik deformasyon türü craze olup, bunlar genellikle yansıyan ışıkta çıplak gözle görülebilir ve çatlak benzeri bir görünümü oluşturur. PMMA ve PS yükleme altında çatlaklar sergileyen tipik birer amorf camsı polimer örnekleridir. Bu çatlakların ince yapısı elektron mikroskobunda yalnızca yüksek büyütmelerde görülebilir [28].

Yapılan bir çalışmada polistiren homopolimerinin moleküler ağırlığına ve karışım bileşimine bağlı olarak, çok çeşitli morfoloji ve mikromekanik davranışları ortaya çıkarmıştır. Sabit bir moleküler ağırlıkta (yaklaşık 100.000 g/mol) ve sabit bir bileşimde, diblok kopolimerlerde gözlemlenen tüm temel morfolojilerin zincir mimarisindeki bir değişiklik yoluyla üretilebileceği görülmüştür. Dolayısıyla işleme koşullarındaki değişiklikler, morfolojiyi ve mikromekanik davranışını önemli ölçüde değiştirmektedir. Özellikle homojen plastik akışından (mikro boyun oluşturma ve çekme), craze benzeri deformasyon bölgelerinin oluşumuna (deformasyonun lokalizasyonu) geçiş, polistiren katmanlarının kalınlığı kritik bir değeri aştığında ortaya çıkmaktadır. Gelecekteki çalışmalarda, blok kopolimer mimarisinin ve işleme koşullarının morfoloji oluşumu ve mikromekanik davranış üzerindeki etkisine odaklanmak gereklidir [29].

3. AMORF POLİMERLER

Amorf polimerler, X-ışını veya elektron saçılma deneylerinde kristal yapı sergilemeyen polimerler olarak tanımlanır. Termoplastikler, reçineler (polyesterler ve epoksiler gibi) ve elastomerler (kauçuk) amorf polimerler ailesine aittir [28]. Amorf polimerler, moleküler zincirleri rastgele birbiri içine geçmiş yün yumakları şeklindedir. Moleküller kendi aralarında rastgele bağlanmış durumda olup, kristalleşme veya çapraz bağlar mevcut değildir. Amorf yapıdaki plastikler, çekme zorlamaları etkisi altındayken molekül zincirleri çekme yönünde bir yönlenme gösterir ki bu nedenle, çekme mukavemetleri yüksektir [18]. Polimerler tamamen amorf olabilecekleri gibi hem amorf hem de kristalin bölgelere de sahip olabilirler. Amorf polimerler, yapıları ve sıcaklıkları nedeniyle farklı mekanik ve fiziksel özelliklere sahip olabilir. Tg'nin altında, amorf polimerler camsı, sert ve kırılgan özellik gösterirler iken, sıcaklık arttıkça, amorf polimerler çapraz bağlar oluşturur, yumuşar ve elastik özellik gösterirler (poliizobütilen, polibütadien gibi). Polimerin Tg üzerine ısıtılması devam ederse; polimer, kauçuğumsu davranışı bırakıp, yeterince yüksek sıcaklıklarda sıvı halini alır. Doğal kauçuk (lateks) ve stiren-bütadien kauçuğu (SBR) Tg'nin altındaki amorf polimerlere iyi birer örnektirler [5,18]. Polimer zinciri üzerindeki grupların, örneğin metil gruplarının, rastgele yer aldığı yapı ataktik yapı olarak adlandırılır. Amorf polimerler ataktik polimer zincirlerinden oluştukları için yapıları zayıftır. Şekil 4'te ataktik zincir yapısının temsili gösterimi mevcuttur [30].

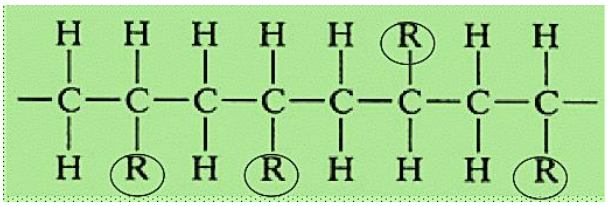

Şekil 4. Ataktik zincir yapısının gösterimi [24]

Polimerizasyon ve üretim prosesinden etkilenen kristalinite derecesi amorf polimerlerde bulunmadığı için bunlar, kristalin polimerlere kıyasla daha düşük bir yoğunluğa sahiptirler ve bu nedenle, kimyasal dirençleri düşük olup, yapıları da şeffaftır [31]. Amorf polimerler genellikle anizotropik özelliklere sahiptir, çünkü zincirlerinin düzenlenmesinde belirli bir yön yoktur ki bu da aşağıdaki durumlara sebep olur;

- **Hatalı erime sıcaklığı:** Erime, molekül içi bağların kırılmasından ziyade viskozitedeki azalmaya bağlı olduğundan, erime, geniş bir sıcaklık aralığında gerçekleşir.
- **Yanlış katılaşma sıcaklığı:** Katılaşma da yine geniş bir sıcaklık aralığında gerçekleşir. Sıcaklık yükseldiğinde bu polimerler elastik özellik gösterir.
- **Yüksek kırılma indeksi:** Camların kırılma indeksi yüksektir, bu sebeple şeffaftırlar [1].

Amorf polimerler, görünüşte rastgele ve sarmal bir moleküler yapıya sahip olan ve ısıtıldığında hemen erimeyen bir polimer türü olup, bunların işlenmesi daha kolaydır. Ek olarak, amorf polimerler daha iyi boyutsal kararlılık sunar ve akışta izotropiktir, daha az büzülme sağlamak için daha eşit şekilde erir. Amorf polimerler, camsı, kırılgan polimerler (PS, PMMA, döngüsel olefin kopolimeri (COC), stiren akrilonitril (SAN) gibi) ve sünek polimerler (PC ve PVC gibi) dahil olmak üzere geniş bir malzeme grubunu oluşturur. Amorf blok kopolimerler ve polimer karışımları da amorf polimerlerdir [28].

3.1 Polimetakrilat (PMMA)

PMMA, işlenmesi kolay ve film, çubuk, tüp ve levha gibi birçok yarı mamul ürüne dönüştürülebilen, oldukça şeffaf, amorf, sentetik, ticari olarak kolayca temin edilebilen termoplastiklerden birisidir. Yüksek Tg'ye (398 °K), iyi mekanik özelliklere ve mükemmel hava koşullarına dayanıklılığa sahip ve yüksek hacimli amorf bir termoplastiktir. Bunun yanında, oldukça kırılgan bir yapıda olan PMMA, düşük darbe dayanımına ve yorulma direncine sahiptir. Dayanıklılığını artırmak için PMMA genellikle çekirdek-kabuk yapısında kauçuk veya diğer darbe düzenleyiciler ile modifiye edilebilir [31].

Su absorpsiyonu düşük olduğu için uzun süre neme maruz kalması ya da tamamen suya daldırılması ile mekanik ve optik özelliklerinde önemli bir değişiklik görülmez. Hava ve güneş ışığına dayanıklılığı sebebiyle UV stabilizatörü olarak da kullanılır. PMMA'nın IUPAC adı, poli (metil 2-metilpropenoat) olup [32], Tablo 1'de bazı fiziksel özellikleri verilmiştir.

Tablo 1. PMMA'nın bazı fiziksel özellikleri [32]

Özellik	Ortalama Değer
Çekme Dayanımı (MN/m^2)	55-80
Kopma Uzaması	<%10
Bükülme Dayanımı (MN/m^2)	100-150
Özgül Isısı (kJ/kg/°C)	1,25-1,7
Isıl Genleşme Katsayısı $(°C)^{-1}$	$5\text{-}10\times10^{-3}$
Özkütlesi	1,0-1,2
Su Absorpsiyonu	%0,1-0,5

İmplant olarak diş hekimliğinde ve sanatsal ve estetik olarak da farklı şekillerde kullanım alanlarına sahiptir [32]. PMMA veya polikarbonat gibi yalnızca amorf yapıya sahip olan termoplastikler saydamlığın önemli olduğu uygulamalarda özellikle tercih edilirler. Amorf termoplastikler genellikle kimyasallara karşı düşük direnç göstererek kimyasal ortamlardaki çevresel faktörler sebebiyle çatlamaya başlayabilirler. Yarı-kristal termoplastikler ise çözücülere ve diğer kimyasallara karşı daha dirençli olup; kristalleri ışığın dalga boyundan büyük olması sebebiyle opaktırlar ve bu sebeple optik uygulamalarda tercih edilmezler [33]. PMMA, metil metakrilatın organik peroksitler kullanılarak polimerizasyonu ile üretilir. Bu amaçla üç farklı üretim süreci kullanılır ki bunlar; süspansiyon polimerizasyonu (organik peroksitlerle), toplu (yığın) polimerizasyon (organik peroksitlerle) ve emülsiyon polimerizasyonudur [34].

3.2 Kauçuk

3.2.1 Doğal kauçuk

Kauçuğun amorf bir polimer olması nedeniyle sarmal polimer zincirleri gerilerek düzleştirilebilir. Gerilmiş yapıdaki daha yüksek sıralı zincirler entropik olarak kararsızdır ve gevşemelerine izin verildiğinde orijinal sarmal durumlarına geri dönerler (Şekil 5).

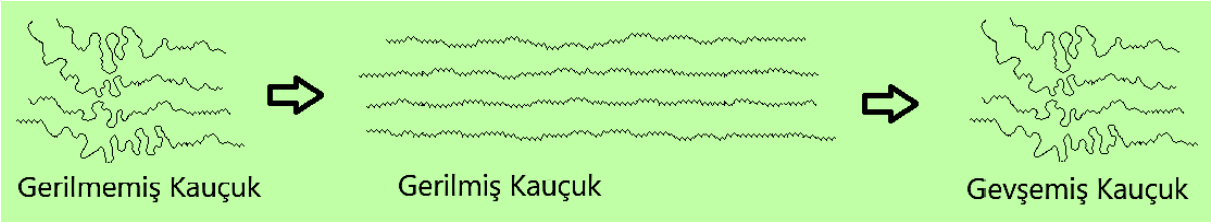

Şekil 5. Gerilmemiş ve gerilmiş kauçuktaki uzun zincirli moleküller [35]

Charles Goodyear tesadüf eseri kükürt ve kauçuğun karıştırılmasıyla kauçuk özelliklerinin daha sert, soğuk-sıcağa dayanıklı ve elastikiyetinin daha da arttığını keşfetmişti ve bu durum vulkanizasyon olarak adlandırıldı. Kükürt vulkanizasyonu, kauçuğu veya ilgili polimerleri kükürt veya eşdeğer iyileştiricilerle ısıtarak daha dayanıklı malzemelere dönüştüren ve kauçuk zincirleri arasında çapraz bağlar oluşturan kimyasal bir işlemdir. Bu işlem, doğal kauçuğun elastik özelliklerini geliştirir. Vulkanize edilmemiş kauçuğa (ham kauçuk) bir kuvvet uygulandığında gerilir ve ardından kuvvet ortadan kaldırılırsa, kauçuk tamamen orijinal boyutlarına geri dönemez. Yani, vulkanize edilmemiş kauçuk, basitçe plastik gibi davranır. Ancak vulkanize kauçuk, bir kuvvet uygulandığında esneyecek ve kuvvet kaldırıldığında orijinal durumuna (veya orijinal durumuna çok yakın bir hale) geri dönecektir. Bunun nedeni vulkanize kauçukta bulunan çapraz bağlardır. Çapraz bağlamanın %2-3 civarında gerçekleşmesi, ısıtma ve soğutma sırasında gözlenen artık yapışkanlık ve kırılganlık sorunları yaşamayan kullanışlı yumuşak bir kauçuk yapısı elde edilirken, %25-35 çapraz bağlanmada sert bir kauçuk ürün oluşur [36]. Şekil 6, vulkanizasyon işlemiyle kükürtle çapraz bağlanmış amorf kauçuğun temsili kesitini göstermektedir.

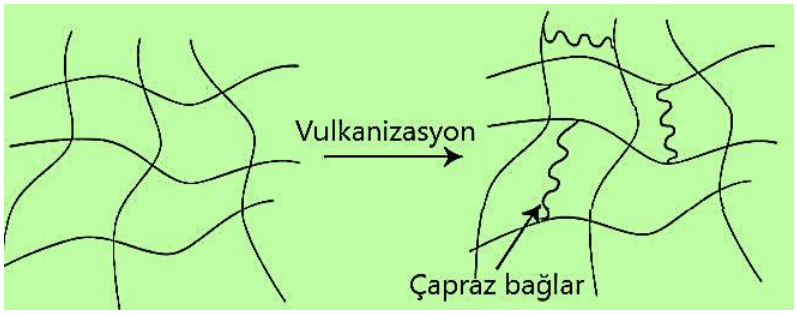

Şekil 6. Vulkanizasyon işlemiyle kükürtle çapraz bağlanmış amorf kauçuğun temsili kesiti [35]

Doğal kauçuğa gerilim uygulandığında, kauçuk molekülleri kuvvetin yönü boyunca düzenlenir ki bu nedenle, kauçuğun bazı bölgeleri kristalleşir ve bu duruma "gerilim kaynaklı kristalleşme" denir. Doğal kauçuk, dolgu maddesi olmadan bile yüksek çekme özellikleri gösterir [37].

3.2.2 Polibütadien kauçuk (PBR)

Polibütadien, aşınmaya karşı direnci yüksek olan ve lastik imalatında kullanılan sentetik bir kauçuktur. Yüksek elektrik direnci sayesinde elektronik kaplamalarda da kullanılabilir. Polibütadien, 1,3-bütadien monomerinin polimerizasyonundan oluşan bir polimerdir. 1,3-Bütadien, basit bir konjuge dien hidrokarbon olan organik bir bileşiktir (dienlerin iki karbon-karbon çift bağı vardır). Polimer zincirinin bağlanabilirliği açısından, bütadien cis-, trans- ve vinil olarak adlandırılan üç farklı şekilde polimerleşebilir. Cis- ve trans- formları, bütadien moleküllerinin uçtan uca bağlanmasıyla ortaya çıkar ve söz konusu polibütadien izomerik formlarının özellikleri birbirlerinden farklıdır. Örneğin, "yüksek cis-" polibütadien yüksek bir esnekliğe sahiptir. Polibütadienler dallanma ve moleküler ağırlıkları açısından da farklılıklar gösterir. Polimerizasyon sırasında oluşan trans- çift bağlar (Şekil 7), polimer zincirinin oldukça düz kalmasına izin vererek, polimer zincirlerinin bölümlerinin malzemede mikro kristalli bölgeler oluşturmak üzere hizalanmasını kolaylaştırırken; cis- çift bağları ise polimer zincirinde bükülmeye neden olarak, onların kristalin bölgeler oluşturmak için hizalanmasını önler ki bu durum da daha büyük amorf polimer bölgelerinin oluşumuyla sonuçlanır [38].

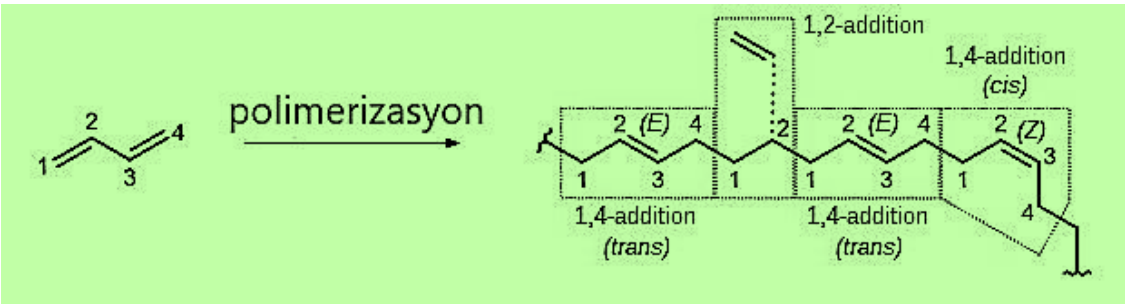

Şekil 7. 1,3-Bütadienin polimerizasyonu [38]

3.2.3 Etilen-propilen-dien monomer (EPDM)

Diğer kristalleşmeyen polimerik malzemeler gibi, dolgusuz EPDM kauçuklarının mekanik özellikleri de çok zayıftır ve dolayısıyla takviye dolgu maddelerinin eklenmesi kauçuğa mukavemet kazandırmak için önemlidir. EPDM kauçuklarının uygulama alanları genellikle kimyasal ve asidik ortamları ya da su ve gaz sistemleri olduğundan, yüksek değerlere sahip fiziksel özellikler gerekli değildir. EPDM bileşiklerinde genelde kolay işlenebilen yarı takviye edici karbon siyahı kullanılır. EPDM kauçukları, galvanik kaplama endüstrisi gibi uygulamalarda nitrik asit ve kromik asit aşındırıcı ortamları işleyen proses endüstrileri için önemlidir. Piyasada yağ ile genişletilmiş başka EPDM çeşitleri de mevcuttur ki bunlar, darbe aşınmasının baskın olduğu alanlarda düşük sertlikteki bileşikler için kullanılabilir. EPDM, yüksek yırtılma direncine sahip olduğu için "çatlaksız kauçuk" olarak da anılır. EPDM kauçukları için genel bir kürleme sistemi, bir tiuram ve/veya bir ditiokarbamat içeren bir tiyazol (merkaptobenzotiyazol veya MBTS) hızlandırıcıdan oluşur. EPDM molekülünün ana zincirlerinde çift bağ yoktur ve bu nedenle EPDM, güneş ışığına veya yüksek ozon konsantrasyonuna uzun süre maruz kaldıktan sonra bile moleküler bölünme nedeniyle bozulmaz ve dolayısı ile ozon, ısı direnci, ultraviyole radyasyon ve nem gibi diğer atmosferik şartlara maruz kalma dirençleri mükemmeldir. Moleküler yapısından dolayı ve uygun şekilde birleştirilirse, EPDM bileşikleri her türlü hava koşullarına karşı dayanıklıdır. Mükemmel elektriksel yalıtım özellikleri ve yüksek dielektrik dayanımı nedeniyle EPDM, çelik endüstrisindeki galvanik kaplama tanklarında yaygın olarak tercih edilen bir kauçuk kaplama bileşiğidir [39].

EPDM yalnızca katalitik ekleme polimerizasyonu kullanılarak üretilir. Monomerlerin rastgele birleşmesi, EPDM'nin amorf, elastomerik karakterini açıklamaktadır. Klasik vanadyum bazlı Ziegler–Natta (ZN)

katalizörleri uzun yıllardır EPDM üretiminde kullanılmaktadır. Mükemmel elastomerik özelliklere sahip, homojen, tamamen amorf EPDM'ler üretilebilmektedir. EPDM'in yüksek uzun zincir dallanmasına sahip olması, hızlı karıştırma ve yüksek ekstrüzyon oranlarına olanak tanıyarak onu yoğun otomotiv profilleri, radyatör hortumları ve pencere contalarının üretiminde tercih edilen polimer haline getirmektedir. Yapılan bir çalışmada yüksek molekül ağırlıklı, amorf 5-vinil 2-norbornen-EPDM'ler, bina ve inşaat pencere contalarında karbon siyahı, beyaz dolgu maddesi, yağ ve peroksitten oluşan bir formülasyonda değerlendirilmiştir [40].

3.2.4 Akrilonitril-bütadien kauçuk (NBR)

Akrilonitril bütadien kauçuk (NBR), akrilonitril ve bütadien monomerlerinin bir kopolimeridir. Fonksiyonel bir gruba (C≡N) sahip akrilonitril nedeniyle, NBR yüksek dielektrik sabitine sahip olan özel bir polar kauçuktur. NBR; geniş bir sıcaklık uygulama aralığı, bağlanma performansı, mükemmel yağ ve solvent (çözücü) direnci ve nispeten düşük maliyet gibi faydalı özelliklere sahip olduğu için endüstriyel ve otomotiv kauçuk ürünlerinde yaygın olarak kullanılır. Bununla birlikte, rastgele kopolimerlerin düzensiz moleküler yapısından dolayı gerinim kaynaklı kristalleşme yapmadığından, NBR kendi kendini güçlendirme davranışları sergilemez ki bu da nispeten zayıf mekanik özelliklere sahip olması ile sonuçlanır. Bu nedenle, iyi mekanik özelliklere sahip yüksek performanslı ürünler elde etmek üzere NBR için uygun bir dolgu maddesi seçilmelidir [41].

3.3 Akrilonitril-Bütadien Stiren (ABS)

Akrilonitril Bütadien Stiren plastik opak bir termoplastik olup, ABS, en yaygın olarak emülsifikasyon işlemiyle veya tipik olarak tek bir üründe bir araya gelmeyen birden fazla ürün birleştirilerek polimerize edilir [42,43]. Akrilonitril-bütadien-stiren kopolimeri, akrilonitril, bütadien ve stirenden oluşan üç monomerden oluşur ve amorf plastiklere aittir. ABS, iyi darbe dayanımına, boyutsal kararlılığa ve doğruluğa sahiptir. Bu amorf plastik, iyi bir ısı ve kimyasal direncine de sahiptir ve işlenmesi kolaydır. Galvanizlenmesi, boyanması ve basılması kolaydır [44]. ABS, darbelere dayanıklı amorf bir mühendislik termoplastiğidir. Akrilonitril, sentetik bir monomer olup, propilen ve amonyaktan üretilir. Bu bileşen, ABS'nin kimyasal direncine ve ısıl stabilitesine katkıda bulunur. Bütadien, buhar kırıcılardan etilen üretiminin bir yan ürünü olarak elde edilir. Bu bileşen, ABS'ye tokluk ve darbe dayanımı özelliklerini sağlar. Stiren, etil benzenin dehidrojenasyonu ile üretilir ve ABS plastiğine işlenebilirlik ve sertlik özelliklerini sağlar. ABS, emülsiyon veya sürekli kütle tekniği ile üretilir. ABS'nin kimyasal formülü $(C_8H_8 \cdot C_4H_6 \cdot C_3H_3N)_n$'dir. Doğal olarak opak fildişi rengindeki bu malzeme, pigmentler veya boyalarla kolayca renklendirilebilir [45].

3.4 PVC

PVC, moleküler yapısındaki polar klor atomları ile doğrudan ilişkili olan amorf bir yapıya sahiptir. PVC, moleküler yapı veya mekanik özelliklerinde çok az değişiklik gösteren ve kimyasal olarak kararlı bir malzemedir. Bununla birlikte, uzun zincirli polimerler viskoelastik malzemeler olduklarından, uygulanan kuvvet akma noktalarının çok altında olsa bile sürekli dış kuvvet uygulamasıyla deforme olabilirler ki buna sürünme deformasyonu denir. PVC'nin sürünme deformasyonu normal sıcaklıkta sınırlı moleküler hareketi nedeniyle diğer plastiklere kıyasla düşüktür. PE ve PP'nin amorf bölümlerinde daha fazla moleküler hareketlilik vardır. PVC faz geçişi olmayan amorf bir plastik olduğu için, yani soğuma sırasında belirgin şekilde büzülmediğinden, kalıplarda üretilen PVC ürünler, kalıplanmış boyutlarını korurlar. PVC; bükme imalatında, kaynakta, yüksek frekanslı birleştirmede ve vakumla şekillendirmede ikincil işlenebilirlik özelliğine sahiptir. Slush kalıplama, serigrafi ve kaplama gibi macun reçine işleme yalnızca PVC ile mümkün olan işleme teknikleridir. Bu işleme yöntemleri döşeme, duvar kaplama ve astarlamada kullanılır [46].

Bir çalışmada PVC'nin %15 civarında kristalin bölgeye sahip olduğu görülmüştür. PVC'nin kristalleşme davranışının, benzer yüzde kristalin bölgeye sahip PET ile karşılaştırıldığında, PVC'nin çok daha hızlı

kristalleşmesi açısından farklılık gösterdi görülmüştür. PVC, ortam sıcaklıklarında diklorlu hidrokarbonlarda çözünmemektedir [47].

PVC'deki kristalin bölgelerin varlığı, polimerin mukavemetine ve esnekliğine önemli ölçüde katkıda bulunur. PVC'de bir trombosit veya düz iğne benzeri katmanlı kristalit (birincil) ve eriyiklerden veya çözeltilerden elde edilen saçaklı misel kristalit (ikincil) olmak üzere iki farklı kristalit yapısı tanımlanmaktadır. Her iki kristalit de gevşek ve çapraz bağlar oluşturmaktadır. Kristalitler reolojik özellikler üzerinde önemli bir etkiye sahiptir. Erime fazındaki birincil kristalit ağlar, elastik modülde bir azalmaya neden olmaktadır. Birincil kristalitler çok geniş bir sıcaklık aralığında (120-260 °C) erimektedir. Polimer soğudukça, dayanıklılık ve esneklik sağlayan fiziksel çapraz bağlar olan ikincil kristalitler oluşur [48, 49].

3.4.1 Polistiren

Polistiren (PS), işlenmesi kolay ve köpükler, filmler ve levhalar gibi çok sayıda yarı mamul ürüne kolaylıkla dönüştürülebilen berrak, amorf ve polar olmayan bir termoplastiktir [50]. $(C_8H_9)_n$ formülüne sahip olan PS, uzun bir hidrokarbon zincirinin üzerinde her iki karbondan birine fenil grubunun bağlanmasıyla oluşur. Vinil bazlı bir monomerden sentezlendiği için polimerizasyonu da serbest radikal vinil polimerizasyonu ile gerçekleşir. Sonuçta oluşturulan polimer, izotaktik polistiren (iPS) olsa da endüstride iPS üretimine pek rastlanmaz çünkü iPS sentezi, izotaktik polipropilen ya da polietilen sentezinden daha maliyetlidir. Normal PS diye adlandırılan ataktik PS'nin üretimi daha yaygındır. Bu polimer, ataktik yapının getirdiği düzensizlikten dolayı amorftur ve bu sebeple bir erime noktası yoktur. Yüksek sıcaklıklarda, düşük molekül ağırlıklı bileşiklerden oluşan bir karışıma (çoğunlukla stiren) dönüşerek bozunmaya uğrar. Metalosen-katalizörlü polimerizasyon yöntemiyle sindiotaktik PS de üretilebilir. Kristal yapı oluşturabilen bu PS'nin erime noktası 270 °C civarındadır [33].

3.5 Polikarbonat

Polikarbonat (PC) plastikler; doğal olarak, şeffaf ve şekilsiz bir termoplastik olup, çeşitli renklerde (belki yarı saydam ve belki de değil) ticari olarak temin edilebilmelerine rağmen, hammaddesi, ışığın neredeyse camla aynı kapasitede dahili olarak iletilmesine izin verir. PC polimerler, çeşitli malzemeler üretmek için kullanılır ve darbe direnci ve/veya şeffaf bir ürün gerekliliği olduğunda (örn., kurşun geçirmez cam üretiminde) özellikle yararlıdır. PC genellikle gözlüklerde, tıbbi cihazlarda, otomotiv bileşenlerinde, koruyucu donanımda, seralarda, dijital disklerde (CD'ler, DVD'ler ve Blu-ray) ve dış aydınlatma armatürlerinde plastik lensler için kullanılır. PC ayrıca, çok iyi ısı direncine sahiptir ve önemli ölçüde malzeme bozulması olmadan alev geciktirici malzemelerle birleştirilebilir. Şekil 8, ABS, Polistiren (PS) veya Naylon gibi yaygın olarak kullanılan diğer plastiklerin darbe dayanımı ile karşılaştırıldığında PC'nin nispi darbe dayanımını göstermektedir [51].

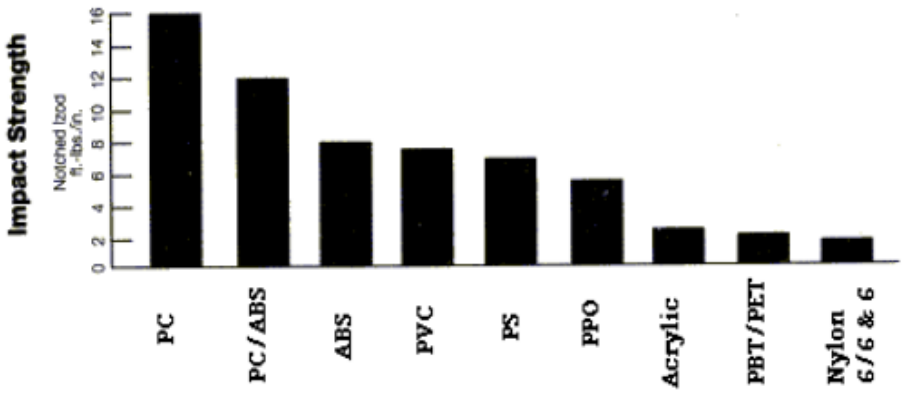

Şekil 8. Çeşitli polimerlerin darbe dayanımları [51]

PC'nin bir diğer özelliği de çok esnek olmasıdır. Oda sıcaklığında çatlama veya kırılma olmaksızın oluşturulabilir. Şeffaflık gerektiren, iyi elektrik yalıtımı özelliklerine sahip bir malzeme gerektiğinde kullanılabilir. Tipik olarak amorf plastikler, kristal polimerlerde olduğu gibi katıdan sıvıya keskin bir geçiş sergilemek yerine kademeli olarak yumuşama eğilimi gösterirler (yani cam geçiş sıcaklıkları ile erime noktaları arasında daha geniş bir aralığa sahiptirler) [51].

3.6 PET

Polietilen tereftalat (PET), sıvıların, yiyecek ve içeceklerin saklanmasında ile taşınmasında ve sentetik liflerin yapımında kullanılan termoplastik polimer bir reçine olup, amorf veya yarı kristalin yapıda olabilir. PET'in kristal yapısı ile fiziksel ve mekanik özellikleri, büyük oranda, işlem sıcaklığı, soğutma hızı, gerdirme işlemi gibi proses parametrelerine bağlıdır. Tüm polimerlerde olduğu gibi kristalizasyon, PET'in fiziksel ve mekanik özelliklerini etkileyen önemli bir özelliktir. Tipik yarı kristalin polimerler gibi PET molekülleri de kristalin ve amorf bölgelerden oluşan karmaşık yapıya sahiptirler (Şekil 9).

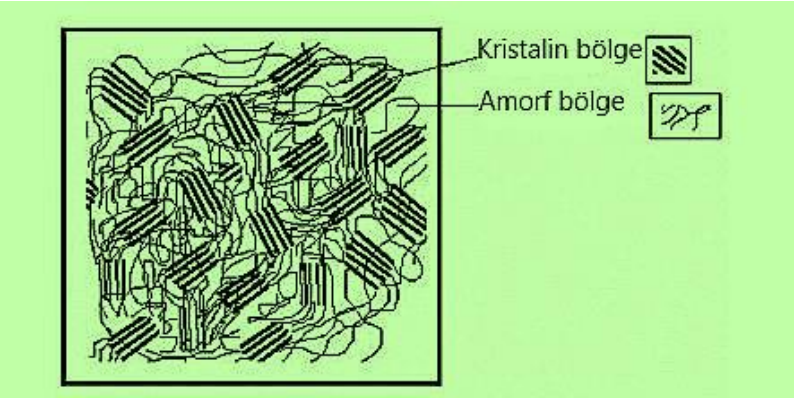

Şekil 9. Amorf-kristalin makromoleküler polimer yapısı [52]

PET, kimyasal ve geometrik yapısındaki düzenlilik nedeniyle kristalleşebilen bir polimer olup, bariyer özellikleri ve mekanik mukavemetindeki sınırlamalara rağmen, kristal PET hala yaygın olarak kullanılmaktadır. Yüksek kristalliğe sahip polimerler daha yüksek bir Tg'ye sahiptir (Tg; amorf PET için 67 °C ve kristalin PET için 81 °C'dir) ve daha yüksek modül ile tokluk, sertlik, gerilme mukavemeti ve solventlere (çözücülere) karşı daha fazla dirence sahiptir. Kristalizasyon işlemi, çekirdeklenme ve küresel kristalleşmeden oluşur ve Tg'nin üzerindeki ve Tm'nin altındaki sıcaklıklarda meydana gelebilir. Eriyiğin hızlı bir şekilde soğutulması tamamen amorf bir PET ile sonuçlanır. Kristalin polimerler, moleküllerinin arasına serpiştirilmiş amorf bölgeler nedeniyle heterojen bir yapıya sahipken, amorf polimerler tüm formlarında (eriyikler, kauçuklar, camlar vb.) homojen bir yapıya sahiptir. Yarı kristalin bir polimerin Tg'si, amorf polimerinkinden daha yüksek ve daha geniştir. Kristalin polimerler belli bir Tm değeri ile karakterize edilirken amorf polimerler ise bir Tg değeri ile karakterize edilir [52].

Yapılan bir çalışmada geri dönüştürülmüş polietilen tereftalat (PET) polimerinin performansı üzerinde kristalin, hareketli amorf ve sert amorf fraksiyonların rolü incelenmiştir. PET polimerlerin kristalin bölgeleri, moleküler zincirlerin düzenli bir şekilde sıralandığı bölgelerdir. Bu bölgeler, polimerin mekanik mukavemetini ve sertliğini etkileyebilir. PET polimerlerin mobil amorf bölgeleri, moleküler zincirlerin daha rastgele bir şekilde düzenlendiği, ancak hala hareket edebilen bölgelerdir. Bu bölgeler polimerin esnekliğini ve sünekliğini etkileyebilir. PET polimerlerin rijit amorf bölgeleri, moleküler zincirlerin daha düzensiz ve sabit bir şekilde düzenlendiği bölgelerdir. Bu bölgeler polimerin termal davranışını ve kimyasal dayanıklılığını etkileyebilmektedir [53].

4. YARI KRİSTALİN POLİMERLER

Kristalin polimerler, iyi düzenlenmiş bir yapıya sahip olan polimerlerdir [30]. Tüm kristalli polimerler önemli miktarda amorf kısım içerir. Bu nedenle, kristalli polimerler genellikle yarı kristalin polimerler olarak adlandırılır. Kristal polimerlerin çoğu amorf bölgelere sahiptir, yani hiçbir zaman tamamen kristalin değillerdir. Kristallik, %0 (tamamen şekilsiz) ile %100 (tamamen kristal) arasında değişebilir, ancak çoğu polimer bu uç noktalar arasında bir yere düşer. Zincir esnekliği (hem tüm zincir boyunca hem de atomlar arasındaki bağlarda gözlenen esneme) polimer kristalinin oluşumunda büyük rol oynar. Zincirler birbirlerine karşı esneyip büzüldükçe, çeşitli çekme ve itme kuvvetleri, polimer zincirlerinin kendilerini nasıl daha düzenli veya daha az düzenli bir hale geleceklerini etkiler. Kristallik derecesi, bir polimerin tipik bir katı gibi eriyip erimediği veya camsı ve kauçuğumsu haller arasında geçiş yapıp yapmadığı ile doğrudan ilişkilidir. Yüksek oranda kristalin polimerler bir erime noktasına sahip olduklarından ısıtıldıklarında, uzun zincirli yapılarının düzenli, düzenlemesinin rastgele veya düzensiz bir düzenlemeye geçtiği belirli bir sıcaklığa (Tm) ulaşırlar [4]. Polietilen, polipropilen, PVC ve naylon gibi yukarıda bahsedilen polimerlerin amorf bölgeleri olduğu gibi kristalin bölgeleri de mevcuttur. Dolayısıyla bu polimerler, farklı kristalin-amorf oranlarına sahip olabilirler ve bu nedenle farklı mekanik ve termal özelliklere sahip olabilirler.

5. AMORF VE YARI KRİSTALİN POLİMERLERİN KIYASLAMASI

- Amorf polimerler, moleküler zincirleri uzayda düzensiz bir şekilde düzenlenmiş katılar olup, kristalin polimerler ise bazı bölümlerinin kesin bir sırayla kristalleştiği ve organize bir katı birimin oluşmasına izin verdiği polimerlerdir.
- Amorf polimerler ataktik polimer zincirlerinden oluşurken, kristalin polimerler sindiyotaktik veya izotaktik polimer zincirlerinden oluşurlar.
- Amorf polimerler, moleküllerin rastgele düzenlendiği bölgeler içerirken, kristalin polimerler, moleküllerin kısmi bir düzende düzenlendiği bölgelere sahip olan polimerlerdir [5].
- Çekim kuvveti açısından bakıldığında amorf polimerlerin zincirleri arasındaki çekim kuvvetleri zayıf iken; kristalin polimerler, zincirleri arasında güçlü kuvvetlere sahiptir.
- Amorf polimerler düşük bir yoğunluğa sahipken, kristalin polimerler yüksek yoğunluğa sahiptir.
- Amorf polimerler yumuşak, kristalin polimerler serttir.
- Amorf polimerler yüksek gaz geçirgenliğine sahipken, kristalin polimerler düşük gaz geçirgenliğine sahiptir.
- Amorf polimerlerin aksine, kristalin polimerler hem Tm hem de Tg değerine sahiptirler [5].
- Amorf polimerlerin kimyasal dayanımı düşük iken, kristalin polimerler yüksek bir kimyasal dirence sahiptir.
- Amorf polimerler şeffaf, kristalin polimerler opak veya yarı saydamdır.
- Amorf polimerler düşük bir kristallik derecesine, kristalin polimerler ise yüksek bir kristallik derecesine sahiptir ve bir polimerin fiziksel ve kimyasal özellikleri de buna bağlıdır [30].
- Amorf polimerlerde büzülme düşük iken, yarı kristalin polimerlerde büzülme çok yüksektir [5].
- Kimyasal temas veya yüksek düzeyde mekanik etkiye maruz kalan bir ortamda yarı kristalin yapıdaki polimerler daha iyi bir mekanik performans sağlar [28].
- Yarı kristalin polimerler, aşınmaya karşı üstün performans sağlar [28], ki bu durum Tablo 2'de kıyaslamalı olarak verilmiştir.

Tablo 2. Amorf ve yarı kristalin polimerlerin kıyaslaması [1,3]

Amorf Polimerler	**Yarı Kristalin Polimerler**
Rastgele Dağılım (Düzensiz)	Düzenli Dağılım
Geniş Proses Sıcaklığı	Dar Proses Sıcaklığı
Ataktik Polimer Zincirleri	Sindiyotaktik ve İzotaktik Polimer Zincirleri
Düşük Yoğunluklu	Yüksek Yoğunluklu
Zayıf Çekim Kuvveti	Güçlü Çekim Kuvveti
Düşük Hacimsel Çekme	Yüksek Hacimsel Çekme
Düşük Mekanik/Kimyasal Dayanım	Yüksek Mekanik/Kimyasal Dayanım
Transparan Yapı	Opak/Yarı Saydam
Düşük Büzülme	Yüksek Büzülme
Yüksek Erime Noktası	Düşük Erime Noktası
Örnekler: ABS, PS, ASA	Örnekler: PP, PA, POM, PBT

6. SONUÇ

Sonuç olarak, amorf ve yarı kristalin polimerler onları farklı uygulamalar için daha uygun kılan farklı özelliklere sahiptir. Amorf polimerler genellikle daha esnek, şeffaf ve darbelere karşı dirençliyken, kristalin polimerler daha sert, opak ve sıcaklığa karşı daha dayanıklıdır. Amorf ve yarı kristalin polimerler arasındaki farkları anlamak, geniş bir uygulama yelpazesi için belirli özelliklere sahip malzemelerin tasarlanmasında esas teşkil eder. Her iki polimer türünün de kendine göre avantajları ve dezavantajları vardır. Amorf polimerlerin yapısal eksiklikleri nedeniyle işlenmesi daha zor olabilir ve ayrıca, kristalin polimerlerden daha düşük Tm'ye sahip olabilirler. Farklılıklarına rağmen, amorf ve kristalin polimerler; ambalajlama, otomotiv, elektronik ve tıbbi cihazlar dahil olmak üzere birçok endüstride temel malzemeler olarak yaygın bir şekilde kullanılırlar.

REFERANSLAR

[1] Study Smarter. (2023, Nisan 13). Study Smarter. Web Sitesi: https://www.studysmarter.co.uk/explanations/chemistry/physical-chemistry/amorphous-polymer/

[2] Maddah, H. A. (2016). Polypropylene as a promising plastic: A review. Am. J. Polym. Sci, 6(1), 1-11.

[3] Brightworks Engineering. (2023, Nisan 13). Brightworks Engineering. Web Sitesi: https://brightworksengineering.com/upload/4/teknik-bulten-ocak-2017.pdf

[4] Mallard Creek Polymers. (2023, Nisan 13). Mallard Creek Polymers. Web Sitesi: https://www.mcpolymers.com/library/amorphous-vs-crystalline-polymers

[5] Pediaa. (2023, Nisan 13). Pediaa Web Sitesi: https://pediaa.com/difference-between-amorphous-and-crystalline-polymers/

[6] Goodship, V. (2007). Plastic recycling. Science progress, 90(4), 245-268.

[7] Tüm Plastik Sektörü Bu Çatı Altında. (2023, Nisan 13). Plastikçiyiz. Web Sitesi: https://www.plastikciyiz.biz/bilgi-kutuphanesi/teknik-bilgi-kutuphanesi/447/polimer-nedir-cesitleri-ozellikleri-nelerdir

[8] Yu, K., Taynton, P., Zhang, W., Dunn, M. L., & Qi, H. J. (2014). Reprocessing and recycling of thermosetting polymers based on bond exchange reactions. RSC advances, 4(20), 10108-10117.

[9] Hale, A., Macosko, C. W., & Bair, H. E. (1991). Glass transition temperature as a function of conversion in thermosetting polymers. Macromolecules, 24(9), 2610-2621.

[10] Takeoka, Y., Liu, S., & Asai, F. (2020). Improvement of mechanical properties of elastic materials by chemical methods. Science and Technology of Advanced Materials, 21(1), 817-832.

[11] Wang, Z., Lu, X., Sun, S., Yu, C., & Xia, H. (2019). Preparation, characterization and properties of intrinsic self-healing elastomers. Journal of Materials Chemistry B, 7(32), 4876-4926.

[12] Farfan-Cabrera, L. I. (2019). Tribology of electric vehicles: A review of critical components, current state and future improvement trends. Tribology International, 138, 473-486.

[13] Freemantle, M. (1987). Natural Products and Polymers. In Chemistry in Action (pp. 801-851). Palgrave, London.

[14] Allcock, H. R. (1994). Inorganic—organic polymers. Advanced Materials, 6(2), 106-115.

[15] Jones, R. G., Kitayama, T., Hellwich, K. H., Hess, M., Jenkins, A. D., Kahovec, J., ... & Wilks, E. S. (2016). Source-based nomenclature for single-strand homopolymers and copolymers (IUPAC Recommendations 2016). Pure and Applied Chemistry, 88(10-11), 1073-1100.

[16] Alshehrei, F. (2017). Biodegradation of synthetic and natural plastic by microorganisms. Journal of Applied & Environmental Microbiology, 5(1), 8-19.

[17] Wang, M., Guo, L., & Sun, H. (2019). Manufacture of biomaterials. Reference Module in Biomedical Sciences: Encyclopedia of Biomedical Engineering.

[18] Polymer Bilim ve Teknoloji. (2023, Nisan 13). Web Sitesi: http://blog.kmu.edu.tr/bbcarbas/wp-content/uploads/sites/70/2018/02/1.-ve-2.-%C3%BCnite.pdf

[19] Kocaokutgen Hasan. "Polimerlerin Özellikleri." (2023, Nisan 14). https://avys.omu.edu.tr/storage/app/public/hkocaok/109062/5%20Polimerlerin%20%C3%96zellikleri.doc

[20] Demirel, B., Yaraş, A., & Elcicek, H. (2011). Crystallization behavior of PET materials.

[21] Keith, H. D., & Padden Jr, F. J. (1964). Spherulitic crystallization from the melt. II. Influence of fractionation and impurity segregation on the kinetics of crystallization. Journal of applied Physics, 35(4), 1286-1296.

[22] Wang, J., Kazemi, Y., Wang, S., Hamidinejad, M., Mahmud, M. B., Pötschke, P., & Park, C. B. (2020). Enhancing the electrical conductivity of PP/CNT nanocomposites through crystal-induced volume exclusion effect with a slow cooling rate. Composites Part B: Engineering, 183, 107663.

[23] Parker, S. F., Maddams, W. F., Vickers, M. E., Williams, K. P., & Downs, G. W. (1996). Order in nascent polyethylene. Polymer, 37(13), 2755-2757.

[24] MEGEP. (2023, Nisan 13). Web Sitesi: http://megep.meb.gov.tr/mte_program_modul/moduller_pdf/Polimerlerin%20Fiziksel%20%C3%96zellikleri%202.pdf

[25] Coskun, A. "Erime ve Camsı Geçiş Sıcaklığı" (2023, Nisan 13). Web Sitesi: https://slideplayer.biz.tr/slide/7482713

[26] Arş. Gör. Dr. Yavuz Gökçe, "Yeni malzemeler Polimerler." (2023, Nisan 13). Web Sitesi: https://acikders.ankara.edu.tr/pluginfile.php/196152/mod_resource/content/0/KYM%20345%20Yeni%20Malzemeler-Polimerler.pdf.

[27] Doroudiani, S., Park, C. B., & Kortschot, M. T. (1996). Effect of the crystallinity and morphology on the microcellular foam structure of semicrystalline polymers. Polymer Engineering & Science, 36(21), 2645–2662. doi:10.1002/pen.10664

[28] Star Guide. (2023, Nisan 13). Star Guide Web Sitesi: https://www.starplastics.com/amorphous-vs-semi-crystalline-polymers

[29] Adhikari, R., & Michler, G. H. (2004). Influence of molecular architecture on morphology and micromechanical behavior of styrene/butadiene block copolymer systems. Progress in Polymer Science, 29(9), 949–986.

[30] "Polimerlerin Yapısı: Konformasyon-Konfigürasyon". Web Sitesi: https://acikders.ankara.edu.tr/pluginfile.php/98037/mod_resource/content/2/KYM%20445%20Polimerlerin%20Yap%C4%B1s%C4%B1%20%28Konfig%C3%BCrasyon%29%20-2018.pdf

[31] Polymer database. (2023, Nisan 13). Polymer Database Web Sitesi: https://polymerdatabase.com/polymer%20classes/Polymethacrylate%20type.html

[32] Zafar, Muhammad Sohail (2020). "Prosthodontic Applications of Polymethyl Methacrylate (PMMA): An Update." Polymers, 12(10), 1-35. https://doi.org/10.3390/polym12102299.

[33] Aldemir. (2023, Nisan 13). Aldemir Web Sitesi: https://www.aldemirltd.com/polymer/ adresinden alındı

[34] AKPA Kimya. (2023, Nisan 13). Akpa. Web Sitesi: https://www.akpakimya.com/uygulama-alani/pmma-polimetil-metakrilat/

[35] Learnbin. (2023, Nisan 13). Learnbin. Web Sitesi: https://learnbin.net/properties-of-natural-rubber/

[36] Vijayaram, T. R. (2009). A technical review on rubber. International Journal on Design and Manufacturing Technologies, 3(1), 25-37.

[37] Gregg Jr, E. C., & Macey, J. H. (1973). The relationship of properties of synthetic poly (isoprene) and natural rubber in the factory. The effect of non-rubber constituents of natural rubber. Rubber Chemistry and Technology, 46(1), 47-66.

[38] Wikipedia, the Free Encyclopedia. (2023, Nisan 13). Wikipedia Web Sitesi: https://en.wikipedia.org/wiki/Polybutadiene/

[39] Mokhothu, Thabang & Luyt, Adriaan & Messori, Massimo. (2014). Reinforcement of EPDM rubber with in situ generated silica particles in the presence of a coupling agent via a sol–gel route. Polymer Testing. 33. 97–106. 10.1016/j.polymertesting.2013.11.009.

[40] Van Doremaele, G., van Duin, M., Valla, M., & Berthoud, A. (2017). On the Development of Titanium κ1-Amidinate Complexes, Commercialized as Keltan ACE™ Technology, Enabling the Production of an Unprecedented Large Variety of EPDM Polymer Structures. Journal of Polymer Science Part A: Polymer Chemistry, 55(18), 2877-2891.

[41] Chueangchayaphan, W.; Luangchuang, P.; Chueangchayaphan. (2022). N. High Performance of Titanium Dioxide Reinforced Acrylonitrile Butadiene Rubber Composites. Polymers. 14(23). 1–12. https://doi.org/10.3390/polym14235267.

[42] Ataman Kimya, the Free Encyclopedia. (2023, Nisan 13). Ataman Kimya Web Sitesi: https://atamankimya.com/sayfalar.asp?LanguageID=2&cid=3&id=8&id2=4866 / adresinden alındı

[43] Adreco Plastics, the Free Encyclopedia. (2023, Nisan 13). Adreco Plastics Web Sitesi: https://adrecoplastics.co.uk/abs-plastic-properties/

[44] K.D. Feddersen. (2023, Nisan 13). K.D. Feddersen. Web Sitesi: https://kdfeddersen.com/competencies/engineering-plastics/polymers/abs//

[45] Campo, E. Alfredo (2008). Selection of Polymeric Materials || Polymeric Materials and Properties, 1–39. doi:10.1016/B978-081551551-7.50003-6.

[46] PVC. (2023, Nisan 13). PVC Web Sitesi: https://pvc.org/about-pvc/pvcs-physical-properties/

[47] Ballard, D. G. H., Burgess, A. N., Dekoninck, J. M., & Roberts, E. A. (1987). The ‘crystallinity’of PVC. Polymer, 28(1), 3-9.

[48] Marshall, R. A. (1994). Effect of crystallinity on PVC physical properties. Journal of Vinyl Technology, 16(1), 35-38.

[49] Polymer Database. (2023, Nisan 13). Polymer Database Web Sitesi: https://polymerdatabase.com/polymer%20classes/Polystyrene%20type.html / adresinden alındı

[50] McKeen, L. W. (2012). Styrenic Plastics. McKeen, L. W. (eds.) In Plastics Design Library, Permeability Properties of Plastics and Elastomers. 3rd ed. William Andrew Publishing.

[51] Creativemechanisms, (2023, Nisan 13). Creativemechanisms Web Sitesi: http://www.creativemechanisms.com/blog/everything-you-need-to-know-about-polycarbonate-pc /

[52] Demirel, Bilal & Yaraş, Ali & ELÇİÇEK, Huseyin. (2011). Crystallization Behavior of PET Materials. Balıkesir Üniversitesi Fen Bilimleri Enstitü Dergisi. 13. 26-35.

[53] Badia, J. D., Strömberg, E., Karlsson, S., & Ribes-Greus, A. (2012). The role of crystalline, mobile amorphous and rigid amorphous frac.

ALKU Journal of Science 2023, Sayı 5 (3): 149-162
e-ISSN: 2667-7814

Original Article

Experimental Verification of Dynamic Properties of a Hollow Aluminum Beam

Mert Bilir, Muhsin Karakaş, Akın Oktav*, Emre Özdemir, Ahmet Selim Savi, Fatih Sevinç, Hasan Ali Türkan
Alanya Alaaddin Keykubat University, Rafet Kayış Faculty of Engineering Department of Mechanical Engineering, Antalya, Turkiye.
**akin.oktav@alanya.edu.tr*

Abstract

In this study, analytical and computational analyses are performed to determine the dynamic properties of an aluminum hollow beam, and an experimental analysis is also performed. The experimental model is taken as a reference model and the computational model is updated accordingly using model updating tools. The damping behavior inherent in all physical structures is measured experimentally. According to the results of the cross-correlation modal assurance criterion, the experimental and computational results match well. The average error between the computational and experimental results for the first five damped natural frequency values is 1.5%.

Keywords: Hollow beam, Damping, Model update, Frequency response function.

Alüminyum Kutu Kesitli Kirişin Dinamik Özelliklerinin Deneysel Olarak Doğrulanması

Özet

Bu çalışmada, alüminyum boşluklu kirişin dinamik özelliklerini belirlemek için analitik ve hesaplamalı analizler gerçekleştirilmiş ve ayrıca deneysel bir analiz yapılmıştır. Deneysel model referans model olarak alınmış ve model güncelleme araçları kullanılarak hesaplamalı model buna göre güncellenmiştir. Tüm fiziksel yapılarda doğal olarak mevcut olan sönümleme davranışı deneysel olarak ölçülmüştür. Çapraz korelasyon modal güvence kriteri sonuçlarına göre, deneysel ve hesaplamalı sonuçlar iyi bir şekilde eşleşmektedir. İlk beş sönümlü doğal frekans değeri için hesaplamalı ve deneysel sonuçlar arasındaki ortalama hata 1,5% olarak hesaplanmıştır.

Anahtar Kelimeler: Kutu kesitli kiriş, Sönümleme, Model güncelleme, Frekans cevap fonksiyonu.

Geliş/Received: 10 Temmuz/July 2023
Kabul Ediliş/Accepted: 19 Ekim/October 2023

1. INTRODUCTION

Aluminum beams are used in many industries such as aerospace, automotive, defense, construction, and various industrial products. In the automotive industry, many load-bearing components of a body-in-white have properties similar to hollow beams [1, 2]. Automotive components are stimulated by internal and external influences that can cause fatigue, fracture, and damage. Dynamically induced vibrations can cause unwanted acoustic emissions [3]. Vibration analysis of an airplane wing is one of the critical problems during the design of the wing [4]. The vibration behavior of beams, which are components of various structures, is part of the dynamic characteristics of systems [5]. Hollow beams are also used in the defense industry. For example, tank barrels are composed of multiple hollow beams.

Hollow beams are often used in engineering structures because they are cheaper, lighter and easier to assemble. The main goals when creating new designs are to use lighter structures and increase strength. In addition to weight savings, material savings also provide a significant economic advantage. In a study, analytical and computational modal analysis procedures were applied on a hollow Euler-Bernoulli beam using Matlab and Ansys [6]. The researchers concluded that the error between the computational and analytical results decreases as the slenderness ratio of the hollow beam increases. They used the finite element method (FEM) to perform dynamic analysis on hollow cantilever beams of various diameters and compared their findings with analytical results. Another study reported a good agreement between Ansys Workbench results and theoretical results [7]. In the study, the researchers compared the natural frequencies of hollow and solid beams of circular cross-sections made of different materials using Ansys Workbench. They found that when the inner diameter of the circular beam is reduced, the transverse natural frequency values increase. The researchers also showed a way to determine the natural frequencies and mode shapes of a beam using a combined analytical and numerical method [8]. They concluded that it is better than the conventional finite element method considering the computational cost. In another research, an analytical modal analysis of aluminum and steel beams was performed.

The researchers performed a modal analysis of the cantilever beam using Euler-Bernoulli beam theory and calculated the natural frequencies and mode shapes using FEM [9]. The theoretical and experimental results were compared, and very close values were obtained [10]. In their study, the researchers obtained and compared the results of dynamic analysis of steel, aluminum, and fiberglass cantilever beams by performing analytical and experimental calculations using Ansys. By comparing the error rates, they concluded that the error is less at low frequencies than at high frequencies [11]. Researchers are trying to reduce the severity of vibrations that cause component wear and fatigue in vehicles. The severity of vibration problems increases when the mass of the vehicle is reduced. An aluminum cantilever beam was studied for the vibration reduction frame. Friction strips were used to reduce vibration, reduce the overall mass of the structure, and regulate the vibration amplitude [3]. In the study, the researchers presented the natural frequency variation of the beams to quantify the damage, the damaged area, and the magnitude of the damage [12]. As a result of the experiments and calculations, the damaged areas were accurately estimated.

In the relevant literature, it is observed that analytical and computational studies on hollow beams have been carried out, but studies on model updating and damping behaviors of the structures are limited. The model updating procedure is necessary not only for validation but also to complement the model in terms of damping properties. In this study, analytical and computational analyses are performed to determine the dynamic properties of an aluminum hollow beam, and an experimental analysis is also performed. The experimental model is taken as a reference model and the computational model is updated accordingly using the model update tools available in Siemens Simcenter3D v2022.2.

2. MATERIAL AND METHOD

The dynamic characterization study for the hollow aluminum beam is conducted using experimental and computational modal analysis procedures. The finite element model is a deterministic numerical solution model that facilitates the solution of complex problems in engineering fields [13]. The computational analysis is conducted using Simcenter 3D. In the work, a 750 mm × 20 mm × 10 mm hollow beam with a 2 mm wall thickness is used (Figure 1). The material is Aluminum 6063. The mechanical properties of the material are tabulated in Table 1. Four different methods were applied throughout the study. In Section 2.1, the first five undamped natural frequencies are calculated analytically using the Euler-Bernoulli beam equation. In Section 2.2, the structure is modeled in 2D and 3D using FEM, and the first five natural frequencies and associated mode shapes are calculated. In addition, these procedures are also performed using Matlab. Information about the experimental studies and results is given in Section 2.3. In Section 2.4, a model update analysis is performed based on the experimental results.

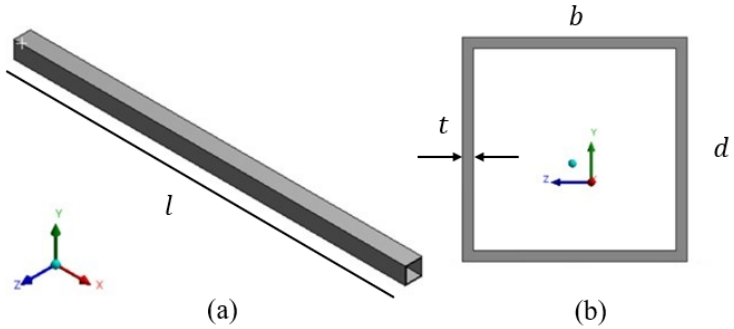

Figure 1. Dimensions of the cantilever beam (a) isometric view of the beam, (b) cross-section

Table 1. The dimensions and material properties of the Aluminum 6063 hollow beam

Parameter	Value
E: Young's modulus (GPa)	68.9
ν: Poisson's ratio	0.33
ρ: Density(kg/m³)	2,755.4
l: Length (mm)	750
b: Width (mm)	20
d: Height (mm)	10
t: Wall thickness (mm)	2

2.1 Analytical Calculations

The equation of motion for isotropic cantilever uniform Euler-Bernoulli beam exposed to free vibration is given as [14-16]:

$$c^2 \frac{\partial^4 w}{\partial x^4}(x,t) + \frac{\partial^2 w}{\partial t^2}(x,t) = 0 \quad (1)$$

where w is the transverse deflection, and c is

$$c = \sqrt{\frac{EI}{\rho A}} \tag{2}$$

where E is Young's modulus, I is the area moment of inertia, ω is the circular frequency A is the cross-sectional area. The initial lateral displacement and velocity are taken as zero. Four boundary conditions for the cantilever beam are applied. The frequency equation and mode shape equation are given in Equation 3 and Equation 4, respectively.

$$\cos\beta_n l \cdot \cosh\beta_n l = -1 \tag{3}$$

$$W_n(x) = C_n[\sin\beta_n x - \sinh\beta_n x - \alpha_n(\cos\beta_n x - \cosh\beta_n x)] \tag{4}$$

where

$$\alpha_n = \left(\frac{\sin\beta_n l + \sinh\beta_n l}{\cos\beta_n l + \cosh\beta_n l}\right) \tag{5}$$

The natural frequency of the cantilever beam can be calculated by

$$\omega = \beta^2 \sqrt{\frac{EI}{pA}} \tag{6}$$

The values of $\beta_n l$ for the first five modes are 1.875, 4.694, 7.855, 10.996 and 14.137. Using Equation 6, the first 5 natural frequencies are calculated, and the values are tabulated in Table 2.

Table 2. The first five natural frequencies of the hollow beam calculated analytically (in Hz)

ω_1	ω_2	ω_3	ω_4	ω_5
18.1	113.5	317.9	622.9	1029.6

2.2 Computational Analysis (FEM)

For the computational analysis of the hollow beam, FEM is implemented in both Matlab and Simcenter 3D. For the studies carried out in Matlab; first, the physical properties and the number of elements are assigned. Mass and stiffness matrices are written (Equations 7 and 8). Discrete and continuous solutions are performed in Matlab. For the discrete solution, the number of elements is taken as 150, which means that the element size is 5 mm. The stiffness and mass matrices for the discrete solution are

$$[K] = \frac{EI}{l^3}\begin{bmatrix} 12 & 6l & -12 & 6l \\ 6l & 4l^2 & -6l & 2l^2 \\ -12 & -6l & 12 & -6l \\ 6l & 2l^2 & -6 & 4l^2 \end{bmatrix} \tag{7}$$

$$[M] = \frac{\rho AI}{420}\begin{bmatrix} 156 & 22l & 54 & -13l \\ 22l & 4l^2 & 13l & -3l^2 \\ 54 & 13l & 156 & -22l \\ -13l & -3l^2 & -22l & 4l^2 \end{bmatrix} \tag{8}$$

The eigenvalues and eigenvectors are computed using the $[V, D] = \text{eig}\,(K, M)$ command for the continuous solution. The mode shapes are plotted in Matlab, and the first five mode shapes are shown in Figure 2. The mode shapes shown are obtained only for transverse deflection.

The calculations made so far have been done both discretely and continuously using Matlab. In continuous solution the number of degrees of freedom is infinite. Eigenvectors and eigenvalues are used for continuous solutions. In the discrete solution, the number of degrees of freedom is finite. In the discrete solution, the finite element method is used, and the discrete solution is performed by assigning stiffness and mass matrix equations.

To construct the FE model in Simcenter 3D, the element type, material properties, mesh structure, and boundary conditions must be provided. First, geometry is drawn, and a mesh structure is formed on the CAD. Afterwards, the material information is assigned. Then, 2D and 3D modeling are performed using all these steps, and the results are compared and interpreted.

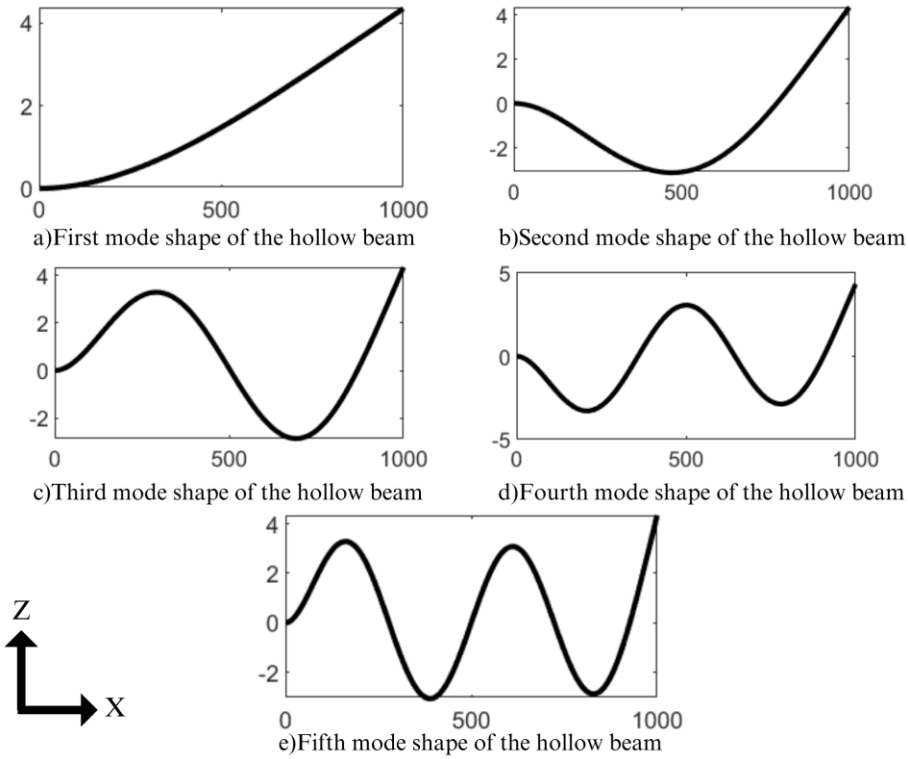

Figure 2. The first five mode shapes of the hollow beam

For 2D modeling, the midsurface of the hollow beam is extracted. Then, since the material is isotropic, the wall thickness value of the midsurface is assigned. A mesh structure is created using CQUAD 4 type four-node, two-dimensional elements. The element size for the hollow beam starts at 9 mm and is decreased until convergence in the results is achieved. Natural frequency values are determined with the Nastran SOL103 solver. Natural frequency values converge at 5 mm element size. Cantilever beam boundary conditions are used in the analysis. Additional boundary conditions are also specified for only the transverse movement of the beam.

For 3D modeling, the entire volume of the model is used, and the mesh structure is created with CHEXA8 eight-node elements. 2D mesh model results and 3D mesh model results are expected to be slightly different because the 2D mesh model considers only a flat surface, while the 3D mesh model considers the whole volume. 3D mesh models are known to be more accurate for complex geometries because they automatically form mid-nodes which take into account certain motions such as rotation and bending in the element level.

After the computational modal analysis in FEM, the accelerometer locations need to be determined for the experimental modal analysis. The accelerometer locations shown in Figure 3 are based on the computational modal analysis solution performed in Simcenter 3D software. A mesh size of 5 mm is used to determine the accelerometer locations. The maximum distance between accelerometers is determined to be 20 mm. Eight locations have been identified and one of these locations is for excitation. The distance between the nodes is measured in the software based on the fixed point for the placement of the accelerometers during the experiment. Moreover, the software shows not only the position of the accelerometers but also the angle of placement of the accelerometers. Figure 3 shows the sensor positions and angles determined by the software.

In Table 3, the calculation results for both 2D mesh and 3D mesh and Matlab results are tabulated for comparison. For FEM, mesh size is very important for processing time. To reduce processing time, the convergence of the results should be taken as a basis and the convergence should be used for the operations. The convergence value can be easily found by checking the convergence graph. The autocorrelation matrix shown in Figure 4 is a measure of the degree of correlation between two mode shapes of the same mode shape set. The results revealed a perfect correlation which means that the computation performed to determine the optimal sensor locations is successful. The diagonal matrix values are perfectly 1 and all off-diagonal terms are well below 0.1.

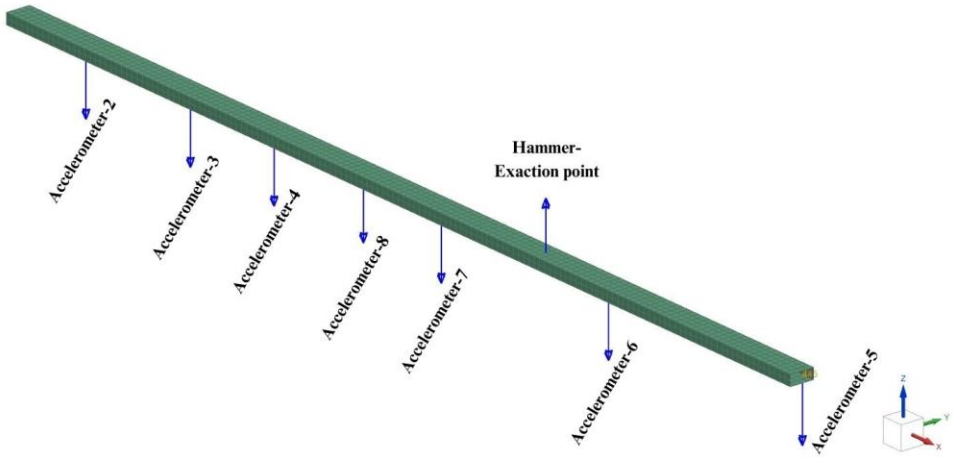

Figure 3. The optimal accelerometer locations and the optimal excitation location computed by the algorithm built-in Simcenter 3D.

Table 3. The first five natural frequencies of hollow beam obtained by different types of analysis

	Size	ω_1	ω_2	ω_3	ω_4	ω_5
Computational 2D	5 mm	18.8 Hz	117.3 Hz	326.1 Hz	632.1 Hz	1031.0 Hz
Computational 3D	5 mm	19.2 Hz	120.2 Hz	334.8 Hz	650.9 Hz	1065.0 Hz
Matlab calculations	Discrete (5mm)	18.1 Hz	113.5 Hz	317.8 Hz	622.9 Hz	1029.6 Hz
	Continuous	18.1 Hz	113.5 Hz	317.9Hz	622.9 Hz	1029.6 Hz

In the study, 2D and 3D convergence graphs are examined, and it is seen that the analysis results are very close since the experimental subject does not have a complex geometry. Therefore, the ideal mesh size is chosen as 5 mm. If the structure used had a larger and more complex geometry, the analysis results would

have shown more significant differences and consequently, the mesh size chosen would have changed accordingly.

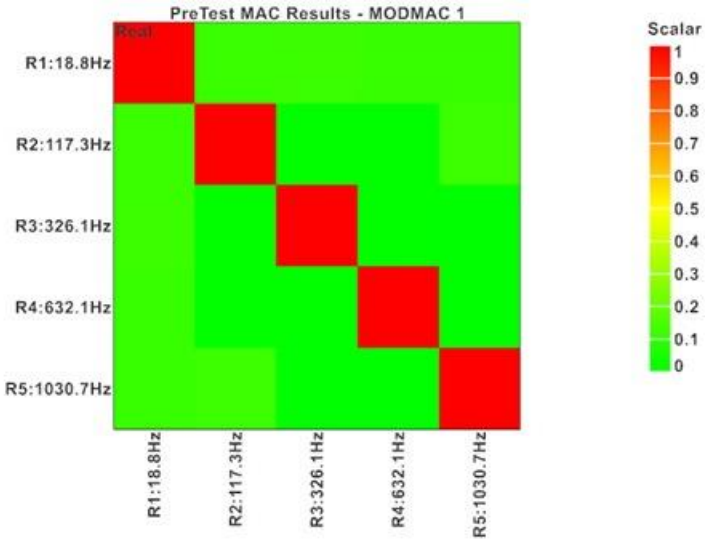

Figure 4. The autocorrelation matrix

2.3 Experimental Analysis

The hollow aluminum beam is fixed to the fixture at one end to provide a fixed-free boundary condition. An eight-channel Sinus™ mobile analyzer is used for data acquisition and recording. 7 Dytran™ uniaxial accelerometers are employed for the measurements. Accelerometers are used to transfer the acceleration signals caused by hammer strikes, i.e., the response of the structure to the analyzer. The specific accelerometer brand used in the experiment is Dytran 3035BG. Seven accelerometers were used simultaneously in the experiment. The beam is excited with an impact hammer, and an average of 3 impact measurements are recorded to be analyzed through the measurement software, Samurai. The roving hammer used during the analysis is a Dytran 5800B3 with a sensitivity value of 48.70 mV/LbF.

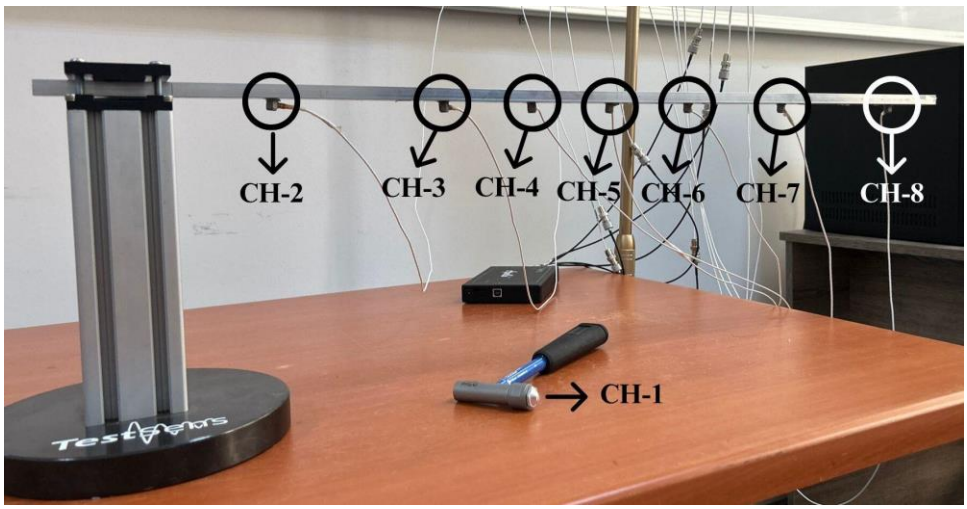

Figure 5. Experimental setup (Vibration & Acoustics Laboratory, Alanya Alaaddin Keykubat University)

The positions of the accelerometers and the location to be hit with the impact hammer were determined by an algorithm in Simcenter 3D. The locations and channel numbers are shown in Figure 5. In the mobile

analyzer, Channel#1 is reserved for the roving hammer, and other channels (#2 to #8) are employed for the accelerometers. The results are compared with FEM results and interpreted. Based on the results, the model is updated in Section 2.4.

The measurements are done to obtain the frequency response functions (FRFs), which are used to determine the natural frequencies, damping ratios and mode shapes of the engineering structures. After processing the raw data, the response can be obtained as displacement, velocity or acceleration [17].

The coherence function informs us about how well the measured data is in line with the actual response of the engineering structure and whether there are any detrimental effects in the data that affect the response i.e., nonlinearities, self-induced vibration, etc. In modal analysis, it is a measure of the correlation between the input excitation and the measured response. In the cantilever beam experiment, the resulting high coherence values indicate that the measured response is highly correlated with the excitation signal, and the measured data are reliable for postprocessing [18]. To give an idea, an FRF function and its coherence function obtained from Channel#6 are shown in Figure 6. The damped natural frequency values obtained during the experimental study are tabulated in Table 5. The mathematical relation between the undamped natural frequencies (ω_n) and the damped natural frequencies (ω_d) is

$$\omega_d = \omega_n\sqrt{1-\zeta} \tag{9}$$

where ζ is the damping ratio.

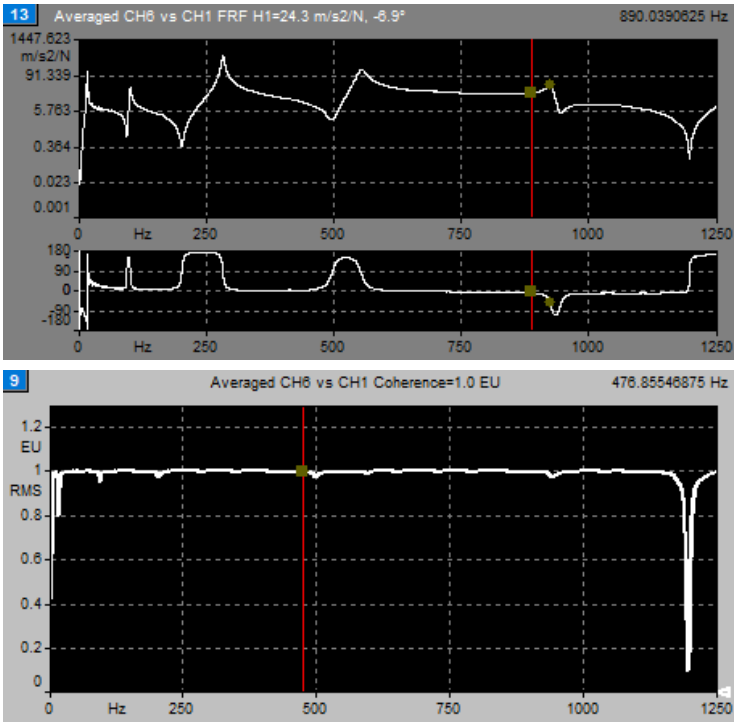

Figure 6. The FRF (top) and the coherence function (bottom) graphs obtained from Channel#6

Table 5. The first five natural frequencies of hollow beam obtained by the experimental modal analysis

ω_1	ω_2	ω_3	ω_4	ω_5
16.6 Hz	101.5 Hz	283.1 Hz	556.4 Hz	924.9 Hz

2.4 Model Update

The data acquired from the experimental modal analysis study is compared with the results of the computational modal analysis. The experimental data is taken as reference data and the computational model is updated to minimize the difference between the two models. The mode shapes are compared using the modal assurance criterion (MAC). It is observed that the mode shapes are similar, but the frequency values associated with the mode shapes are slightly different. The reason is that the natural frequency values (ω_n) obtained from the computational analysis are undamped, while the values obtained from the experimental modal analysis are the damped natural frequencies (ω_d). The damping ratio (ζ) is measured during the experiments to be included in the computational model. MAC compares the mode shapes in two sets of modes and indicates the degree of consistency between the shapes. The MAC is computed using the following equation:

$$\mathrm{MAC}(A_k, A_l) = \frac{\left|\sum_{j=1}^{N} \Psi_{\mathrm{Akj}} \Psi_{\mathrm{Alj}}{}^{*}\right|^2}{\sum_{j=1}^{N} \Psi_{\mathrm{Akj}} \Psi_{\mathrm{Akj}}{}^{*} \sum_{j=1}^{N} \Psi_{\mathrm{Alj}} \Psi_{\mathrm{Alj}}{}^{*}} \tag{10}$$

where Ψ_{Akj} and Ψ_{Alj} are the jth value of the mode shape vectors $\{\Psi_{\mathrm{Ak}}\}$ and $\{\Psi_{\mathrm{Al}}\}$, respectively. First, 7 accelerometers are placed on the FE model obtained from Simcenter 3D for the analysis using nCode. The positions of the accelerometers are the same as in the experimental setup. The positions and measurement directions of the accelerometers on the hollow beam are shown in Figure 7.

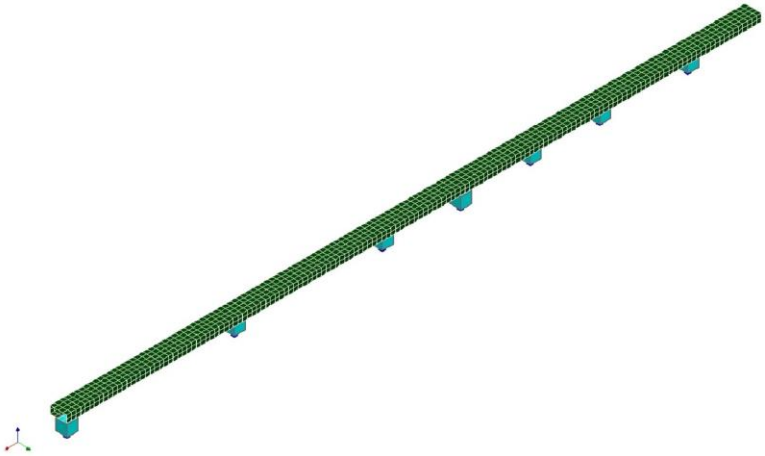

Figure 7. Positions of the accelerometers on the hollow beam (nCode analysis)

Then, using nCode software, a MAC analysis is performed to compare the first 5 mode shapes obtained from the computational analysis results. The first 5 experimental mode shapes are generated in nCode. A comparison of the computational and experimental mode shapes is given in the next subsection.

3. COMPARISON OF RESULTS

Analytical, experimental, and computational results are obtained throughout the study. The analytical calculations do not consider damping, which is inherent in all physical systems. The initial computational model also does not include damping. The damping was measured experimentally using FRFs and incorporated into the updated model by adding viscous damping elements. The viscous damping elements added to the updated computational model are shown in Figure 8. The 1D viscous damping elements are assigned a damping value of 0.32 N·s/mm (shown in orange in Figure 8).

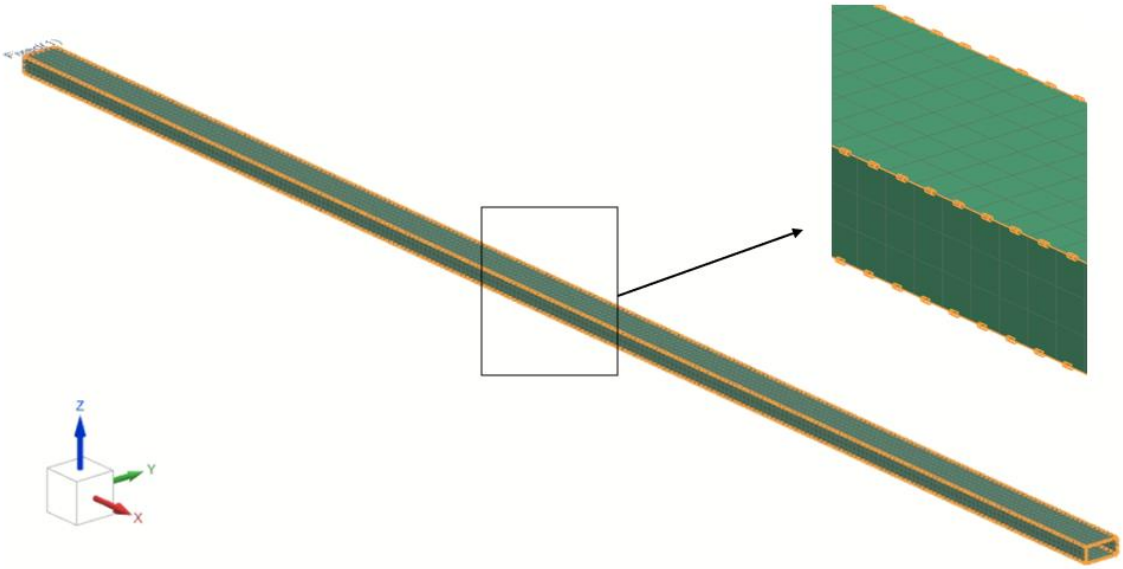

Figure 8. Viscous damping elements introduced the updated computational model (shown in orange)

Table 5. The first five mode frequencies of the hollow beam obtained by the analytical, computational and experimental analysis (in Hz)

Analysis	ω_1	ω_2	ω_3	ω_4	ω_5
Analytical	18.1	113.5	317.9	622.9	1,029.6
Matlab (discrete solution)	18.1	113.5	317.9	622.9	1,029.6
Computational (initial model)	18.8	117.4	326.3	632.4	1,031.0
Experimental	16.6	101.5	283.1	556.4	924.9
Computational (updated model)	17.1	100.2	285.1	559.2	906.0

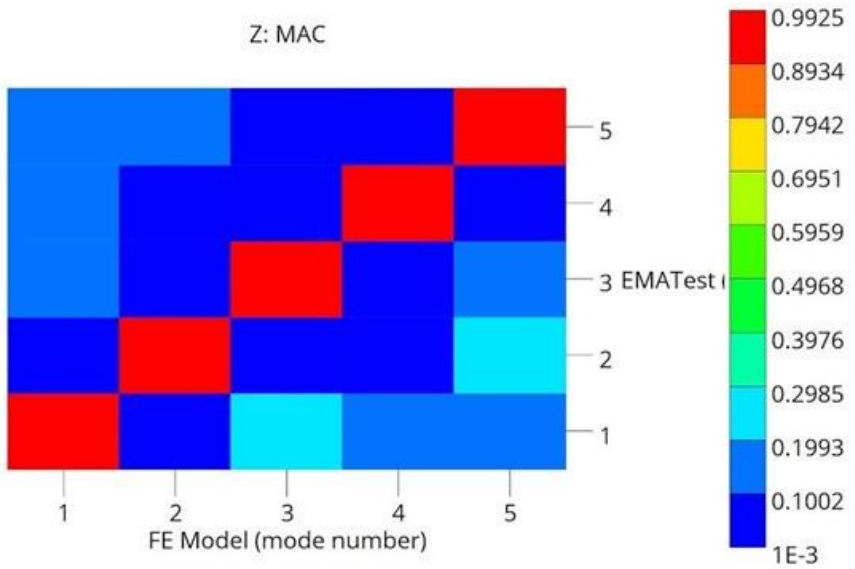

Figure 9. Cross-correlation of MAC matrix: comparison of experimental and computational mode shapes

Computational mode shapes	Experimental mode shapes
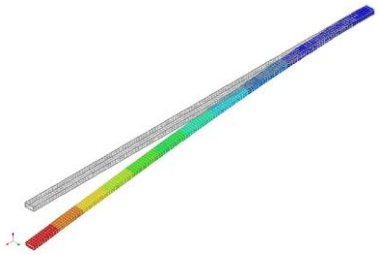	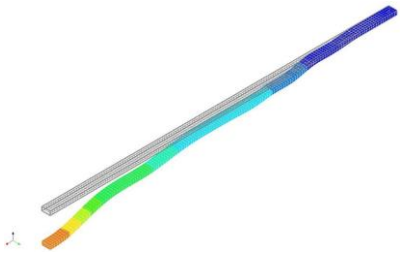
1st mode, 17.1 Hz	1st mode, 16.6 Hz
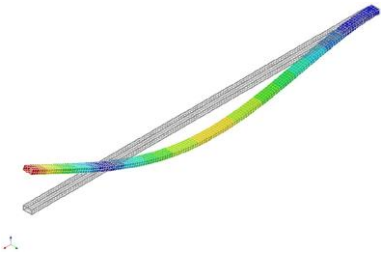	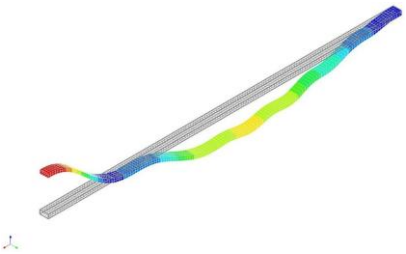
2nd mode, 100.2 Hz	2nd mode, 101.5 Hz
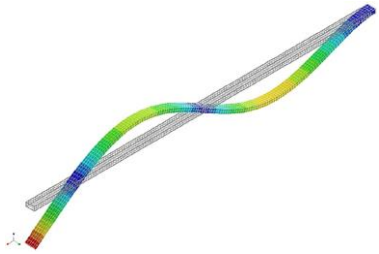	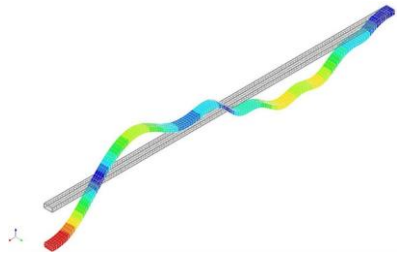
3rd mode, 285.1 Hz	3rd mode, 283.1 Hz
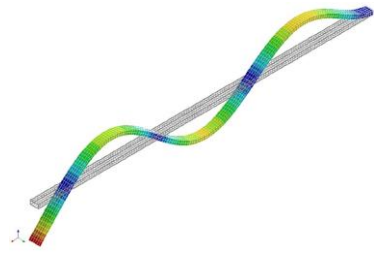	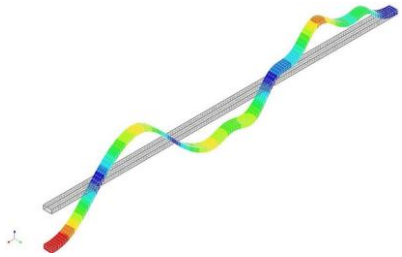
4th mode, 559.2 Hz	4th mode, 556.4 Hz
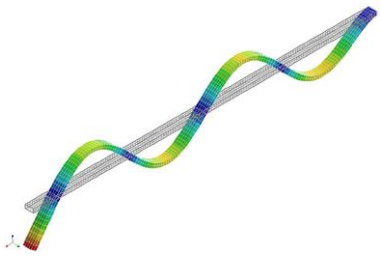	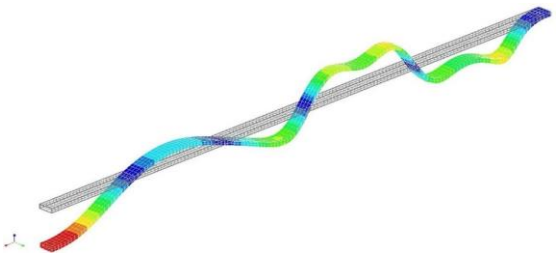
5th mode, 906.0 Hz	5th mode, 924.9 Hz

Figure 10. Computational (left column) and experimental (right column) mode shapes

The results tabulated in Table 5 show that the updated computational model is the model that best fits the experimental results in terms of mode frequencies. The cross-correlation MAC matrix compares the computationally and experimentally derived eigenvectors (aka mode shapes). The color scale in Figure 9 represents correlation values ranging from 0 to 1. As the value approaches 1, the similarity increases and as the value approaches 0, the similarity decreases. As a result of the study, values close to 1 are obtained in the diagonally positioned cross-correlation MAC matrix. This diagonal arrangement can be interpreted as a successful completion of the conducted analysis. The experimental and computational mode shapes are compared in Figure 10.

4. CONCLUSION

Structural parameter estimation is affected by uncertainties which are present in the system. The relevant literature reveals the importance of model updating. A technique is proposed to estimate spatially distributed parameters of samples with regular geometry structure using Karhunen Loève expansion and sensitivity based FRF model updating [19]. A model updating study is performed on an H-cross section steel beam [20]. The model is updated using natural frequencies measured in an impact hammer test of the beam structure and the validity of the updated model is confirmed by the strain responses measured from the test. In a recent study, several model updating methods based on full-scale model tests of track beams are compared [21]. The results of a model update study on a composite beam show that the uncertainties in the simulated finite element model like the modulus of elasticity of the fibers and matrices, individual densities, modulus of rigidity, and most importantly the fiber orientations can be effectively corrected by using direct updating method [22].

In this study, the dynamic properties of an aluminum hollow beam are investigated using analytical, computational, and experimental methods. An analytical solution is carried out according to the assumptions of the Euler-Bernoulli beam theory. The assumptions of the theory negatively affect the accuracy of the results as the frequency range increases. Discrete and continuous solutions for the structure are realized using Matlab. The number of elements is taken as 150 for the discrete Matlab solution and infinite for the continuous solution. The tabulated results in Table 5 show that the analytical and Matlab solutions overestimate the mode frequencies compared to the experimental results.

The initial computational model, which does not consider damping, also overestimates the results. The computational model is updated regarding the experimental model. The damping behavior inherent in all physical structures is measured experimentally and added to the updated computational model. It is then observed that the experimental and computational results match well. The average error between the computational and experimental results for the first five damped natural frequency values is calculated to be 1.5%. In line with the former studies [19-22], this study shows the importance of model updating for correct analysis and design. Differently, in this study, damping elements were also taken into account which refines and improves the results in terms of suppressing the errors between the experimental and computational results.

5. ACKNOWLEDGEMENT

This research was supported by The Scientific and Technological Research Council of Turkey (TUBITAK), 2209A Program, Project number: 1919B012220892.

REFERENCES

[1] Zannon, M. (2014). Free vibration of thin film cantilever beam. *International Journal of Engineering and Technical Research (IJETR)*, *2*, 304-314.

[2] Piranda, J., Corn, S., Bouhaddi, N., Stawicki, C., Van Herpe, F., & Cudney, H. H. (1998, February). Determination of equivalent beam properties for hollow girders typically used in the automotive industry. In *Society for Experimental Mechanics, Inc, 16 th International Modal Analysis Conference.* (Vol. 2, pp. 1227-1232).

[3] Machhan, R. A., & Könke, C. (2021). Investigation of different types of damping effects for automotive components–preliminary work. *Materials Today: Proceedings*, *46*, 9659-9666.

[4] Demirtaş, A., & Bayraktar, M. (2019). Free vibration analysis of an aircraft wing by considering as a cantilever beam. *Selçuk Üniversitesi Mühendislik, Bilim Ve Teknoloji Dergisi*, *7*(1), 12-21.

[5] Chaphalkar, S. P., Khetre, S. N., & Meshram, A. M. (2015). Modal analysis of cantilever beam structure using finite element analysis and experimental analysis. *American Journal of Engineering Research*, 4(10), 178-185.

[6] İnan, C. Y., & Oktav, A. (2021). Model Updating of a Euler-Bernoulli Beam Using the Response Method. *Kocaeli Journal of Science and Engineering*, *4*(1), 16-23.

[7] Flaieh, E. H., Dwech, A. A., & Mosheer, M. R. (2021, February). Modal analysis of fixed-free beam considering different geometric parameters and materials. In *IOP Conference Series: Materials Science and Engineering* (Vol. 1094, No. 1, p. 012118). IOP Publishing.

[8] Wu, J. S., & Chou, H. M. (1998). Free vibration analysis of a cantilever beam carrying any number of elastically mounted point masses with the analytical-and-numerical-combined method. *Journal of Sound and Vibration*, *213*(2), 317-332.

[9] Prashant, S. W., Chougule, V. N., & Mitra, A. C. (2015). Investigation on modal parameters of rectangular cantilever beam using experimental modal analysis. *Materials Today: Proceedings*, *2*(4-5), 2121-2130.

[10] Imran, M., Abbasi, A. A., & Hyder, M. J. (2016, October). Determination of modal characteristics of cantilever beam. In *2016 International Conference on Emerging Technologies (ICET)* (pp. 1-3). IEEE.

[11] Mekalke, G. C., & Sutar, A. V. (2016). Modal analysis of cantilever beam for various cases and its analytical and FEA analysis. *International Journal of Engineering Technology, Management and Applied Sciences*, *4*(2), 60-66.

[12] Jassim, Z. A., Ali, N. N., Mustapha, F., & Jalil, N. A. (2013). A review on the vibration analysis for a damage occurrence of a cantilever beam. *Engineering Failure Analysis*, *31*, 442-461.

[13] Korucu, S., Gök K., Tümsek, M., Soy, G., & Gök, A. (2019). Farklı profillere sahip kirişlerde meydana gelen eğilme gerilmesi ve sehim miktarının teorik ve nümerik yöntemler ile analizi. *Dokuz Eylül Üniversitesi Mühendislik Fakültesi Fen ve Mühendislik Dergisi*, *21*(62), 469-482.

[14] Inman, D.J., Engineering Vibration. 3rd ed. 2007, New Jersey: Prentice Hall.

[15] Timoshenko, S. P., & Gere, J. M. (2009). Theory of Elastic Stability. Courier Corporation.

[16] Young, D., & Felgar, R. P. (1949). Tables of characteristic functions representing nomal modes of vibration of a beam. Bureau of Engineering Research.

[17] Irvine, T. (2000). An introduction to frequency response functions. *Rapport, College of Engineering and Computer Science*, *2000*.

[18] Ewins, D. J. (2009). *Modal testing: theory, practice and application*. John Wiley & Sons.

[19] Machado, M.R., Adhikari, S., Dos Santos, J.M.C. & Arruda, J.R.F. (2018). Estimation of beam material random field properties via sensitivity-based model updating using experimental frequency response functions. *Mechanical Systems and Signal Processing*, 102,180-197.

[20] Oh, B. K., Kim, M. S., Kim, Y., Cho, T., & Park, H. S. (2015). Model updating technique based on modal participation factors for beam structures. *Computer-Aided Civil and Infrastructure Engineering*, 30(9), 733-747.

[21] Zhong, J., Gou, H., Zhao, H., Zhao, T., & Wang, X. (2022, January). Comparison of several model updating methods based on full-scale model test of track beam. *Structures*, 35, 46-54.

[22] Bagha, A. K., Gupta, P., & Panwar, V. (2020). Finite element model updating of a composite material beam using direct updating method. *Materials Today: Proceedings*, 27, 1947-1950.

ALKU Journal of Science 2023, Sayı 5 (3): 163-175
e-ISSN: 2667-7814

Original Article

Optimization Studies of Mg/Al-NO_3 Layered Double Hydroxide Nanoparticles by Hydrothermal Treatment

Kevser Bal[1*], Sema Şentürk[1], Özlem Kaplan[2], Mehmet Koray Gök[1], Saadet Kevser Pabuccuoğlu[1]

[1]*Istanbul University-Cerrahpasa, Faculty of Engineering, Department of Chemical Engineering, Istanbul, Turkey*

[2]*Alanya Alaaddin Keykubat University, Rafet Kayış Faculty of Engineering, Department of Genetics and Bioengineering, Antalya, Turkey*

**kevser.bal@iuc.edu.tr*

Abstract

Layered Double Hydroxide-based nanoparticles offer significant advantages in biological applications with high biocompatibility and low cytotoxicity. In this study, nanoparticles (nMg/Al-NO_3-LDH) were synthesized by the co-precipitation method, and synthesis optimization of the nanoparticles was carried out by hydrothermal treatment. The effect of hydrothermal treatment on Z-average and surface charge was evaluated. Experiments were performed at 80˚C and 100˚C in the range of 2-48 h by using different stirring rates (250, 1000, and 1500 rpm) and without stirring. Dynamic Light Scattering (DLS) was used to assess the particle size (nm), polydispersity index (PDI), and zeta potential (mV) of the nanoparticles. The chemical structure of nanoparticles was characterized by Fourier Transform Infrared spectrometry (FTIR). As a result, nanoparticles with an optimum particle size of 86.87 nm, a PDI of 0.132, and a zeta potential (mV) of 44.4±8.74 were obtained at 80˚C, 48h and 250 rpm. The data showed that Mg/Al-NO_3-LDH nanoparticles have suitable physical properties for biological applications.

Keywords: Layered double hydroxide nanoparticles, Hydrothermal treatment, Particle size optimization, Inorganic materials

Mg/Al-NO_3 Çift Tabakalı Hidroksit Nanopartiküllerinin Hidrotermal İşlem İle Optimizasyonu Çalışmaları

Özet

Çift Tabakalı Hidroksitler yüksek biyouyumluluk ve düşük sitotoksisite ile biyolojik uygulamalarda önemli avantajlar sunar. Bu çalışmada nanopartiküller (nMg/Al-NO_3-LDH) birlikte çöktürme yöntemiyle sentezlendi ve nanopartiküllerin sentez optimizasyonu hidrotermal işlem altında gerçekleştirildi. Hidrotermal işlemin partikül boyutu ve yüzey yükü üzerindeki etkisi değerlendirildi. Deneyler 80˚C ve 100˚C'de, 2-48 saat aralığında ve çeşitli karıştırma hızlarında 250, 1000, 1500 rpm gerçekleştirildi. Nanopartiküllerin partikül boyutu (nm), polidispersite indeksi (PDI) ve zeta potansiyel (mV) değerleri Dinamik Işık Saçılımı (DLS) ile saptandı. Nanopartiküllerin kimyasal yapısı Fourier Dönüşümü Kızılötesi spektrometresi (FTIR) ile karakterize edildi. Sonuç olarak, 80˚C, 48 saat ve 250 rpm'de optimum partikül boyutu 86.87 nm, polidispersite indeksi (PDI) 0.132 ve zeta potansiyeli (mV) 44.4±8.74 olan nanopartiküller elde edildi. Veriler, biyolojik uygulamalarda kullanıma yönelik Mg/Al-NO_3-LDH nanopartiküllerinin uygun fiziksel özelliklere sahip olduğunu gösterdi.

Anahtar Kelimeler: Çift tabakalı hidroksit nanopartiküller, Hidrotermal işlem, Partikül boyutu optimizasyonu, İnorganik malzemeler

Geliş/Received: 3 Ekim/October 2023
Kabul Ediliş/Accepted: 20 Ekim/October 2023

1. INTRODUCTION

Layered Double Hydroxides (LDHs) are layered materials with a unique 2-dimensional structure and biocompatibility. The alternating pattern of positively charged metal hydroxide layers and negatively charged interlayer exchangeable anions characterizes them [1]. LDHs have recently gained popularity due to their unique properties and versatile applications in various fields, including catalysis, drug delivery, and environmental remediation [2]. LDH has superior properties such as good biocompatibility, low cytotoxicity, high loading capacity, diverse functionality, tunable particle size, targeted delivery, and protection of biomolecules from external chemical and biological attacks [3]. Numerous research has focused on the utilization of LDH as a carrier of biomolecules such as vitamins [4], anti-inflammatory drugs [5], anti-cancer drugs [6], neurodegenerative drugs [7] and genes [8,9]. In synthesizing LDH nanoparticles, the co-precipitation method is a widely used technique known for its simplicity and efficiency in producing well-defined nanostructures [10].

LDH possesses a general chemical formula of $[M^{II}_{1-x} M^{III}_{x}(OH)_2]^{x+} (A^{n-})_{x/n} \cdot mH_2O$, wherein M^{II}, M^{III} and A^{n-} represent divalent a metal cation, a trivalent metal cation and an interlayer anion, respectively. LDH has a layered crystal structure that varies widely depending on the structure of the cations M^{II}/M^{III} molar ratios and anion type. The range $0.2 < x < 0.33$ (M^{II}/M^{III} ratio between 2: 1 and 4: 1) is suitable for pure LDH synthesis. In the case of $x > 0.33$, the formation of $M(OH)_3$ occurs; likewise, $M(OH)_2$ is formed at $x < 0.2$ [11,12].

Hydrothermal treatment is an important step in improving the properties of LDH nanoparticles, as it allows fine-tuning parameters such as temperature, time, and stirring speed [13]. In this study, the synthesis of nMg/Al-NO_3-LDH was optimized for use in biological applications. nMg/Al-NO_3-LDH was prepared by the co-precipitation method, and the hydrothermal optimization of the nMg/Al-NO_3-LDH was examined. It is well established in biological applications that parameters such as cellular uptake, biodistribution, and biocompatibility are significantly influenced by particle size and surface charge [14].

In this regard, the effect of synthesis conditions such as temperature, time, and stirring rate on the particle characteristics was investigated. The size (nm), PDI and zeta potential (mV) of nMg/Al-NO_3-LDH prepared under various conditions were revealed by Dynamic Light Scattering (DLS) analysis, while their chemical structure was illuminated by Fourier Transform Infrared Spectrometer (FT-IR). Especially there is no study on the nanoparticle size of stirring rate during hydrothermal treatment, but the data obtained with this parameter created a meaningful and important result and brought innovation and originality to our study.

2. MATERIAL AND METHOD

2.1 Material

Mg $(NO_3)_2.6H_2O$ (>99%) and Al $(NO_3).9H_2O$ was obtained from Merck. NaOH (>98-100) purchased from Sigma–Aldrich.

2.2 Synthesis and Optimization of nMg/Al-NO_3-LDH

nMg/Al-NO_3-LDH were synthesized using a coprecipitation step followed by a hydrothermal treatment process [15]. 10 mL aqueous solution of 3 mmole Mg $(NO_3)_2.6H_2O$, and 1 mmole Al $(NO_3).9H_2O$, ([Al]/([Mg]+[Al]); 0.25) was added quickly in NaOH solution (0.15 M, 40 mL) under vigorous magnetic stirring continued for 10 min. This acquired LDH suspension was separated by centrifuging for 5 min at 4500 rpm. LDH slurry was washed, dispersed in 50 mL of deionized water, and transferred into an autoclave (Berghof Highpreactor BR-HS; Germany). Hydrothermal treatments were carried out at 80˚C and 100˚C, in a range of 2-48 h and with different stirring rates (250, 1000, and 1500 rpm) and without stirring, respectively. Figure 1 depicts the synthesis of Mg/Al-NO3-LDH nanoparticles.

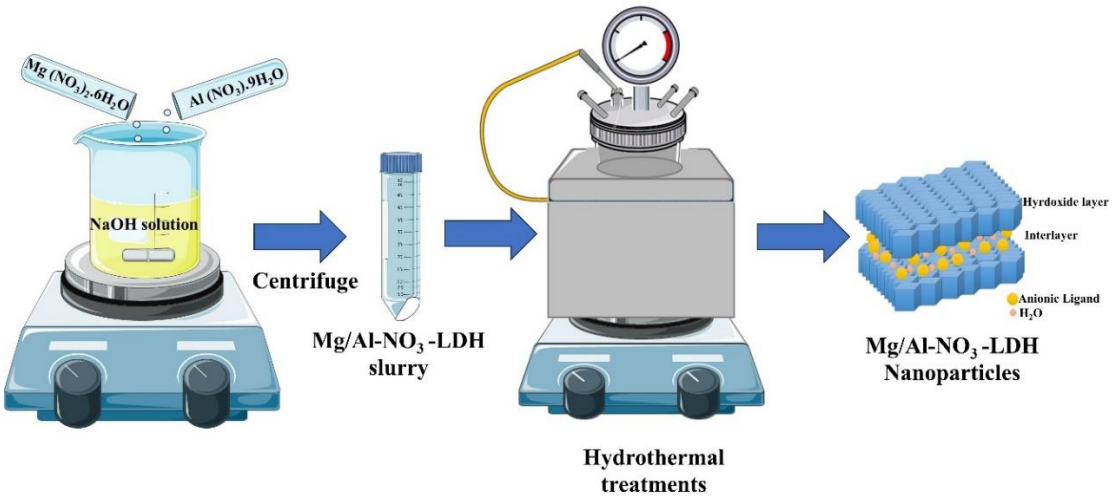

Figure 1. Schematic illustration of nMg/Al-NO_3-LDH synthesis

After the co-precipitation process, the effect of hydrothermal treatment conditions was examined by changing the temperature, stirring rate and time on nanoparticle characteristics. First, the hydrothermal treatment process was examined for the different stirring rates (250 rpm, 1000 rpm, 1500 rpm). For this purpose, samples were taken at different time intervals for different stirring rates, and then particle size (nm), PDI, and zeta potential (mV) values were determined. Secondly, the effect of temperature (80°C and 100°C) was examined after determining the appropriate stirring rate. Finally, the effect of hydrothermal treatment time (2h, 4h, 6h, 8h, 24h and 48 h) on particle size, PDI, and zeta potential value was also examined.

2.3. Characterization of nMg/Al-NO_3-LDH

2.3.1 FTIR analysis

The structure of nMg/Al-NO_3-LDH was identified on a Fourier transform infrared (FTIR) (Agilent Cary 630, USA) using a pellet prepared with 1 mg of the sample and 200mg of KBr. The absorption spectra were obtained in the wavenumber range of 4000-650 cm^{-1}.

2.3.2 Determination of mean particle size, PDI and zeta potential

Photon correlation spectroscopy (Nano ZS, Malvern UK) was used to determine the Z-average and PDI of nMg/Al-NO_3-LDH. The same instrument was used to determine the surface charge of nanoparticles. The measurement results were repeated three times.

2.4 Colloidal Stability of nMg/Al-NO_3-LDH

The colloidal stability of nMg/Al-NO_3-LDH was examined by storing dispersions at +4 ± 1 °C. Particle size, PDI, and zeta potential value were measured by taking weekly samples. Stability was checked over 5 weeks, and the measurement results were repeated three times.

2.5 Statistical Evaluation

Statistical analysis and similar data sets were analyzed using GraphPad Prism 8.0 software and a two-way ANOVA with the Sidak test. Statistical significance was evaluated as a probability value of 0.05.

3. RESULTS AND DISCUSSION

3.1 Synthesis and Characterization of nMg/Al-NO_3-LDH

As aforementioned in section 2.2, nMg/Al-NO_3-LDH was synthesized by the co-precipitation method using the magnesium and aluminum salts. Afterward, the stable suspension containing nMg/Al-NO_3-LDH was obtained by hydrothermal treatment. To elucidate the resulting structure, the nMg/Al-NO_3-LDH suspension was lyophilized, and the structure was characterized by FTIR analysis using the dry sample.

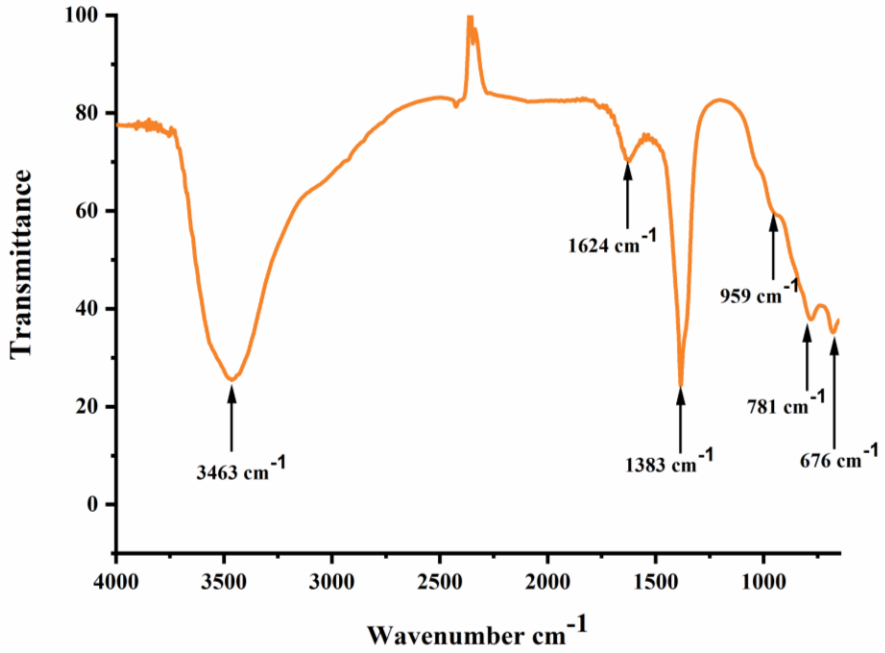

Figure 2. FTIR spectra of nMg/Al-NO_3-LDH

As illustrated in Figure 2, FTIR spectra of nMg/Al-NO_3-LDH are taken for the range of 4000-650 cm^{-1}. The broad absorption band in the 3250-3800 cm^{-1} region (maximum appeared at about 3463 cm^{-1}) and the broad shoulder appeared at about 3580 cm^{-1} are related to the symmetrical and asymmetric vibrations of the hydrogen-bonded O-H groups in lattice structure (Mg/Al-OH or Al-OH) and interlayer water molecules surrounding the exchangeable anions [16]. The small sharp absorption band seen at 1624 cm^{-1} is attributed to the deformation and bending vibrations of the H_2O molecules in the H_2O-CO_3^{2-} structure. The sharper band at about 1383 cm^{-1} was also assigned to the stretching vibrations of the NO_3^- anions in the interlayer region. The broad shoulder at about 1359 cm^{-1} was also assigned to the symmetric stretching vibrations of the unidentate CO_3^{2-} anions, which may have entered the structure during precipitation or purification. Hence, CO_3^{-2} and NO_3^{-1} anions in the interlayer of LDH are observed to be overlapped as the one sharp absorption band at 1383 cm^{-1} [4]. Absorption bands are seen as small sharp or small shoulders of approximately 500-1000 cm^{-1} caused by vibrations of the LDH lattice structure, which are Mg-O / Al-O / O-Al-O / O-Mg-O, Al-OH, H_2O molecules [17]. Consequently, FTIR spectra of nMg/Al-NO_3-LDH confirm its molecular structure.

3.2 Optimization Studies of nMg/Al-NO_3-LDH

Nanoparticulate systems are a very important developing field as drug or gene carrier systems [18]. It is known that the key factor to achieve maximum therapeutic effectiveness in the applications of these systems is the control of particle size, PDI and surface charge [14]. Additionally, some studies have revealed that

the particle size and surface charge of nanoparticles are more important than the nanoparticle structure in biological applications [14].

In optimizing the synthesis of nMg/Al-NO_3-LDH, the effect of hydrothermal treatment conditions such as time (2h, 4h, 6h, 8h, 24h), stirring rate (250 rpm, 1000 rpm and 1500 rpm) and without stirring on the characteristics of the nanoparticles were investigated at the constant temperature 100°C, which indicated in the literature [19-24]. According to the results (Figure 3), hydrothermal treatment conditions significantly affect particle size and PDI. As known, hydrothermal treatment increases the kinetic energy and Brownian motion that can overcome the adhesive effect and interaction between aggregates [19]. Thus, stable LDH suspension is obtained due to electrostatic repulsion between positive particles. The obtained values in Figure 3 show that the Z-average size varies between 77.47±0.150 nm and 133.8±3.195 nm due to the stirring rate. Moreover, hydrothermal treatments were carried out with and without stirring in the autoclave to observe the effect on particle size. All nMg/Al-NO_3-LDH were obtained smaller than 200 nm particle size at hydrothermal treatment conditions with variable stirring rate and time in the autoclave. This range is considered small-sized for nanoparticular systems [25] and a suitable agent for drug/gene carrier systems in target therapies [26-28]. Especially when the stirring rate is 250 rpm, it can be seen that all the results are below 100 nm (Table 1). This situation creates a great advantage for nanoparticle systems that target the blood-brain barrier, especially requiring small nanoparticle size (<200 nm) [29].

The PDI is defined as the level of non-uniformity in the size distribution of particles [30]. If the PDI value of the nanoparticle system is <0.1, it is highly uniform, and if it is between 0.1 and 0.4, it is considered to be moderately uniform. These two ranges are considered suitable for nanoparticular systems for drug/gene delivery systems [27,28,31]. If this value is >0.4, it indicates a high level of nanoparticle size variation and is unsuitable for drug/gen carrier systems [32]. Based on this, when we examined the PDI values, it was observed that the measured values varied between 0.185±0.014 and 0.404±0.0122 (Figure 3). In fact, all the obtained results have a good PDI value, of course, considering that specific values will be required depending on the carrier system to be customized.

Zeta potential, also called electrokinetic potential, is measured by the movement of particles dispersed in a liquid towards the positive or negative domain depending on the surface charge ratio when an electrical field is applied to the liquid [32]. Zeta potential is a highly significant characteristic of colloids or nanosuspension, and its value is strongly connected to suspension stability and particle surface shape. It is evaluated as a parameter of the impacts of pH, ionic strength, and the kind of ions in suspension [33,34]. When we examined all the zeta potential results, the values (between 37.8±6.39 and 51.4±6.82) were close to each other (Figure 3). The distribution is considered stable in colloidal systems where the zeta potential is higher than +30 mV or lower than −30 mV [35]. Accordingly, the results show that LDH nanoparticles with high cationic charge are stable.

According to Figure 3, the diversity in stirring rate resulted in a statistically significant change in particle size and PDI values, while the change in zeta potential was statistically insignificant at all times tested. However, when the stirring rate increased to 1500 rpm, particle size, PDI, and zeta potential value also increased due to increasing the intraparticle interaction. The obtained results revealed that the optimal stirring rate is 250 rpm.

Based on the literature, there are many studies on LDH [19,34]. Although there are different studies on parameters such as anion type in the structure, temperature, concentration and time, no study has been found investigating the effects of stirring speed on particle size, PDI and zeta potential in hydrothermal treatment. When the data obtained is examined, it shows that stirring rate is a statistically significant parameter of particle size in hydrothermal treatment. The stirring rate in the hydrothermal treatment on LDH nanoparticle creates a unique value for this study and distinguishes it from other studies.

Table 1. The zeta potential, particle size and PDI values of nMg/Al-NO_3-LDH obtained hydrothermal treatment conditions (250rpm, 100˚C, 24h)

	Time (h)	***Z-average (nm) ±SD***	***PD ±SD***	***Zeta potential (mV) ±SD***
100 ˚C-0 rpm	2 h	108,0±1,761	0,185±0,014	43,6±5,46
	4 h	105,0±0,5	0,210±0,003	45,1±7,51
	6 h	102,4±0,585	0,280±0,020	48,1±9,31
	8 h	100,0±1,217	0,245±0,004	42,4±5,86
	24 h	106,9±0,556	0,231±0,009	37,8±6,39
100°C -250 rpm	2 h	79,97±0,527	0,250±0,001	40,1±8,58
	4 h	77,47±0,150	0,211± 0,004	43,9±7,92
	6 h	77,59±0,820	0,192±0,013	45,6±7,74
	8 h	85,0±0,686	0,211±0,007	45,1±7,15
	24 h	95,10±0,707	0,201±0,004	44,8±6,87
100 ˚C-1000 rpm	2 h	106,9±0,862	0,247±0,006	43,7±53,8
	4 h	81,82±0,841	0,254±0,010	43,3±14,7
	6 h	77,18±0,31	0,229±0,004	44,2±6,37
	8 h	81,07±0,520	0,237±0,008	42,9±5,49
	24 h	86,34±0,89	0,208±0,011	42,7±8,62
100 ˚C-1500 rpm	2 h	93,68±0,826	0,404±0,0122	50,0±8,51
	4 h	99,02±2,933	0,378±0,006	51,2±8,42
	6 h	99,74±1,065	0,382±0,006	50,0±3,6
	8 h	104,0±2,592	0,380±0,005	51,4±6,82
	24 h	133,8±3,195	0,376±0,017	49,9±8,58

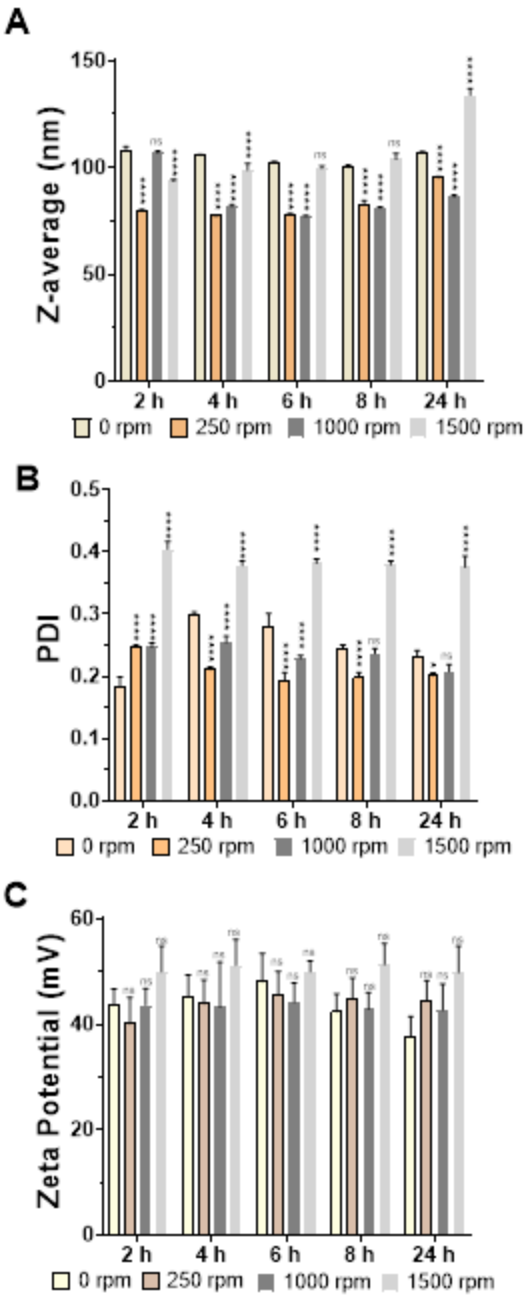

Figure 3. The particle size (nm) (A), PDI (B) and Zeta potential (mV) (C) of nMg/Al-NO_3-LDH in various parameters 0 (without stirring), 250, 1000 and 1500rpm. The data is provided as mean SEM (n = 3). The following statistical significance levels were used: *p < 0.05, **p < 0.01, ***p < 0.001, and ****p < 0.0001, ns: not significant.

To investigate the impact of temperature on the size and surface charge of nMg/Al-NO_3-LDH the stirring rate was kept constant at 250 rpm and the synthesis was carried out at 80°C. When the temperature was changed to 80°C, particle size and size distribution decreased at 24h, with no significant change in surface charge (Figure 4 and Table 2).

Table 2. Effect of temperature on the particle size (A), PDI (B) and zeta potential (C)

	Time (h)	*Z-average (nm) ±SD*	*PD ±SD*	*Zeta potential (mV) ±SD*
80°C – 250 rpm	2h	93,92±0,382	0,238±0,0122	44,6±6,52
	4 h	75,54±0,337	0,272±0,250	44,2±5,46
	6 h	73,86±0,864	0,208±0,0057	45,1±4,49
	8 h	77,72±1,130	0,224±0,005	45,3±3,95
	24 h	88,35±1,751	0,173±0,012	47,5±6,25

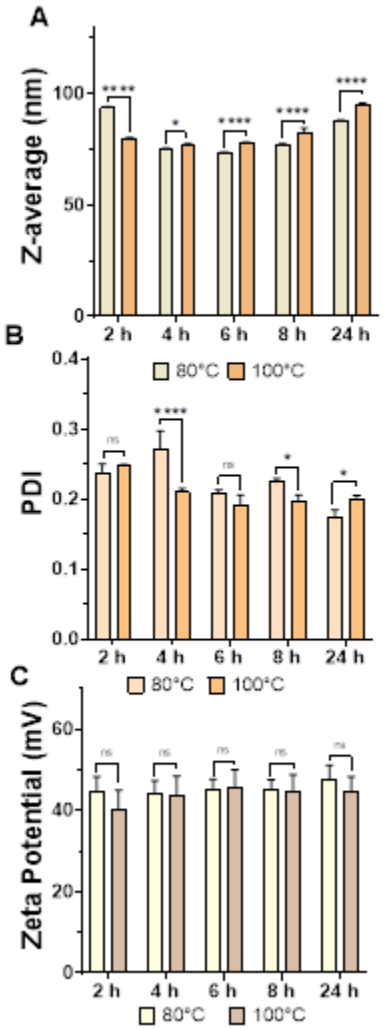

Figure 4. Effect of temperature on the particle size (A), PDI (B) and zeta potential (C)
The data is provided as mean SEM (n = 3). The following statistical significance levels were used: *p < 0.05, **p < 0.01, ***p < 0.001, and ****p < 0.0001, ns: not significant.

The particle size and PDI value of nMg/Al-NO_3-LDH are positively affected depending on hydrothermal treatment time (Table 3). Without hydrothermal treatment, LDH slurry has a glue effect causing aggregation, distribution over a wide range and a large PDI value.

Table 3. Effect of hydrothermal treatment time on the LDH particle size, PDI and zeta potential in 80˚C temperature, 250 rpm stirring rate.

Time (h)	*Z-average (nm)*	*PDI*	*Zeta potential (mV) ±SD*
without hydrothermal treatment	358.8±4,747	0.513±0,027	-
24	88.35±1,75	0.173±0,019	47.5±6.25
48	86.87±0.320	0.132±0,018	44.4±8.74

When the hydrothermal treatment time reached 24 h, it was seen that the nMg/Al-NO_3-LDH was a stable monodisperse nanosuspension with narrower size distributions i.e. lower PDI. However, a peak of about 1% is seen around 5000 nm of hydrothermal treatment time at 24 h. Therefore, the hydrothermal treatment time was raised to 48 h. Thus, it was observed that the unwanted second peak (~5000 nm) disappeared and the PDI value decreased significantly (Figure 5). According to the measurement results, the particle size was close to 24 h, but the PDI value was further decreased, and the large particles around 5000 nm turned into nanoparticular structure. In light of these findings, it was concluded that the most suitable hydrothermal treatment conditions were 80 °C, 250 rpm and 48 h to obtain the nMg/Al-NO_3-LDH.

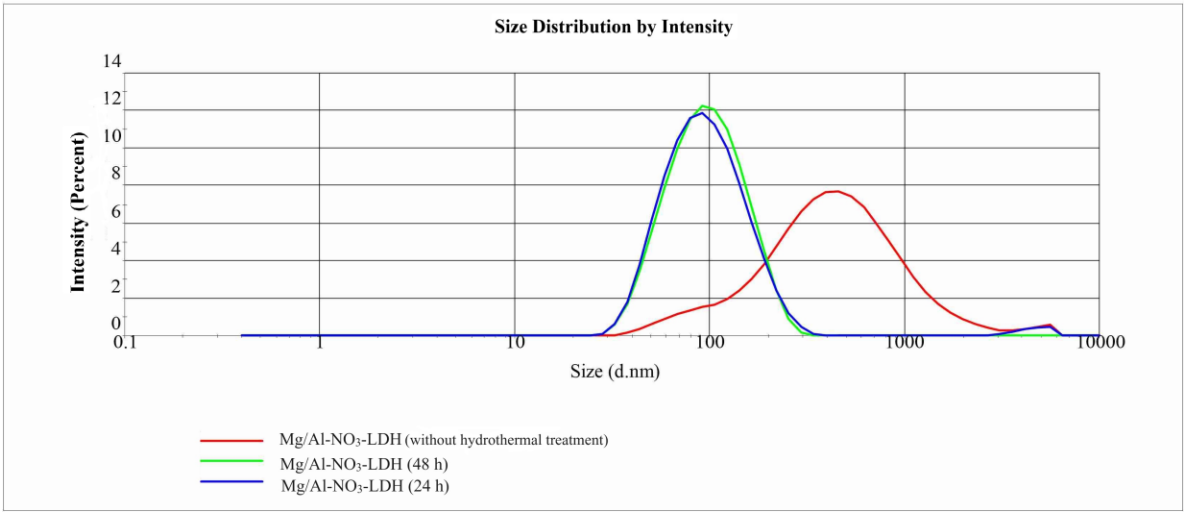

Figure 5. Effect of hydrothermal treatment time on the nMg/Al-NO_3-LDH particle size

3.3 Colloidal Stability of nMg/Al-NO_3-LDH

A colloidal stability of nMg/Al-NO_3-LDH was carried out to determine the change in particle size, PDI and zeta potential in the duration of use depending on the time and +4 °C storage condition (Table 4). Results were taken in triplicate. According to Table 4, the measurement results show that the Z average varied slightly between 86.87±0.320 and 109.6±2.3 nm. Moreover, PDI values are located between 0.132±0.018 and 0.276±0.018. Although the results of zeta potential were very close to the value obtained in the first synthesis of nMg/Al-NO_3-LDH, it changed slightly within 5 weeks. nMg/Al-NO_3-LDH remains stable for 5 weeks.

Table 4. Colloidal stability of nMg/Al-NO_3-LDH stored at +4 ±1˚C for 5 weeks.

Time (Week)	*Z-average (nm)*	*PDI*	*Zeta potential (mV) ±SD*
After preparation	86.87±0.32	0.132±0.018	44.4±8.74
1	97.29±8.22	0.173±0,017	47.6±8.58
2	93.71±1.44	0.173±0.011	49.7±6.93
3	95.39±2.50	0.205±0.038	46.3±8.77
4	107.55±2.80	0.228±0.019	41.8±7.82
5	109.6±2.30	0.276±0.018	47.3±7.94

4. CONCLUSION

As a result, the synthesis of nMg/Al-NO_3-LDH was optimized in this study. The effects of time, temperature, and stirring rate on the size and zeta potential of nMg/Al-NO_3-LDH were evaluated. The most suitable condition for synthesis was 80 ˚C, 48 h and 250 rpm, and nanoparticles with the particle size of 86.87 nm, a PDI of 0.132, and a zeta potential (mV) of 44.4±8.74 were obtained. The colloidal stability of nMg/Al-NO_3-LDH was then monitored for 5 weeks. The prepared nanoparticles maintained physical stability for up to 5 weeks under +4±1˚C storage conditions. Insights from this study revealed important data on tailoring nMg/Al-NO_3-LDH for specific biological applications, from controlled release systems to advanced catalytic materials. Future studies on drug loading and biodistribution will increase the prospective importance of nMg/Al-NO_3-LDH prepared under optimum conditions.

REFERENCES

[1] Kameliya J., Verma A., Dutta P., Arora C., Vyas S., Varma R.S. (2023). "Layered Double Hydroxide Materials: A Review on Their Preparation, Characterization, and Applications." Inorganics 11, 121

[2] Gama B., Selvasembian R., Giannakoudakis D.A., Triantafyllidis K.S., McKay G., Meili L. (2022). "Layered Double Hydroxides as Rising-Star Adsorbents for Water Purification: A Brief Discussion." Molecules 27. 10.3390/molecules27154900

[3] Constantino V.R.L., Figueiredo M.P., Magri V.R., Eulálio D., Cunha V.R.R., Alcântara A.C.S., Perotti G.F. (2023). "Biomaterials Based on Organic Polymers and Layered Double Hydroxides Nanocomposites: Drug Delivery and Tissue Engineering." Pharmaceutics 15. 10.3390/pharmaceutics15020413

[4] Choy J.-H., Jung J.-S., Oh J.-M., Park M., Jeong J., Kang Y.-K., Han O.-J. (2004). "Layered double hydroxide as an efficient drug reservoir for folate derivatives." Biomaterials 25, 3059-3064. https://doi.org/10.1016/j.biomaterials.2003.09.083

[5] Mohanambe L., Vasudevan S. (2005). "Anionic clays containing anti-inflammatory drug molecules: Comparison of molecular dynamics simulation and measurements." The Journal of Physical Chemistry B 109, 15651-15658

[6] Li L., Gu W., Chen J., Chen W., Xu Z.P. (2014). "Co-delivery of siRNAs and anti-cancer drugs using layered double hydroxide nanoparticles." Biomaterials 35, 3331-3339. https://doi.org/10.1016/j.biomaterials.2013.12.095

[7] Kura A.U., Ain N.M., Hussein M.Z., Fakurazi S., Hussein-Al-Ali S.H. (2014). "Toxicity and metabolism of layered double hydroxide intercalated with levodopa in a Parkinson's disease model." Int J Mol Sci 15, 5916-5927. 10.3390/ijms15045916

[8] Wong Y., Markham K., Xu Z.P., Chen M., Max Lu G.Q., Bartlett P.F., Cooper H.M. (2010). "Efficient delivery of siRNA to cortical neurons using layered double hydroxide nanoparticles." Biomaterials 31, 8770-8779. 10.1016/j.biomaterials.2010.07.077

[9] Chen C., Wang P., Lim T.-T., Liu L., Liu S., Xu R. (2013). "A facile synthesis of monodispersed hierarchical layered double hydroxide on silica spheres for efficient removal of pharmaceuticals from water." Journal of Materials Chemistry A 1, 3877-3880. 10.1039/C3TA10197E

[10] Janani F.Z., Taoufik N., Khiar H., Boumya W., Elhalil A., Sadiq M., Puga A.V., Barka N. (2021). "Nanostructured layered double hydroxides based photocatalysts: Insight on synthesis methods, application in water decontamination/splitting and antibacterial activity." Surfaces and Interfaces 25, 101263. https://doi.org/10.1016/j.surfin.2021.101263

[11] Özgümüş S., Gök M.K., Bal A., Güçlü G. (2013). "Study on novel exfoliated polyampholyte nanocomposite hydrogels based on acrylic monomers and Mg–Al–Cl layered double hydroxide: Synthesis and characterization." Chemical Engineering Journal 223, 277-286. https://doi.org/10.1016/j.cej.2013.02.098

[12] Mishra G., Dash B., Pandey S. (2018). "Layered double hydroxides: A brief review from fundamentals to application as evolving biomaterials." Applied Clay Science 153, 172-186. https://doi.org/10.1016/j.clay.2017.12.021

[13] Liu L., Deng Q., White P., Dong S., Cole I.S., Dong J., Chen X.-B. (2022). "Hydrothermally prepared layered double hydroxide coatings for corrosion protection of Mg alloys – a critical review." Corrosion Communications 8, 40-48. https://doi.org/10.1016/j.corcom.2022.07.001

[14] He C., Hu Y., Yin L., Tang C., Yin C. (2010). "Effects of particle size and surface charge on cellular uptake and biodistribution of polymeric nanoparticles." Biomaterials 31, 3657-3666. https://doi.org/10.1016/j.biomaterials.2010.01.065

[15] Ladewig K., Xu Z.P., Lu G.Q. (2009). "Layered double hydroxide nanoparticles in gene and drug delivery." Expert Opin Drug Deliv 6, 907-922. 10.1517/17425240903130585

[16] Costa F.R., Leuteritz A., Wagenknecht U., Jehnichen D., Häußler L., Heinrich G. (2008). "Intercalation of Mg–Al layered double hydroxide by anionic surfactants: Preparation and characterization." Applied Clay Science 38, 153-164. https://doi.org/10.1016/j.clay.2007.03.006

[17] Molano-Mendoza M., Donneys-Victoria D., Marriaga-Cabrales N., Angel Mueses M., Puma G.L., Machuca-Martínez F. (2019). "Dataset on infrared spectroscopy and X-ray diffraction patterns of Mg-Al layered double hydroxides by the electrocoagulation technique." Data Brief 27, 104564. 10.1016/j.dib.2019.104564

[18] Jin S., Ye K. (2007). "Nanoparticle-mediated drug delivery and gene therapy." Biotechnol Prog 23, 32-41. 10.1021/bp060348j

[19] Xu Z.P., Stevenson G., Lu C.-Q., Lu G.Q. (2006). "Dispersion and Size Control of Layered Double Hydroxide Nanoparticles in Aqueous Solutions." The Journal of Physical Chemistry B 110, 16923-16929. 10.1021/jp062281o

[20] Harrison R., Li L., Gu Z., Xu Z.P. (2017). "Controlling mesoporous silica-coating of layered double hydroxide nanoparticles for drug control release." Microporous and Mesoporous Materials 238, 97-104. https://doi.org/10.1016/j.micromeso.2016.04.031

[21] Zhang L.-x., Xie X.-x., Liu D.-q., Xu Z.P., Liu R.-t. (2018). "Efficient co-delivery of neo-epitopes using dispersion-stable layered double hydroxide nanoparticles for enhanced melanoma immunotherapy." Biomaterials 174, 54-66. https://doi.org/10.1016/j.biomaterials.2018.05.015

[22] Zuo H., Gu Z., Cooper H., Xu Z.P. (2015). "Crosslinking to enhance colloidal stability and redispersity of layered double hydroxide nanoparticles." J Colloid Interface Sci 459, 10-16. 10.1016/j.jcis.2015.07.063

[23] Dong H., Parekh H.S., Xu Z.P. (2015). "Particle size- and number-dependent delivery to cells by layered double hydroxide nanoparticles." Journal of Colloid and Interface Science 437, 10-16. https://doi.org/10.1016/j.jcis.2014.09.010

[24] Musumeci A.W., Mortimer G.M., Butler M.K., Xu Z.P., Minchin R.F., Martin D.J. (2010). "Fluorescent layered double hydroxide nanoparticles for biological studies." Applied Clay Science 48, 271-279. https://doi.org/10.1016/j.clay.2009.11.008

[25] Bilati U., Allémann E., Doelker E. (2005). "Development of a nanoprecipitation method intended for the entrapment of hydrophilic drugs into nanoparticles." European Journal of Pharmaceutical Sciences 24, 67-75. https://doi.org/10.1016/j.ejps.2004.09.011

[26] Choi G., Piao H., Kim M.H., Choy J.-H. (2016). "Enabling Nanohybrid Drug Discovery through the Soft Chemistry Telescope." Industrial & Engineering Chemistry Research 55, 11211-11224. 10.1021/acs.iecr.6b02971

[27] Dong H., Chen M., Rahman S., Parekh H.S., Cooper H.M., Xu Z.P. (2014). "Engineering small MgAl-layered double hydroxide nanoparticles for enhanced gene delivery." Applied Clay Science 100, 66-75. https://doi.org/10.1016/j.clay.2014.04.028

[28] Cao Z., Adnan N.N.M., Wang G., Rawal A., Shi B., Liu R., Liang K., Zhao L., Gooding J.J., Boyer C., Gu Z. (2018). "Enhanced colloidal stability and protein resistance of layered double hydroxide nanoparticles with phosphonic acid-terminated PEG coating for drug delivery." J Colloid Interface Sci 521, 242-251. 10.1016/j.jcis.2018.03.006

[29] Persano F., Batasheva S., Fakhrullina G., Gigli G., Leporatti S., Fakhrullin R. (2021). "Recent advances in the design of inorganic and nano-clay particles for the treatment of brain disorders." Journal of Materials Chemistry B 9, 2756-2784. 10.1039/D0TB02957B

[30] Danaei M., Dehghankhold M., Ataei S., Hasanzadeh Davarani F., Javanmard R., Dokhani A., Khorasani S., Mozafari M.R. (2018). "Impact of Particle Size and Polydispersity Index on the Clinical Applications of Lipidic Nanocarrier Systems." Pharmaceutics 10. 10.3390/pharmaceutics10020057

[31] Qin L., Wang W., You S., Dong J., Zhou Y., Wang J. (2014). "In vitro antioxidant activity and in vivo antifatigue effect of layered double hydroxide nanoparticles as delivery vehicles for folic acid." Int J Nanomedicine 9, 5701-5710. 10.2147/ijn.S74306

[32] Bhattacharjee S. (2016). "DLS and zeta potential – What they are and what they are not?" Journal of Controlled Release 235, 337-351. https://doi.org/10.1016/j.jconrel.2016.06.017

[33] Xu R. (2008). "Progress in nanoparticles characterization: Sizing and zeta potential measurement." Particuology 6, 112-115. https://doi.org/10.1016/j.partic.2007.12.002

[34] Xu Z.P., Jin Y., Liu S., Hao Z.P., Lu G.Q. (2008). "Surface charging of layered double hydroxides during dynamic interactions of anions at the interfaces." J Colloid Interface Sci 326, 522-529. 10.1016/j.jcis.2008.06.062

[35] Zhang Y., Evans J.R.G. (2012). "Alignment of layered double hydroxide platelets." Colloids and Surfaces A: Physicochemical and Engineering Aspects 408, 71-78. https://doi.org/10.1016/j.colsurfa.2012.05.033

ALKU Journal of Science 2023, Sayı 5(3): 176-191
e-ISSN: 2667-7814

Original Article

ESO-Based Backstepping Control of DC-DC Buck Converter Under Mismatched Load Disturbance

Akın Uslu[1*], Emrah Irmak[1]
[1]*Alanya Alaaddin Keykubat University, Rafet Kayış Faculty of Engineering, Department of Electrical and Electronics Engineering, Antalya, Turkey.*
**akin.uslu@alanya.edu.tr*

Abstract

The DC buck converter plays a critical role in supplying unfluctuated DC load voltage, however, which is exposed to various parametric uncertainties and disturbances operating under sensitive loads. This paper proposes a composite backstepping control strategy with an extended state observer (ESO) for the buck converter. Firstly, a backstepping control function is constructed to derive an inner current loop reference assuming load disturbance is known, which renders the global stability of the system. An ESO is designed to estimate the unmatched load current and collaborate with the backstepping controller to obtain disturbance attenuation. Quantitative selection of control and observer gains are provided under the highly nonlinear relationship of system dynamics. The rigorous stability of the proposed scheme is proved with an analysis of robustness. Finally, simulation results illustrate the comparative performance of the proposed control scheme against the disturbance caused by the load and uncertainties.

Keywords: Backstepping, Buck converter, Uncertainty, Observer.

DA-DA Alçaltan Dönüştürücülerin Uyumsuz Bozucu Yük Altında GDG Tabanlı Geri Adım Kontrolü

Özet

DC alçaltan dönüştürücüler dalgalanmayan DC yük gerilimi sağlamada kritik bir rol oynar, bununla birlikte hassas yükler altında çalışırken çeşitli parametrik belirsizliklere ve bozucu etkilere maruz kalmaktadır.Bu çalışmada alçaltan tip dönüştürücüler için genişletilmiş durum gözlemleyicisi (GDG) ile birlikte geri-adım kontrol stratejisini içeren tümleşik bir kontrol yapısı önerilmektedir. İlk olarak, sistemin genel kararlılığını sağlayan ve yük bozulmalarının bilindiği varsayılarak iç akım döngüsü referansı üretmek amacıyla bir geri-adımlama kontrol fonksiyonu oluşturulur.Daha sonra, eşleşmeyen yük akımını tahmin etmek ve bozulmayı azaltmak için geri adımlama denetleyicisi ile işbirliği yapmak üzere bir GDG tasarlanmıştır.Kontrol ve gözlemci kazançlarının seçimi, sistem dinamiklerinin doğrusal olmayan ilişkileri altında sağlanmıştır. Önerilen kontrol yapısının kesin kararlılığı, gürbüzlük analizi ile birlikte sağlanmıştır. Son olarak, önerilen kontrol yöntemi için yükün ve belirsizliklerin neden olduğu bozulmalara karşı karşılaştırmalı performansını gösteren simülasyon sonuçları verilmiştir.

Anahtar Kelimeler: Geri-adım, Alçaltan dönüştürücü, Belirsizlik, Gözlemleyici.

Geliş/Received: 27 Kasım/November 2023
Kabul Ediliş/Accepted: 6 Aralık/December 2023

1. INTRODUCTION

DC buck converter is one of the most popular power processing units to change the input/output voltage ratio of DC sources, which are widely applied in photovoltaic panels, renewable energy conversion, portable equipment, electric vehicles, HVDC, motor drives, and industrial processes [1-6].

The DC buck converter is modelled with unmodelled dynamics such as parametric uncertainties and disturbances. These unknown dynamics consist of time delay, parametric variation of passive elements, and unmodelled effects of no-ideal switching elements. Besides, input voltage and load variations are commonly encountered disturbances in the operation of DC buck converters. The main control objective in power circuits is to reach the desired voltage level on the output under source voltage variation and load resistor. To obtain satisfactory control performance, some of the linear approaches have been studied such as cascade proportional–integral (PI) control [7], and proportional-integral-derivative (PID) [8].

However, linear approaches are designed on the small-signal model of the converter around the desired operation points. Thus, only the local stability of the closed-loop system can be provided. When the DC-DC converter system is subjected to large fluctuations far away from the operating point, system stability may deteriorate. Furthermore, this leads to limited dynamic response of the closed-loop system.

To achieve a better dynamic response, various nonlinear control methods have been developed, such as robust control [9–11], adaptive control [12–14], sliding-mode control [15–17], intelligent control [18–20], and disturbance rejection control [21–23].

Predictive control has excellent dynamic response at the expense of relative computational load [24]. Except, predictive control has the disadvantage of adjusting the weighting factor. Although sliding mode control is robust to model uncertainties, it lacks the chattering phenomenon [25]. Repetitive control rejects periodic disturbance, but it has a relatively long internal time delay [26].

The above nonlinear approaches are evaluated from different perspectives according to advantages and sufferings, while they have two limitations in common. In one respect, they are insufficient to rigorously provide the large signal stability of the system. For another, it only focuses on uncertainty and disturbances, which take action on the same channels as the control law.

The large-signal stability of the system can be ensured with Lyapunov's direct method theory, which is designed based on a candidate Lyapunov function (V). In the conventional approach for Lyapunov's, the control law and pseudo-variables are designed to ensure $dV/dt < 0$ [27]. However, control law constructed merely has a single current control loop [28]. When extended for the DC-DC converter regulation, the output voltage is accompanied by steady-state error, which causes a slower dynamic response.

To solve this problem, [29] a virtual filter capacitor voltage is imported to the loop so that a two-loop control stability can be implemented. However, with this approach, the negative definiteness of dV/dt fails, which means the large-signal stability cannot be always guaranteed. It also makes load-current sensors mandatory for practical application.

Adaptive control is developed in [30], which has dual control loops to obtain satisfactory steady state and transient performance and also guarantee large-signal stability. Meanwhile, it obviates the use of load-current sensors. However, to construct the Lyapunov function systematically, backstepping control provides explicit rules that contribute to deriving the virtual reference states and control law within simplified design steps [31].

Most of the previous work only considers disturbances and uncertainties that take on the same channel as the control input which is called matched uncertainty. However, the output voltage of DC buck converters is also disturbed by the so-called unmatched variations like output current, which causes great difficulty for the robust controller design.

To address the mismatching problem, some variable structure schemes have been proposed such as sliding mode control (SMC), adaptive SMC [32], and SMC with integral action [33]. However, these studies

require definite disturbance bounds or first-time derivatives, which are hard to obtain due to the nonlinearity of DC buck converter systems.

Extended state observer (ESO) could achieve an estimation of the variations and disturbances without the knowledge of their boundary limits [34], which originally differs from the classical observers. It constitutes an integrator's chain to make the system canonical form and separate the actual plant from the nominal form plus a lumped disturbance. It lumps a wide range of uncertainties, including unmodeled dynamics, parametric variation, and external unknown disturbance. Thus, it provides a model-independent framework and a strong robustness and anti-disturbance ability.

Considering the limitations of the aforementioned approaches, this study proposes an ESO-based composite robust control approach to regulate buck converter voltage, whose main contribution is summarized as two points:

- The composite backstepping controller has a separate control structure, that could provide the large-signal stability of the system.
- To compensate for mismatched load current disturbance, ESO is designed to feedforward it to the backstepping controller, resulting in accurate tracking and rigid robustness.

2. SYSTEM DESCRIPTION AND MODELING

A basic pulse width modulated (PWM) DC buck converter is shown in Fig. 1. Where v_s, i_L, i_o, v_o and u are input voltage, inductor current, load current, output voltage, and PWM input respectively. Mosfet (Q) and diode (D) are used as switching devices for the converter. The resistor of the load, inductor, and capacitor, which are the passive components of the circuit, are denoted by R, L, C respectively. The values of the components are given in Table 1.

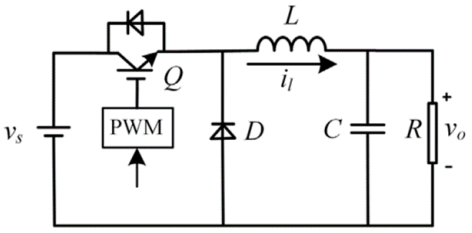

Figure 1. DC-DC Buck converter

Table 1. Parametric values of DC-buck converter

Elements	Parameters	Values
Dc source voltage	v_s	20 V
Reference voltage	v_r	10 V
Filter inductor	L	4.3 mH
Filter capacitor	C	1000 uF
Load resistor	R	100
Switching frequency	f_s	10 kHz

Ignoring the high-frequency dynamics of switching devices, the mean model of the DC buck dynamics is derived as follows:

$$L\frac{di_L}{dt} = uv_s - v_o \tag{1}$$

$$C\frac{dv_o}{dt} = i_L - \frac{v_o}{R} \tag{2}$$

The load resistance R is a major source of uncertainty and the variation in R causes the change of load current Io, which is described as a disturbance for converter dynamics. For ease of representation and derivation, the following equivalent substitution is carried out, given by

$$x_1 = v_o, \quad x_2 = i_L, \quad \frac{v_o}{R} = i_o \tag{3}$$

where (1) can be rewritten as

$$C\dot{x}_1 = x_2 - i_o \tag{4}$$

$$L\dot{x}_2 = uv_s - x_1 \quad (5)$$

The control aim is to keep the load voltage v_o to a reference DC value. With the tuning of the PWM duty ratio μ, x_1 is forced to track its reference x_1^*.

3. BACKSTEPPING CONTROLLER DESIGN

3.1 Derivation of Inductor Current Reference

Load voltage error is expressed as

$$z_1 = x_1^* - x_1 \quad (6)$$

The Lyapunov candidate function for the load voltage error can be selected as

$$V_1 = \frac{1}{2}z_1^2 \quad (7)$$

Differentiating the Lyapunov function (7) alongz_1, yields out that

$$\dot{V}_1 = z_1\dot{z}_1 \quad (8)$$

According to (4) and (6), the full derivation of (8) can be derived as

$$\dot{V}_1 = z_1(\dot{x}_1^* - \dot{x}_1) = z_1\left(\dot{x}_1^* - \frac{x_2 - I_o}{C}\right) \quad (9)$$

The pseudo-inductor current-reference x_1^* is chosen to ensure $\dot{V}_1 < 0$, given by

$$x_2^* = I_o + k_1 C z_1 + C\dot{x}_1^* \quad (10)$$

where $k_1$is a positive constant, which is used for the controller parameter (k_1>0).

If $x_1$is regulated to track x_1^*, (9) will be reformulated as

$$\dot{V}_1 = -k_1 z_1^2 \leq 0 \quad (11)$$

which becomes a negative semi-definite.

3.2 Derivation of Control Law

The pseudo-tracking error for inductor current is expressed as

$$z_2 = x_2^* - x_2 \quad (12)$$

The second Lyapunov candidate function is composed of V_1 and quadratic inductor current tracking error, defined as

$$V_2 = \frac{1}{2}z_1^2 + \frac{1}{2}z_2^2 \quad (13)$$

The time derivative of (13), is given as follows:

$$\dot{V}_2 = z_1\dot{z}_1 + z_2\dot{z}_2 \quad (14)$$

According to (9) and (12), a detailed derivation of (14) can be formulated as

$$\dot{V}_2 = z_1\left[\dot{x}_1^* - \frac{(x_2^* - z_2) - I_o}{C}\right] + z_2(\dot{x}_2^* - \dot{x}_2) \quad (15)$$

To guarantee $\dot{V}_2 < 0$, the control function can be chosen as

$$u = \frac{1}{V_s}\left(x_1 - L\dot{x}_2^* + \frac{L}{C}z_1 + k_2 z_2\right) \quad (16)$$

Where k_2 is a positive constant, which is used for the controller parameter ($k_2 > 0$). Substituting (16) into (15), the second Lyapunov function becomes negative semidefinite, given by

$$\dot{V}_2 = -k_1 z_1^2 - k_2 \frac{z_2^2}{L} \leq 0 \tag{17}$$

4. DESIGN OF THE ESO TO ESTIMATE AND FEEDFORWARD THE LOAD CURRENTS FOR LOAD DISTURBANCE REJECTION

Eq. (10) shows that I_o is needed to generate a pseudo reference x_2^* on the aim of load disturbance rejection. Also load current sensor can be used to sense I_o, however, it increases the cost and deteriorates the system reliability. A better alternative, an ESO can be designed to observe $I_o$for control input [12]. With the help of the ESO observer, the proposed backstepping control law builds a nonlinear composite structure. Since I_o is unmeasurable in practice, an ESO for this type of control system can only be built using inductor current I_o as input and output v_o of the system assuming that I_o is differentiable w.r.t time and $\dot{I}_o$ is bounded [22].

In the proposed control aim is to implement an ESO to estimate $\hat{I}_o$, so that disturbance effect of I_o can be rejected. To design the observer, output voltage dynamics in Eq. (1) is augmented with I_o and reformulated as in the following state space form:

$$\begin{cases} \dot{x} = Ax(t) + Bu_p(t) + E\dot{f}(t) \\ y_p(t) = C_p x(t) \end{cases} \tag{18}$$

where,

$$A_p = \begin{bmatrix} 0 & 1 \\ 0 & 0 \end{bmatrix} \quad B_p = \begin{bmatrix} \frac{1}{C} \\ 0 \end{bmatrix} \quad C_p = [1 \quad 0] \quad E = \begin{bmatrix} 0 \\ 1 \end{bmatrix}$$

$$y_p = V_o \qquad u_p = I_L$$

The corresponding ESO can be configured as follows:

$$\begin{aligned} \dot{\hat{x}}(t) &= A_p \hat{x}(t) + B_p u_p(t) + L_p\left[y_p(t) - \hat{y}_p(t)\right] \\ &= \left(A_p - L_p C_p\right)\hat{x}(t) + B_p u_p(t) + L_p y_p(t) \\ \hat{y}_p(t) &= C_p \hat{x}(t) \end{aligned} \tag{19}$$

where $\hat{x}(t) = [\hat{V}_o \quad \hat{I}_o]$ denotes the estimated state variable v_o and I_o, and $L_p = [l_1 \quad l_2]^T$ is the observer gain matrix. The observation error $x_e(t) = [x_{e1} \quad x_{e2}]^T$ of the ESO is

$$x_e = x(t) - \hat{x}(t) \tag{20}$$

and subtracting (19) from (18), we have

$$\begin{aligned} \dot{x}_e(t) &= D x_e(t) + E\dot{f}(t) \\ D &= \begin{bmatrix} -l_1 & 1 \\ -l_2 & 0 \end{bmatrix}, E = \begin{bmatrix} 0 \\ 1 \end{bmatrix} \end{aligned} \tag{21}$$

Observer parameters are selected such that D is Hurwitz with desired eigenvalues. Bandwidth parametrization is a frequently used method for the observer gains [17],

$$s^2 + l_1 s + l_2 = (s + \omega_o)^2 \tag{22}$$

with ω_o being the observer bandwidth. According to equation (20), observer parameters can be chosen as:

$$l_1 = 2\omega_o \, , l_2 = \omega_o^2 \tag{23}$$

A common rule of thumb is used to select the observer bandwidth as ω_o= (2~5) ω_n, where ω_n is controller natural frequency.

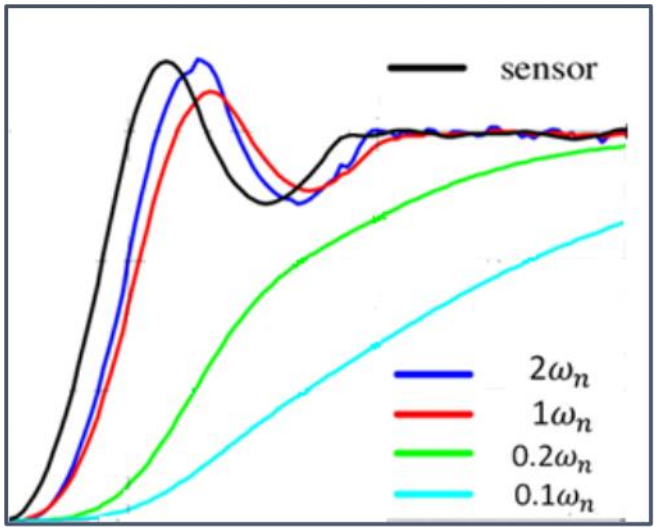

Figure 2. The tracking performance of the ESO as ω_o varies

The tracking performance of ESO is shown in Fig. 2. It shows that choosing ω_o needs a trade-off between controller bandwidth and disturbance sensitivity. When $\omega_o = 2\omega_c$, the estimated load current is almost the same as the sensor output, however, when $\omega_o = 0.1\omega_c$, it takes a very long time to reach the sensor value.

4.1 Formation of ESO Based Backstepping Control

Then the estimated variables can be used to feedforward I_o to generate inductor current reference x_2^* as follows:

$$x_2^* = \hat{I}_o + k_1 C z_1 + C\dot{x}_1^* \tag{24}$$

The designed control law, including the disturbance rejection term and the backstepping controller, can be formulated as:

$$u = \frac{1}{V_s}\left[x_1 + \frac{d}{dt}L\left(\hat{I}_o + Ck_1 z_1\right) + \frac{L}{C}z_1 + k_2 z_2\right] \tag{25}$$

It has two dual control loops, which are the outer voltage loop z_1 and pseudo-inductor-current loop z_2. Voltage-loop control gain is k_1 and current-loop control gain k_1. A block diagram of the buck converter controlled by the proposed control law is depicted in Fig.3.

PWM modulator compares the control signal u(t) with the triangle carrier wave to produce the switching gate signal mosfet. Inductor current i_l and output voltage $v_o$are measured by sensors. Besides, there is no need to measure load-current I_o due to estimation.

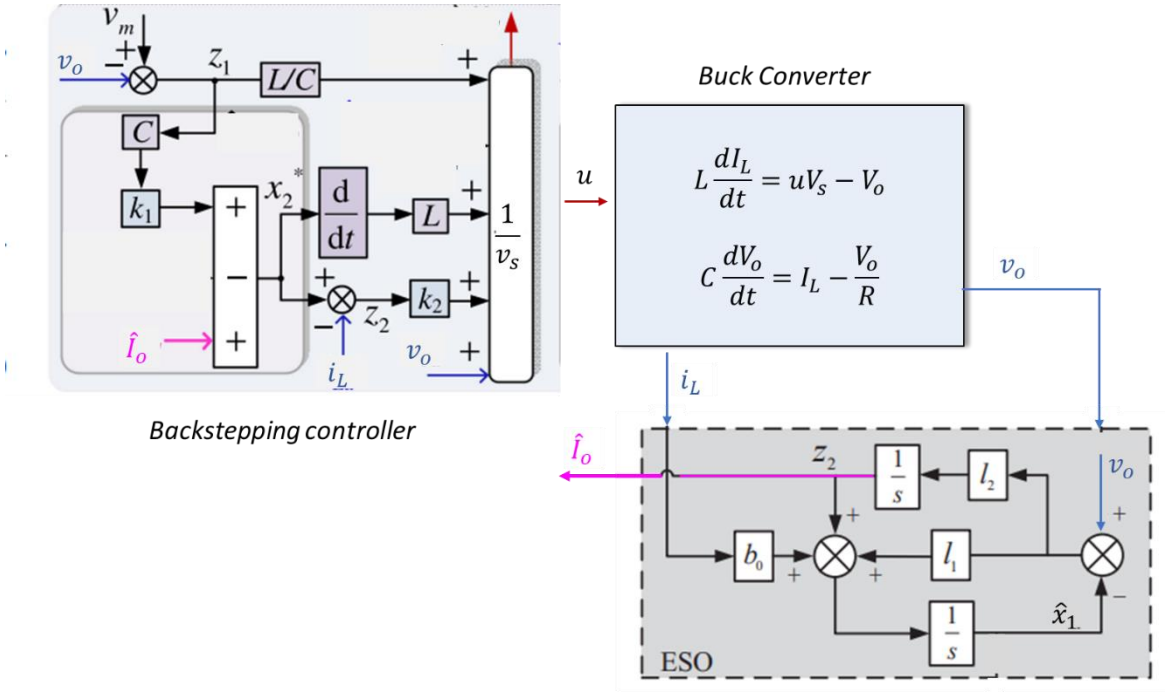

Figure 3. Blok diagram of ESO-based backstepping control for buck converter

To obtain quantitative controller gains, closed-loop error (z_1, z_2) dynamics should be constituted. Substituting (16) to (4), it yields

$$C\dot{x}_1 = x_2^* - z_2 - I_o \tag{26}$$

The inductor current-loop reference (10) is substituted into (26), which gives out that

$$\dot{z}_1 = -k_1 z_1 + z_2/C \tag{27}$$

Similarly, the switching functions (16) is substituted to (5), which gives

$$\dot{z}_2 = -z_1/C - k_2 z_2/L \tag{28}$$

Error dynamics in (27), (28) can be written in compact form as

$$\dot{z}_c = Kz_c \tag{29}$$

where $z_c = [z_1 \quad z_2]^T$, and

$$K = \begin{bmatrix} -k_1 & 1/C \\ -1/C & -k_2/L \end{bmatrix} \qquad k_1 > 0, \qquad k_2 > 0$$

The characteristic equation of matrix K is derived as

$$\det(sI - K) = s^2 + \left(k_1 + \frac{k_2}{L}\right)s + \frac{k_1 k_2}{L} + 1/C^2 \tag{30}$$

Equation (30), demonstrate that closed-loop error dynamics turned into a typical second-order system. So, the damping ratio (ξ) and the natural frequency ω_n can be used as main indicators for tuning the controller gains.

The parameters ξ and ω_n directly indicate the steady-state and dynamic characteristics of the controlled system. The faster dynamic response can be obtained with larger ω_n, which implies that state variables will be regulated to reach their references with less time. While larger ξ provides more damping for the system, which leads small overshoot while transient response.

Initially, (30) equates to the second-order characteristic equations, given by

$$\det(sI - K) = s^2 + (2\xi\omega_n)s + \omega_n^2 = 0 \tag{31}$$

Eq. (31) has two solutions for, described as $s_{1,2}$:

$$s_{1,2} = -\xi\omega\_n \pm \omega_n\sqrt{\xi^2 - 1} \tag{32}$$

where ξ and ω_n are derived as

$$\xi = \frac{CLk_1 + Ck_2}{2\sqrt{k_1k_2LC^2 - L^2}} \qquad \omega_n = \sqrt{\frac{k_1k_2}{L} + \frac{1}{C^2}} \tag{33}$$

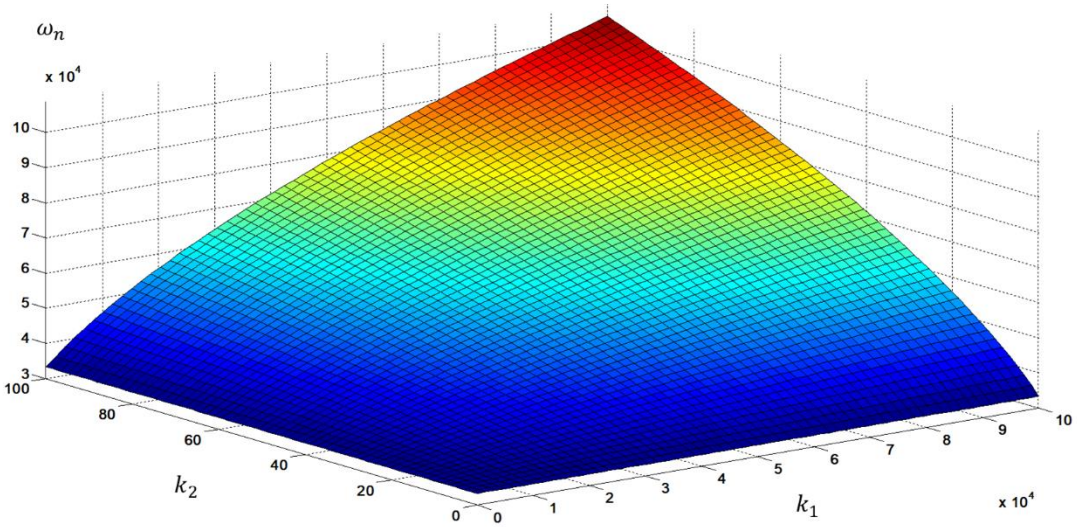

Figure 4. Natural frequency ω_n as k_1 and k_2 increases

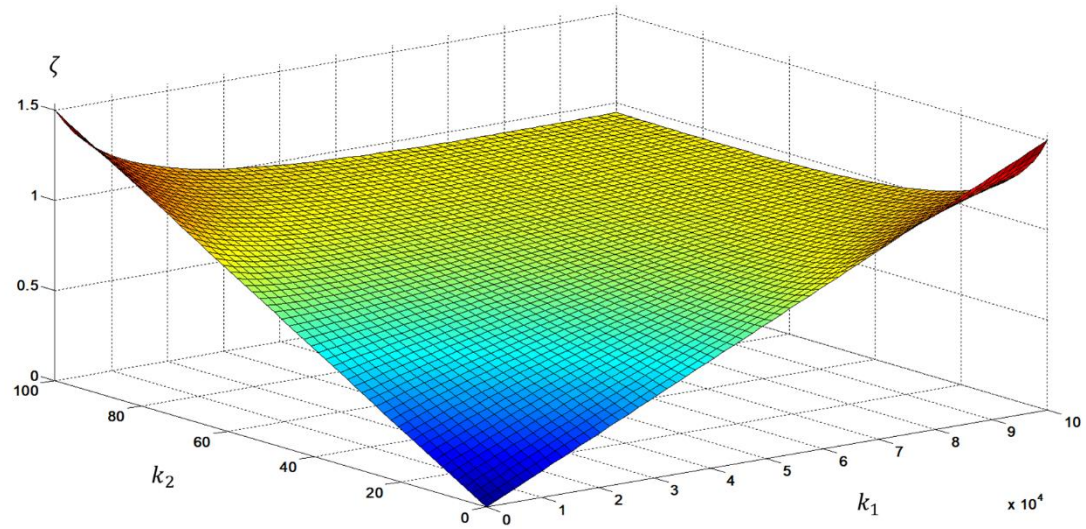

Figure 5. Damping ratio ξ as k_1 and k_2 increases

Fig. 4 and 5 depict the variation of ξ and ω_n with the increase of k_1 and k_2 according to (33). It shows that ξ and ω_n have a highly non-linear relationship with k_1 and k_2. Although, control parameters k_1 and k_2 can be estimated from Fig. 4 and Fig. 5 it is hard to select ξ and ω_n simultaneously. A better alternative is making a trade-off between settling time and overshoot during transients, where ξ is the fixed optimal damping ratio.

$$\xi = \frac{\mathrm{CLk_1 + Ck_2}}{2\sqrt{\mathrm{k_1 k_2 LC^2 - L^2}}} = \frac{\sqrt{2}}{2} = 0.707 \tag{34}$$

After mathematical transformation (34) can be rewritten as,

$$\frac{\mathrm{k_1^2}}{\left(\sqrt{2}/\mathrm{C}\right)^2} + \frac{\mathrm{k_2^2}}{\left(\sqrt{2}\mathrm{L}/\mathrm{C}\right)^2} = 1 \tag{35}$$

Where $k_1 > 0$ and $k_2 > 0$. Certainly, an equivalent parametric Eq. (36) can be expressed in the trigonometric aspect as,

$$\mathrm{k_1} = \frac{\sqrt{2}}{\mathrm{C}}\cos\theta \qquad \mathrm{k_2} = \frac{\sqrt{2}\mathrm{L}}{\mathrm{C}}\sin\theta \qquad \text{Where, } \theta \in [0, \pi/2] \tag{36}$$

Under this condition, the controller parameters ($\mathrm{k_1}$, k_2) can be determined optimally,

$$\begin{cases} \mathrm{k_1} = \sqrt{2}\cos\theta/\mathrm{C}\big|_{\theta=\frac{\pi}{4}} = \dfrac{1}{\mathrm{C}} \\ \mathrm{k_2} = \sqrt{2}\mathrm{L}\sin\theta/\mathrm{C}\big|_{\theta=\frac{\pi}{4}} = \dfrac{\mathrm{L}}{\mathrm{C}} \end{cases} \tag{37}$$

5. STABILITY

In this section, the stability of the ESO and the controlled system is analyzed. From (21), it can be seen that it is always possible to choose the observer constants l_1 and l_2 such that the eigenvalues of D can be placed in the left half plane. Thus, we can always define a positive definite matrix P such that.

$$D^T P + PD = -Q \tag{38}$$

for any given positive definite matrix Q. Assume that, λm is the smallest eigenvalue of Q. Defining a Lyapunov candidate

$$V_o = {x_e}^T P x_e \tag{39}$$

Then derivating along V_o along (21)

$$\begin{aligned} \dot{\mathrm{V}}_\mathrm{o} &= {\mathrm{x_e}}^\mathrm{T}\left(\mathrm{D^T P + PD}\right)\mathrm{x_e} + 2{\mathrm{x_e}}^\mathrm{T}\mathrm{PE}\dot{\mathrm{f}} \\ &\leq -{\mathrm{x_e}}^\mathrm{T}\mathrm{Q}\mathrm{x_e} + 2\|\mathrm{PE}\|\|\mathrm{x_e}\|\mu \\ &\leq -\lambda_\mathrm{m}\|\mathrm{x_e}\|^2 + 2\|\mathrm{PE}\|\|\mathrm{x_e}\|\mu \\ &\leq -\|\mathrm{x_e}\|(\lambda_\mathrm{m}\|\mathrm{x_e}\| + 2\|\mathrm{PE}\|\mu) \end{aligned} \tag{40}$$

It can be concluded from (40) that as time goes to infinity, the estimation error is ultimately bounded by

$$\|\mathrm{x_e}\| \leq \lambda_1 \tag{41}$$

Where,

$$\lambda_1 = \frac{2\|PE\|}{\lambda_m} \tag{42}$$

Lyapunov function for the controller V_o is evaluated to prove the stability of the closed-loop system around (27), which is given by

$$V_c = z_c{}^T z_c \tag{43}$$

The time derivative of (43) is given by

$$\begin{aligned} \dot{V}_c &= \dot{z}_c{}^T z_c + z_c{}^T \dot{z}_c \\ &= z_c{}^T (K^T + K) z_c \\ &= z_c{}^T \left(\begin{bmatrix} -2k_1 & 0 \\ 0 & -2k_2/L \end{bmatrix} \right) z_c \end{aligned} \tag{44}$$

which proves that system stability is not affected by L, C if k_1, k_2>01.

6. SIMULATION RESULTS

In this section, the performance of the designed control law is simulated in Matlab in Fig 6. The conventional backstepping strategy, the ESO-based backstepping, and PI control methods are compared in terms of transient and steady-state response. The classical PI control unit is demonstrated by Eq. (45). For the ESO-backstepping, an extended state observer collaborates to estimate the unmatched uncertainties and load current. Control performance may vary concerning the parameters for many controllers. Therefore, to obtain a fair comparison between test controllers, the parameters of the three controllers have been tuned for their optimal response. The simulation aims to control the output voltage of the buck converter at reference in the condition of uncertainties and also to ensure the controllers track a desired reference voltage. The converter component and controller gains of the buck converter are summarized in Table 2.

$$u_{pi} = k_p z_1 + k_i \int z_1 \tag{45}$$

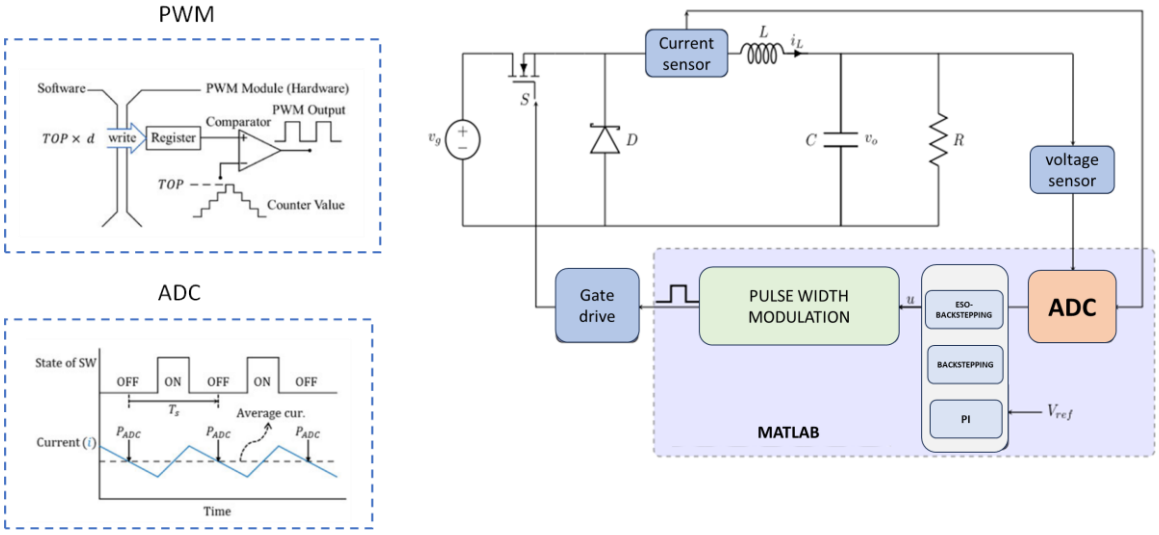

Figure 6. Block diagram of simulation setup

Table 2. Controller gains for buck converter

Control methods	Parameters
Backstepping	$k_1 = 10^3$ $k_2 = 4.7$
ESO	$l_1 = 5x10^4$ $l_2 = 8x10^6$
PI	$k_p = 10, k_i = 5000$

6.1 Case 1: Variation of the Load

To evaluate the robustness against load variation, the resistance R is dropped from full load to half load at t = 3 s, and the results are simulated in Fig. 7. while keeping nominal source voltage v_s at 24 V and $Vref$ at 10 V, It can be seen that both ESO-backstepping and backstepping achieve good robustness against the load changing compared to the backstepping, the ESO-backstepping dynamic performance is better with fast transient response and less overshoot. However, in the classical PI, a large steady tracking error prevents it from reaching the desired output voltage. In addition, the ESO-backstepping is observed superior disturbance reduction compared with the other schemes. Both the ESO-backstepping and backstepping achieve a true estimation of the unmatched uncertainties, but the ESO-backstepping response is faster than other schemes.

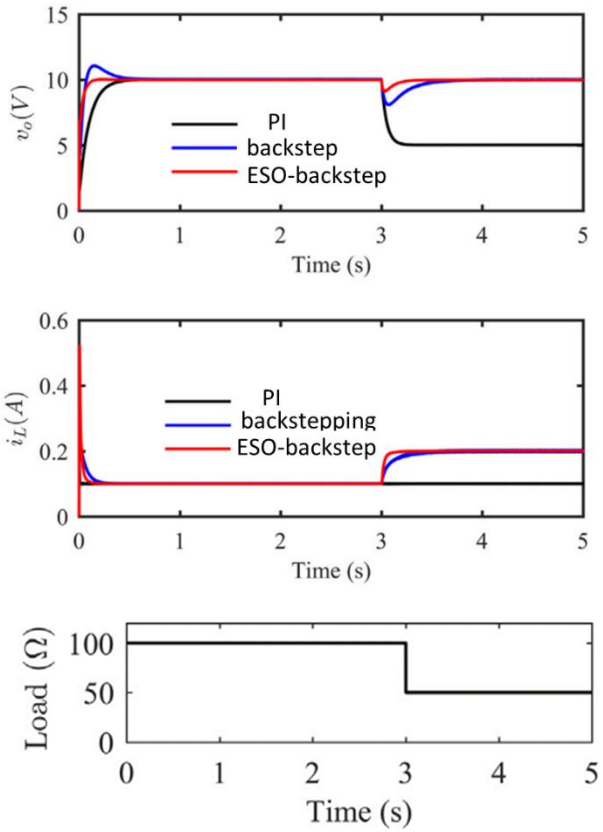

Figure 7. Buck converter with half load change

6.2 Case 2: Variation of Source Voltage

The input voltage v_s is changed in a step and drop fashion from 20-24-16 V while keeping load resistance as nominal and setting Vref voltage at 10 V. Keeping the controller configuration constant, simulated controller results are shown in Fig. 8. Until t = 4 s, it is observed that the backstepping and PI reach the reference output voltage, which means the robustness against to the matched uncertainties is verified. However, at t = 4 s, the output voltage of backstepping and PI have a large steady-state error because the

control gains of the two controllers are insufficient to prevent the magnitude of disturbance. In the condition of input voltage variation, the ESO-backstepping achieved a 10 V output voltage again with a short-term transient.

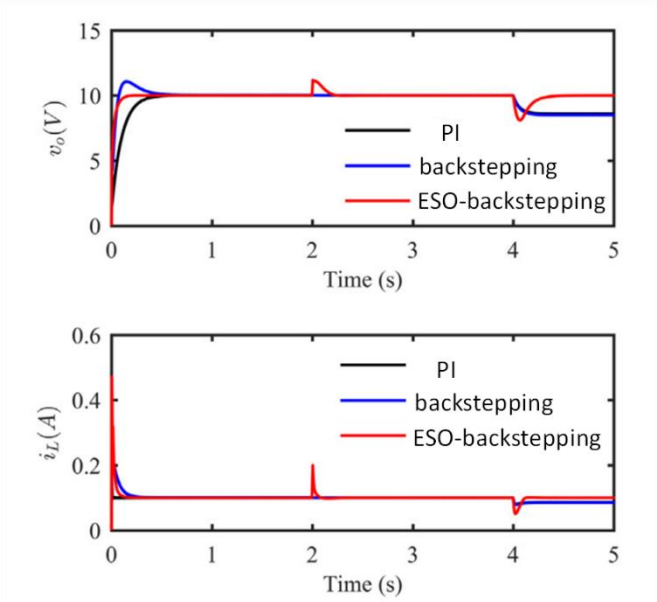

Figure 8. Buck converter with step change of input voltage

6.3 Case 3: Reference Voltage Variation

Next, the desired voltage is changed between 10 and 15 V in step, ramp, and sinusoidal form. Starting with 15V reference voltage and then it is dropped to 10V at t=0.5s. Also, ramp and sinusoidal reference voltage are changed between 15 and 10V. From the results shown in Fig. 9, it can observed that the ESO-backstepping and backstepping could exactly track the variable voltage while it has a steady state error in the order of 0.13 V. Compared with the backstepping, the ESO-based backstepping oscillates with small magnitude and has shorter transient response.

6.4 Case 4: Continuous Load Resistance

To evaluate the performance of the proposed control method with time-varying disturbance in continuous variation, the load resistor is set as R = 20 sin $(0.5\pi t)$. The controller configurations remain the default value, the simulation results are given in Fig. 10. It can be seen that ESO-backstepping achieves high disturbance rejection against the continuous variation of load with faster dynamic response and zero steady-state error. However, backstepping has a 2.3% steady tracking error. The PI is insufficient to track the reference output voltage due to the high oscillation and 27% steady-state error.

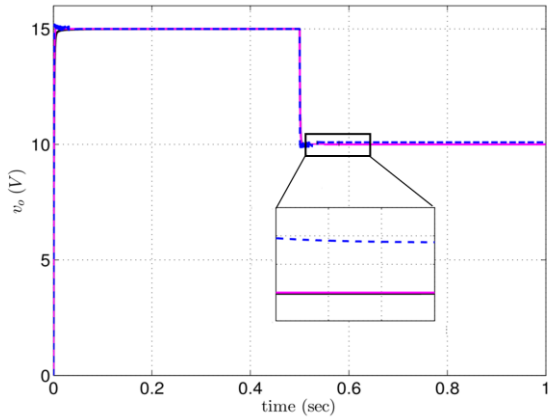

(a)

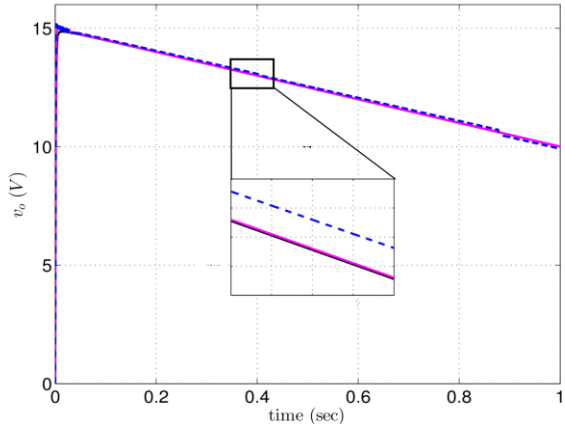

(b)

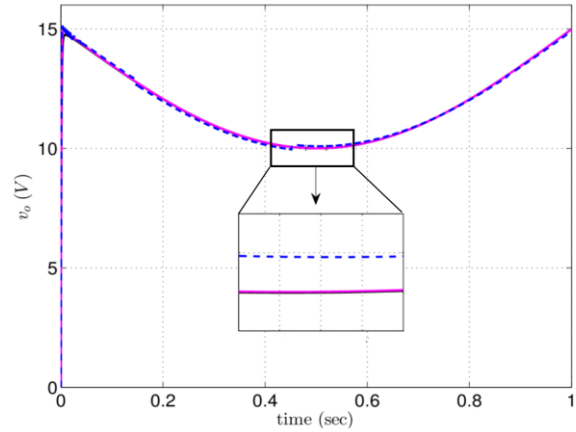

(c)

Figure 9. Buck converter with step change of reference voltage (a) step (b) ramp and (c) sinusoidal

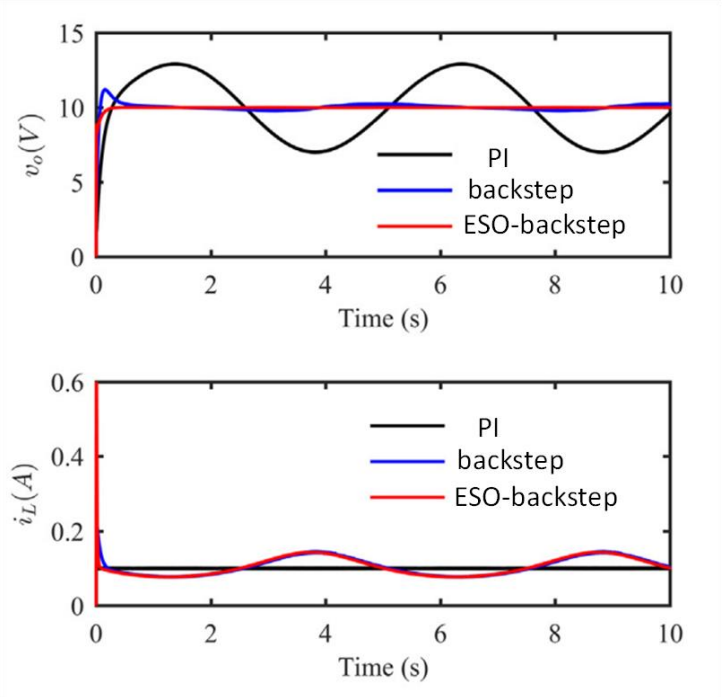

Figure 10. Buck converter with time-varying load

7. CONCLUSION

In this paper, an extended state observer-based backstepping control approach is implemented to a buck converter, to provide a steady DC bus voltage. The ESO-backstepping is designed for the estimation of unmatched load current. Then, a backstepping control law is consolidated with the estimated load current, which makes the robust control law. Simulation results display the performance of the proposed control scheme, with a fast transient response, zero steady-state error, and robustness against uncertainties and disturbances.

REFERANSLAR

[1] Dai, P., Cauet, S., & Coirault, P. (2016). Disturbance rejection of battery/ultracapacitor hybrid energy sources. Control Engineering Practice, 54, 166–175.

[2] Wang, J., Li, S., Yang, J., Wu, B., & Li, Q. (2016). Finite-time disturbance observer based non-singular terminal sliding-mode control for pulse width modulation-based DCDC buck converters with mismatched load disturbances. IET Power Electronics, 9(9), 1995–2002.

[3] König, O., Gregorčič, G., & Jakubek, S. (2013). Model predictive control of a DC–DC converter for battery emulation. Control Engineering Practice, 21(4), 428–440.

[4] Zhong, Q.-C., & Hornik, T. (2013). Control of power inverters in renewable energy and smart grid integration. IEEE-Wiley Press.

[5] Labbe, B., Allard, B., Lin-Shi, X., & Chesneau, D. (2013). An integrated sliding-mode buck converter with switching frequency control for battery-powered applications. IEEE Transactions on Power Electronics, 28(9), 4318–4326.

[6] Silva-Ortigoza, R., Hernández-Guzmán, V. M., Antonio-Cruz, M., & Munoz-Carrillo, D. (2015). DC/DC Buck power converter as a smooth starter for a DC motor based on a hierarchical control. IEEE Transactions on Power Electronics, 30(2), 1076–1084.

[7] Chen, Z., Gao, W., Hu, J., & Ye, X. (2011). Closed-loop analysis and cascade control of a nonminimum phase boost converter. IEEE Transactions on Power Electronics, 26(4), 1237–1252.

[8] Walker, G. R., & Sernia, P. C. (2004). Cascaded DC-DC converter connection of photovoltaic modules. IEEE Transactions on Power Electronics, 19(4), 1130–113.

[9] J. Alvarez-Ramirez, G. Espinosa-Perez, and D. Noriega-Pineda, "Current- ´ mode control of DC–DC power converters: A backstepping approach," Int. J. Robust Nonlinear Control, vol. 13, no. 5, pp. 421–442, Apr. 2003.

[10] C. Olalla, R. Leyva, A. E. Aroudi, and I. Queinnec, "Robust LQR control for PWM converters: An LMI approach," IEEE Trans. Ind. Electron., vol. 56, no. 7, pp. 2548–2558, Jul. 2009.

[11] Q.-C. Zhong and T. Hornik, "Cascaded current–voltage control to improve the power quality for a grid-connected inverter with a local load," IEEE Trans. Ind. Electron., vol. 60, no. 4, pp. 1344–1355, Apr. 2013.

[12] G. Escobar, A. Valdez, J. Leyva-Ramos, and P. Mart ´ ´ınez, "A controller for a boost converter with harmonic reduction," IEEE Trans. Control Syst. Technol., vol. 12, no. 5, pp. 717–726, Sep. 2004.

[13] G. J. Jeong, I. H. Kim, and Y. I. Son, "Design of an adaptive output feedback controller for a DC/DC boost converter subject to load variation," Int. J. Innov. Comput. Inf. Control, vol. 7, no. 2, pp. 791–803, Feb. 2011.

[14] J. Linares-Flores, A. H. Mendez, C. Garc ´ ´ıa-Rodr´ıguez, and H. SiraRam´ırez, "Robust nonlinear adaptive control of a boost converter via algebraic parameter identification," IEEE Trans. Ind. Electron., vol. 61, no. 8, pp. 4105–4114, Aug. 2014.

[15] E. Vidal-Idiarte, C. E. Carrejo, J. Calvente, and L. Mart´ınez-Salamero, "Two-loop digital sliding mode control of DC–DC power converters based on predictive interpolation," IEEE Trans. Ind. Electron., vol. 58, no. 6, pp. 2491–2501, Jun. 2011.

[16] S. Oucheriah and L. Guo, "PWM-based adaptive sliding-mode control for boost DC–DC converters," IEEE Trans. Ind. Electron., vol. 60, no. 8, pp. 3291–3294, Aug. 2013.

[17] O. Lopez-Santos, L. Martinez-Salamero, G. Garcia, H. Valderrama-Blavi, and T. Sierra-Polanco, "Robust sliding-mode control design for a voltage regulated quadratic boost converter," IEEE Trans. Power Electron., vol. 30, no. 4, pp. 2313–2327, Apr. 2015.

[18] L. Guo, J. Y. Hung, and R. M. Nelms, "Evaluation of DSP-based PID and fuzzy controllers for DC–DC converters," IEEE Trans. Ind. Electron., vol. 56, no. 6, pp. 2237–2248, Jun. 2009.

[19] R.-J. Wai and L.-C. Shih, "Adaptive fuzzy-neural-network design for voltage tracking control of a DC–DC boost converter," IEEE Trans. Power Electron., vol. 27, no. 4, pp. 2104–2115, Apr. 2012.

[20] S. E. Beid and S. Doubabi, "DSP-based implementation of fuzzy output tracking control for a boost converter," IEEE Trans. Ind. Electron., vol. 61, no. 1, pp. 196–209, Jan. 2014.

[21] J. Linares-Flores, J. L. Barahona-Avalos, H. Sira-Ram´ırez, and M. A. Contreras-Ordaz, "Robust passivity-based control of a buck–boostconverter/dc-motor system: An active disturbance rejection approach," IEEE Trans. Ind. Appl., vol. 48, no. 6, pp. 2362–2371, Nov./Dec. 2012.

[22] Y.-X. Wang, D.-H. Yu, and Y.-B. Kim, "Robust time-delay control for the DC–DC boost converter," IEEE Trans. Ind. Electron., vol. 61, no. 9, pp. 4829–4837, Sep. 2014.

[23] M. Sitbon, S. Schacham, and A. Kuperman, "Disturbance observer based voltage regulation of current-mode-boost-converter-interfaced photovoltaic generator," IEEE Trans. Ind. Electron., vol. 62, no. 9, pp. 5776– 5785, Sep. 2015.

[24] Zhang, Q., Min, R., Tong, Q., Zou, X., Liu, Z., & Shen, A. (2014). Sensorless predictive current controlled DC–DC converter with a self-correction differential current observer. IEEE Transactions on Industrial Electronics, 61(12), 6747–6757.

[25] Cucuzzella, M., Lazzari, R., Trip, S., Rosti, S., Sandroni, C., & Ferrara, A. (2018). Sliding mode voltage control of boost converters in DC microgrids. Control Engineering Practice, 73, 161–170.

[26] S. Jiang, D. Cao, Y. Li, J. Liu, and F. Z. Peng, "Low-THD, fasttransient, and cost-effective synchronous-frame repetitive controller for three-phase UPS inverters," IEEE Trans. Power Electron., vol. 27, no. 6, pp. 2994–3005, Jun. 2012.

[27] Tan, S.-C., Lai, Y., Tse, C. K., & Cheung, M. K. (2006). Adaptive feedforward and feedback control schemes for sliding mode controlled power converters. IEEE Transactions on Power Electronics, 21(1), 182–192.

[28] I. Son and I. H. Kim, "Complementary PID controller to passivity based nonlinear control of boost converters with inductor resistance," IEEE Trans. Control Syst. Technol., vol. 20, no. 3, pp. 826–834, May 2012.

[29] Kim, S.-K., & Lee, K.-B. (2015). Robust feedback-linearizing output voltage regulator for DC-DC boost converter. IEEE Transactions on Industrial Electronics, 62(11), 7127–7135.

[30] H. K. Khalil, Nonlinear Systems. Englewood Cliffs, NJ, USA: PrenticeHall, 2002.

[31] J. Alvarez-Ramirez, G. Espinosa-Perez, and D. Noriega-Pineda, "Current- ´ mode control of DC–DC power converters: A backstepping approach," Int. J. Robust Nonlinear Control, vol. 13, no. 5, pp. 421–442, Apr. 2003.

[32] Huang, A.-C., & Chen, Y.-C. (2004). Adaptive multiple-surface sliding control for nonautonomous systems with mismatched uncertainties. Automatica, 40(11), 19.

[33] Choi, H. H. (2007). LMI-based sliding surface design for integral sliding mode control of mismatched uncertain systems. IEEE Transactions on Automatic Control, 52(4), 736– 742.

[34] J. Han, "From PID to active disturbance rejection control," IEEE Trans. Ind. Electron., vol. 56, no. 3, pp. 900–906, Mar. 2009.